UNIVERSITY OF OKLAHOMA

GRADUATE COLLEGE

MECHANICAL PROPERTIES OF HUMAN INCUDOSTAPEDIAL JOINT AND

TYMPANIC MEMBRANE IN NORMAL AND BLAST-DAMAGED EARS

A DISSERTATION

SUBMITTED TO THE GRADUATE FACULTY

in partial fulfillment of the requirements for the

Degree of

DOCTOR OF PHILOSOPHY

By

SHANGYUAN JIANG
Norman, Oklahoma
2018

MECHANICAL PROPERTIES OF HUMAN INCUDOSTAPEDIAL JOINT AND
TYMPANIC MEMBRANE IN NORMAL AND BLAST-DAMAGED EARS

A DISSERTATION APPROVED FOR THE
STEPHENSON SCHOOL OF BIOMEDICAL ENGINEERING

BY

_____
Dr. Rong Z. Gan, Chair

_____
Dr. Vassilios I. Sikavitsas

_____
Dr. Matthias U. Nollert

_____
Dr. Edgar A. O'Rear

_____
Dr. Harold L. Stalford

I dedicate my dissertation work to my family.

Acknowledgements

I would like to express my sincere appreciation to my advisor, Dr. Rong Z. Gan for the enormous amount time, energy, resource, and patience she had devoted in my training process. I joined the Ph.D. program at the University of Oklahoma right after I got my bachelor degree and with great language difficulties. Dr. Gan has been teaching me how to think, read, learn and write as a researcher regardless of my weak background since the first day I arrived in the US. Her respect, enthusiasm, and persistence to work has deeply impressed me and changed my attitude towards my work and life. The past five years in the biomedical engineering laboratory is one of the most precious experiences in my life.

I would like to express my appreciation to my committee members, Dr. Vassilios I. Sikavitsas, Dr. Matthias U. Nollert, Dr. Edgar A. O'Rear and Dr. Harold L. Stalford for their time and effort spent on helping me completing my degree.

I would not be able to complete my degree without the help of our outstanding lab members. Zachary Yokell has helped me on my writing, experiments, lab maintenance, and helped me to get involved in the community. Dr. Xiying Guan, who had graduated in 2014, taught me skills in experiments and laser measurement. Dr. Xuelin Wang taught me knowledge in finite element modeling, solid mechanics, and mathematics. Dr. Xiao Ji had helped me on the computer and software problems as well as the general lab maintenance. Don Nakmali had taught me how to process human temporal bones. I would also appreciate Kyle Smith, Warren Engles, Kegan Leckness, and Brooke Hitt who joined the lab as master students for all the shared working experiences and fun we had together. Many thanks to Dr. Junfeng Liang, from the University of Texas at Dallas, who had

iv

helped me with protocols for mechanical measurement. Many thanks to Dr. Tao Chen who introduced me about the clinical experience on human middle ear surgeries. Marcus Brown, who joined the lab in 2016, helped me a lot on the 3D printing technique and English writing.

I would also like to appreciate Dr. Huiyang Luo and Dr. Hongbing Lu from the University of Texas at Dallas for building the split Hopkinson tension bar in our laboratory and high-speed camera in the blast chamber. I thank Mario Pineda and Vikrant Palan from Polytec Inc. for providing technical support for our laser equipment.

I would like to thank Dr. Thomas Seale in Department of Pediatrics at University of Oklahoma Health Science Center for teaching me English writing, helping me with my projects and providing us with experimental materials. I would express my appreciation to Dr. Tsia from University of Oklahoma Health Science Center for her help and advice on our research plan. Dr. Mark Wood at Hough Ear Institute gave us suggestions on our research plan as well.

I would express my appreciation to Dr. Michael Detamore, and his student, Emi Kiyotake, for sharing equipment with us.

Thank Melissa Foster, Bethany Burklund, Billy Mays, Greg Williams, and all the staff from the AME department for providing assistance and convenience on my study at OU. Thank Dora Rapp, Vanessa Smith and all the staffs in SRTC for providing convenience on our material and supplies. Thank Pamela Meek, Chrishayla Glover, and all the SBME staffs for providing assistance and convenience during my study at OU.

Finally, I appreciate my father and mother, Xin Jiang and Hong Li, for their unconditional support in the past five years. Their love is the source of energy for me to accomplish this degree.

Table of Contents

List of Tables

List of Figures

Abstract

The human ear consists of outer ear, middle ear and inner ear. The mechanical properties of the incudostapedial joint (ISJ) and tympanic membrane (TM) are critical to the sound transmission function of the ear because the transformation of the acoustic pressure to the mechanical vibration relies on the TM while the vibration of the ossicles transmits through ISJ into the cochlea. However, the dynamic properties of ISJ have not been reported in previous studies. Moreover, injuries in the TM and ISJ have been observed in ears exposed to blast overpressure. The structural and functional changes in the ISJ and TM during and after blast exposure were not investigated. In addition, the sound transfer function of the middle ear has not been characterized under blast overpressure. The absence of these mechanical properties and data obtained from function tests of the human ear impedes the improvement of the accuracy of the finite element (FE) model of the human ear which was designed to simulate the response of the ear to the blast overpressure.

In this study, biomechanical measurements were conducted on TM and ISJ specimens harvested from human cadaveric temporal bones (TB). The dynamic properties of the ISJ were measured using dynamic mechanical analyzer (DMA) at frequencies from 1 to 80 Hz at three temperatures of 5, 25 and 37 °C. The frequency-temperature superposition (FTS) principle was used to extrapolate the complex moduli of the ISJ specimens to 8 kHz. Then, the mechanical properties of ISJ under high-strain-rate deformation were measured by split Hopkinson tension bar. FE simulations on ISJ demonstrated that the behavior of the joint under harmonic and impulse loads was closely related to the structure and the mechanical properties of the joint components.

For biomechanical measurement of the TM, the full-field surface motion of human TMs was measured by scanning laser Doppler vibrometry (SLDV) over a frequency range from 1 to 8 kHz under normal and post-blast conditions. An FE model of the human TM with multilayer microstructure and orthogonal fiber network was built and successfully characterized the features of the surface motion measured from the normal and damaged ears. The consistency between the experimental data and model simulation suggested that the blast-induced damage to the collagen fibers in the TM.

To investigate the mechanism of the induction of the damage, a dual laser setup was established to capture the real-time motion of the TM in the period of time during which the blast waves were propagating through the ear. The motion of the TM umbo within 5 ms after the blast exposure arrived was measured and normalized by the blast pressure levels. The response of the ear was simulated by an FE model of human ear by applying the same input pressure at the entrance of the ear canal. The TM movement and pressure showed good consistency between the results the FE model prediction and the experimental data. The nonlinear behavior of the human middle ear under blast overpressure was observed.

In this dissertation, the behavior of the human ISJ and TM in the normal and blast-damaged was characterized through a series of biomechanical measurements. The quantitative data can be used as input for FE models of the human ear to improve their accuracy on predicting the behavior of the ear under both normal and blast conditions. The methods used in this series of studies provide novel approaches for micron-level biomechanical measurement under dynamic or impulse loads.

Chapter 1   Introduction

1.1 Structure and function of the middle ear

The human ear is the organ of hearing and balancing. The schematic diagram of the anatomic structure of the human ear is shown in Fig. 1.1. Human ear consists of the outer, middle and inner ear. Each of these three parts is responsible for the transfer function from the acoustic waves in the outside environment to the electric signals in the auditory nerve. The frequency range of the human auditory system is 20 Hz to 20 kHz.
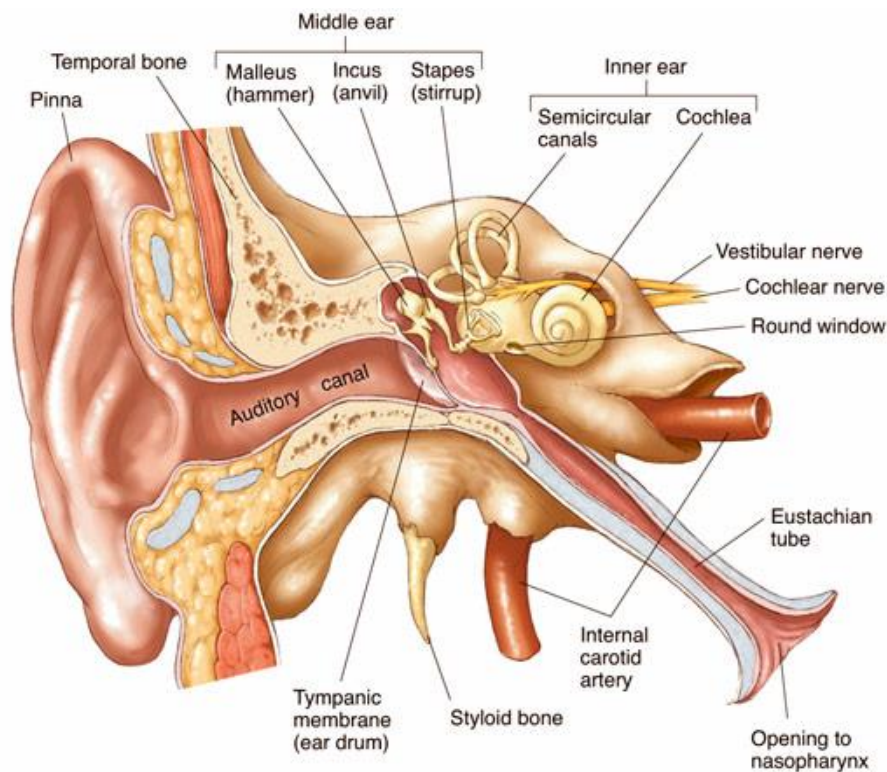
Figure 1.1 Anatomic structure of the human ear
(http://www.biographixmedia.com/human/ear-anatomy.html)

The outer ear is composed of the pinna and external ear canal (auditory canal shown in the Fig. 1.1). The pinna, also called the auricle, is the visible part of the ear consists of auricular cartilage (Bichara et al., 2011). The pinna has a direction-dependent function of collecting and amplifying acoustic signals which contributes to the

localization function of the human ear (Hackley Steven A., 2015; Middlebrooks and Green, 1991). The external ear canal is a long and narrow tunnel with a bony wall in its inner two thirds and cartilage wall in the outer one third (McLellan and Webb, 1957). The canal has a frequency-dependent amplification function of 12 dB sound pressure level (SPL) at 3.5 kHz (Gan et al., 2006).

The middle ear consists of the tympanic membrane (TM) and ossicular chain. The ossicular chain is suspended in the middle ear cavity (MEC) wall through ligaments and muscle tendons. The middle ear cavity is an air-filled space with a volume around 455 to 678 mm^3 connected to the nasopharynx through the Eustachian tube (Gan and Wang, 2007; Gan et al., 2004a). The pressure waves propagate through the ear canal to reach TM, transformed into the mechanical vibration of the ossicular chain, and finally turn into the pressure of the fluid inside the cochlea.

The TM is the barrier separating the external ear canal and the middle ear. It is almost oval with a long axis from 8.5 to 10 mm while horizontal axis ranges from 8 to 9 mm (Ferrazzini, 2003; Volandri et al., 2011). The TM has a cone shape pointed towards the inside of the MEC with an angle of 132-137° and cone depth around 1.42 – 2 mm (Daphalapurkar et al., 2009; Gan et al., 2004a). Umbo is an alternative name for the apex. The TM is located in the ear canal in a particular orientation to allow its surface area larger than the cross-section area of the ear canal. A typical value of the angle between the TM and the superior and anterior wall of the ear canal is around 30°, while 140° between the superior and posterior wall, respectively (Ferrazzini, 2003). The values of TM surface area range from 55.8 to 85.0 mm^2 (Gan et al., 2004a).

2
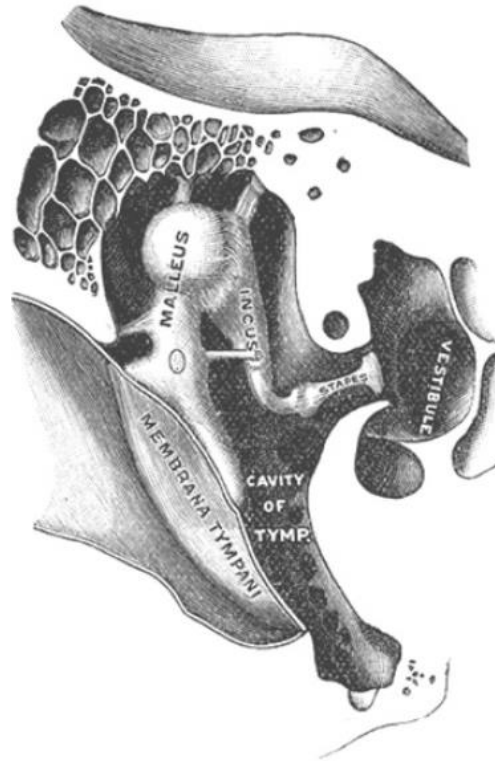
Figure 1.2 Middle ear
(Volandri et al., 2011)

The ossicular chain consists of three ossicles: the malleus, incus, and stapes from the TM to the oval window (Fig. 1.2). The detailed geometry of three ossicles has been described in Gan and Wang, 2007 and Stuhlman, 1937. To be brief, the malleus consists of a head and handle with an angle of 145°. The incus consists of a long, short, and lenticular process which are almost perpendicular to each other. The stapes consists of two cruses and a footplate to form a triangular shape. The reported average masses of the malleus, incus and stapes are 23-27, 25-32 and 2.05–4.35 mg. The handle of the malleus is connected to the medial side of TM through the manubrium. Three ossicles are connected by two synovial joints: the malleus and incus are connected by the incudomalleolar joint (IMJ) while the stapes and the incus are connected by the incudostapedial joint (ISJ). The stapes is connected to the oval window of the cochlea

through the stapedial annular ligament (SAL). The mechanical properties of TM, IMJ, ISJ, and SAL are critical to the sound transmission function of the middle ear and susceptible to diseases and injuries. The ossicular chain is connected to the middle ear bony wall through ligament and tendons: there are the superior mallear ligament, lateral mallear ligament, posterior incudal ligament, anterior mallear ligament, posterior stapedial ligament, tensor tympani tendon. The location of these soft tissues is self-explanatory. The stapedial tendon and the tensor tympani tendon are two muscle tendons that play important roles in the function of the middle ear.
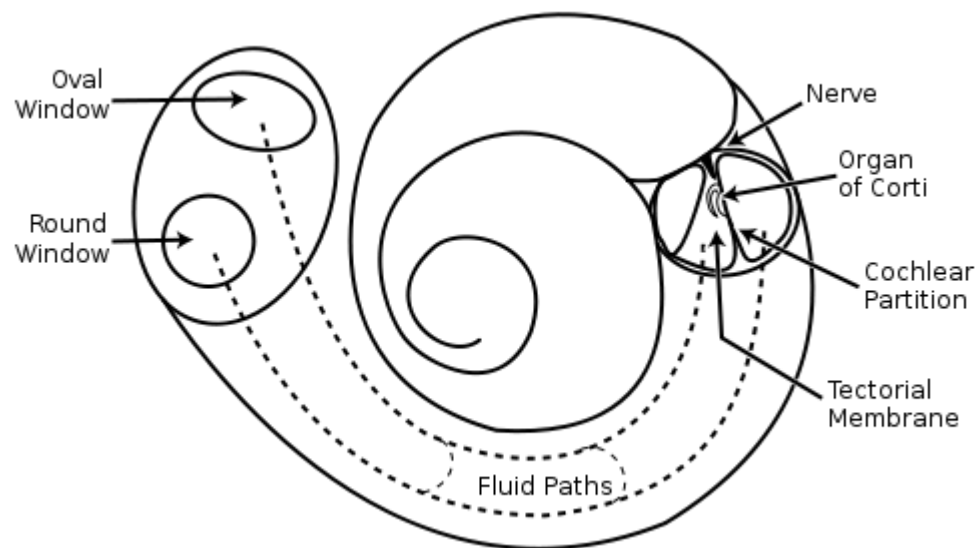
Figure 1.3 Structural diagram of the cochlea
(https://en.wikipedia.org/wiki/Cochlea)

The inner ear is located in the innermost part of the human ear, embedded into the wall of the temporal bone and consists of the cochlea and semicircular canals which indicates both the hearing and balance system are included in the inner ear. The human cochlea bony wall has a coil shape with two and a half turns from the base to the apex. The spiral cochlea has two openings: connects to the stapes footplate at the oval window and to the MEC at the round window membrane (Fig. 1.3). The lymph fluid sealed inside

the cochlea is divided into three chambers: scala vestibule, scala media, and scala tympani separated by cochlear basilar membrane and Reissner's membrane. The tectorial membrane is located between the Reissner's membrane and the basilar membrane. The scala vestibule is connected to the oval window and the scala tympani is connected to the round window membrane. The vibration of the stapes footplate produces fluid pressure change within the scala vestibule of the cochlea. The fluid pressure propagates in the scala vestibule to the apex and finally released through the round window membrane. The pressure difference between the scala vestibule and scala tympani thus drives the basilar membrane to vibrate. (Nakajima et al., 2009). The hair cells located between the basilar membrane and tectorial membrane are deformed due to the fluid pressure gradient between the scala vestibule and scala tympani and transform the pressure signal into the electrical signal to form the sense of hearing.

1.2 Mechanical properties of middle ear soft tissues

The mechanical properties of the middle ear soft tissues are critical to the sound transmission function of the middle ear, thus affecting the hearing function of the ear. Finite element (FE) models of the human ear are useful tools to investigate the function of the ear under normal, diseased or injured conditions (Gan et al., 2004a, 2007, 2018; Zhang and Gan, 2013). The mechanical properties of the soft tissues have been proved to be critical to the accuracy of the FE models, however, the quantitative data is usually limited and can only be determined by the cross-calibration method. In clinical research, human cadaveric temporal bone studies and experimental animals where the microstructural changes of the middle ear soft tissue have been observed, the mechanical properties of these soft tissues are not reported which impedes the understanding of the

mechanism of the conductive hearing loss resulted by the diseases (Guan et al., 2015, 2017; Jiang et al., 2016). Moreover, injuries of soft tissues such as rupture of TM and disarticulation of ISJ are observed in ears that experienced blast exposure which can result in a severe conductive hearing loss (Gan et al., 2016; Mayorga, 1997; Patterson and Hamernik, 1997; Yeh and Schecter, 2012). The behavior of the ISJ and TM have not been characterized under blast loads.

1.2.1 Incudostapedial joint

The ISJ is a synovial joint which is located between the incus and stapes connecting the lenticular process of the incus and the head of the stapes. Scanning electron microscopic and histologic results suggest that the ISJ consists of cartilage, meniscus, capsule, and synovial fluid (Funnell et al., 2005; Gan and Wang, 2015; Karmody et al., 2009; Ortug et al., 2006). In Fig. 1.4, the lenticular process of incus is marked by a star sign which shows a shape like a mushroom. The "stem" is concave, thin, and exquisitely delicate, consisting of thin linear trabeculae and spaces filled with areolar tissue (Karmody et al., 2009). The "cap" of the lenticular process of incus is covered by a layer of hyaline cartilage which extends to the articular surface. The articular cartilage of the head of the stapes is observed to be narrower than that of the lenticular cap which is also consist of hyaline cartilage with a porous structure. The meniscus between the articular cartilage consists of dense fibrous tissue which is similar to the composition of the articular disk of the temporomandibular joint (Karmody et al., 2009). The rest space inside the ISJ is filled by synovial fluid. The joint capsule connects the lenticular process of the incus and the head of the stapes which holds the synovial fluid inside the joint space. The joint capsule is a composite of mature collagen fibers and elastic fibers. A

major part of the fibers is aligned along the axis from the lenticular process to the stapes. A small number seem to be diagonal but in no specific direction (Karmody et al., 2009). Note that the stapedial muscle tendon is connected to the joint capsule on the left side of the Fig. 1.4, which is the posterior side of the ISJ. The bulk of the tendon consists of linear fibers that run in a posterior-to-anterior direction from the middle ear cavity to the ISJ. As shown in Fig. 1.4, the stapedial muscle tendon connects the ISJ to the stapedial muscle that deeply embedded in the middle ear cavity on the left. This complex structure plays an important role in the acoustic reflex which is an active mechanism to protect the inner ear under high-intensity sound.

The sound transmission function of the middle ear is closely related to the mechanical properties of the ISJ (Gan and Wang, 2015; Gan et al., 2004b). Severe conductive hearing loss, which usually requires surgical reconstruction of the ossicular chain to restore the hearing (Abdala and Keefe, 2012; Celik et al., 2009; Maducdoc et al., 2015; Sim and Chang, 2008; Suzuki et al., 2008; Vishwakarma et al., 2009) could be imposed by abnormalities of the ISJ. The recently conducted experimental measurement revealed that the increased ISJ stiffness (ankyloses) reduced the TM mobility and stapes footplate at 0.5-1 kHz (Alian et al., 2013) while the reduced ISJ stiffness (disarticulation) was related to the stapes mobility loss at high frequencies (Szymanski et al., 2014). However, these published results were not specific enough to characterize the relationship between the mechanical properties of the ISJ and middle ear transfer function without providing the material properties of the joint quantitatively.
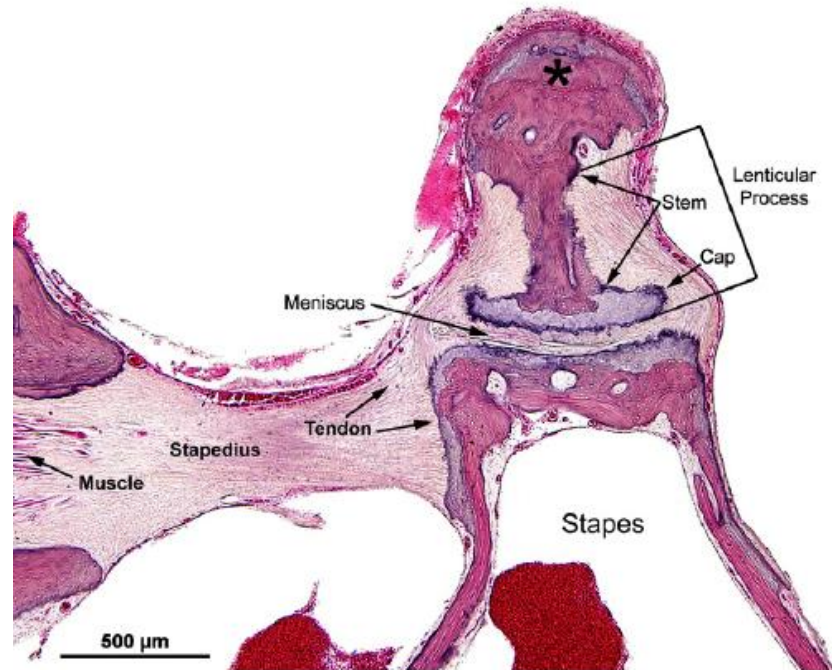
Figure 1.4 Histology section of human ISJ (Karmody et al., 2009)

A literature search indicates the published data on the mechanical properties of the ISJ is very limited. The quasi-static uniaxial loading test on human ISJ reported by (Zhang and Gan, 2010) is the only published biomechanical measurement which provides the mechanical properties of the ISJ directly. The results demonstrate that the ISJ is a synovial joint with viscoelastic properties with the nonlinear stress-strain relationship. The stiffness of the joint depends on the mechanical properties of the joint capsule, cartilage, and synovial fluid. However, the ISJ normally vibrates at the human auditory frequency range of 20 Hz to 20 kHz. The dynamic properties of the joint are more important to understand the contribution of the ISJ to the sound transmission function of the human ear and can provide a better description of the behavior of the joint under physiological conditions.
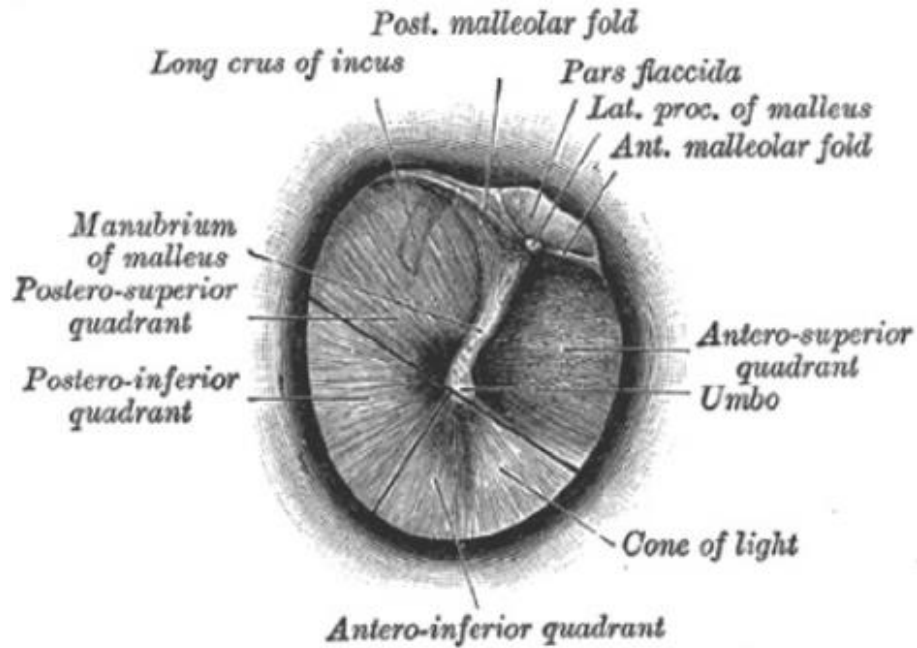
Figure 1.5 A schematic drawing of the medial side of human TM (Volandri et al., 2011)

The TM is a key component of the human auditory apparatus which is a complex biomechanical system, devoted to sound reception and perception. It plays an important role in transforming sound pressure into mechanical vibration and initiates the transfer function of the middle ear for sound transmission into the cochlea. The mechanical properties of TM have a great effect on the transfer function of the middle ear and the formation of hearing. Thus many experiments and theoretical approaches have been made to study its geometry, structure, static and dynamic properties.

Human TM consists of pars flaccida (PF), pars tensa (PT) and a tympanic annulus which firmly anchored the membrane to the wall of the ear canal (Fig. 1.5). The tympanic annulus is a fibrous thickening in the circumferential direction of the TM attached to the sulcus in the tympanic bony ring except it separates the PF and PT in the superior region (Aernouts and Dirckx, 2011). The PF lies in the superior region with higher thickness and

compliance than the PT (Decraemer and Funnell, 2008). The major surface area of the TM is occupied by the PT, which contributes most to the sound transmission function of the membrane. The thickness distribution of the TM varied over the surface and can be different in individuals. The thickness value commonly used in the biomechanical properties of the PT is 60 to 80 μm (Cheng et al., 2006; Daphalapurkar et al., 2009; Fay et al., 2005; Kuypers et al., 2006; Luo et al., 2009; Zhang and Gan, 2012). In the cross-section in the through-thickness direction of human TM PT, a multilayer structure consisting of distinct layers, varying in density, thickness, and arrangement in different regions, can be identified (Fig. 1.6a). TM PT shows a tri-layer structure, with a mucosal epithelial layer in the medial side, an epidermal layer in the lateral side and an intermediate fibrous layer, the lamina propria, which makes the major difference between the PT and PF. The lamina propria of the PF is made up of loose connective tissue containing collagen and elastic fibers. The lamina propria of the PT, however, consists of two connective tissue layers, between which there are two collagenous layers with radial and circumferential fibers (Fig. 1.6b). The radial fibers converge on the manubrium, while the circumferential fibers are in the direction parallel to the TM annulus. These collagen fibers exhibit a viscoelastic and orthotropic behavior with membrane (in-plane) properties different from through-thickness (out-of-plane) properties (Daphalapurkar et al., 2009).
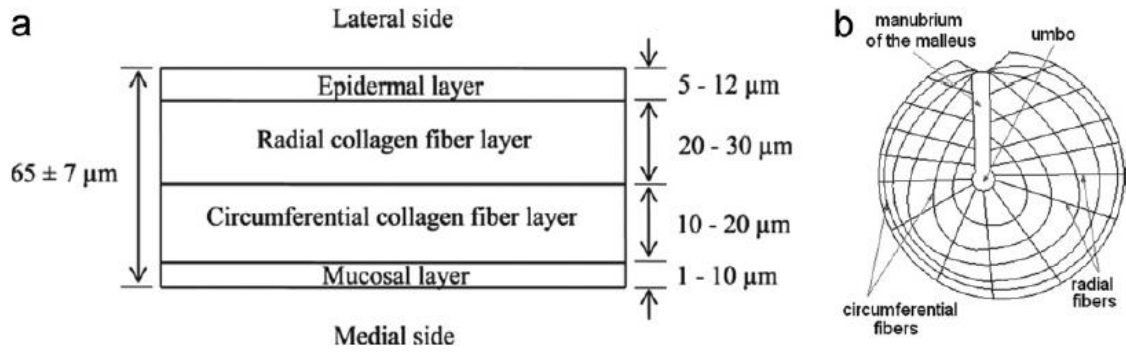
Figure 1.6 Multi-layer structure of TM (a) a schematic diagram in through-thickness direction of PT; (b) schematic of the fiber orientation of human TM. (Volandri et al., 2011)

The mechanical properties of human TM have been reported in a series of studies. In the 1960s, the elastic modulus reported by Von and Kirikae were 20 and 40 MPa, respectively (Kirikae, 1960; Von Békésy and Wever, 1960). The reliability of these results was limited by the precision of the thickness measurements of the TM (Volandri et al., 2011). With the improvement of the thickness measurement technique, Cheng et al. (2006) reported that the elastic modulus varied from 0.4 to 22 MPa over the stress range from 0 to 1 MPa in uniaxial quasi-static tensile test on rectangular strips harvested from human cadaveric samples, which was in good agreement with the data reported by Decraemer et al., 1980. Quasi-static tests on TM with intact structure and boundary condition instead of a rectangular strip have been conducted by Aernouts et al. (2012) using nanoindentation. The reported Young's modulus was 2.1-4.4 MPa. Based on the assumption that the TM is not isotropic, Daphalapurkar et al. (2009) used the nano-indentation techniques to measure the viscoelastic functions of four quadrants of TM in the through-thickness and in-plane directions separately. The in-plane modulus of human TM was reported as 25.73 to 37.8 MPa. Recently, new techniques have been developed for in-situ measurements of the TM such as the micro fringe projection reported by Liang et al. (2016).

Considering the fact that under physiological conditions, TM vibrates over the auditory frequency range from 20 Hz to 20 kHz, the dynamic mechanical properties of TM can provide a better understanding of the contribution of TM to the sound transmission function of the ear. The dynamic properties of human TM were reported by Zhang and Gan, 2012 using dynamic properties analyzer (DMA) and the results were expanded using the frequency-temperature superposition (FTS) method. The mean storage modulus was 15.1 ± 3.0 MPa at 1 Hz and 27.6 ± 5.1 MPa at 3800 Hz. The mean loss modulus was 0.28 ± 0.1 MPa at 1 Hz and 4.1 ± 1.2 MPa at 3800 Hz. Taken the direction-dependent mechanical properties of TM into consideration, Luo et al., 2009 reported the mechanical properties of human TM in both radial and circumferential directions at high strain rates measured by split Hopkinson tension bar (SHTB). The results showed that the Young's modulus of human TM is 45.2–58.9 MPa in the radial direction, and 34.1–56.8 MPa in the circumferential direction at strain rates 300–2000 s^{-2}, which is closely related to the distribution of the fiber network in the lamina propria.

The mechanical properties of normal human TM have been reported, however, there is a necessity to expand this type of measurement to the diseased and injured TM to investigate the role of TM in the situation where conductive hearing loss happened. For example, the TM mobility significantly decreased in the ears with otitis media (Guan et al., 2014, 2017). Histologic measurement and biomechanical measurements reveal the structural alternation induced by the infection is one of the major contributors to the conductive hearing loss resulted by the otitis media (Guan et al., 2015; Yokell et al., 2015). When exposed to the blast overpressure, the damage in TM also induced in the

conductive hearing loss, however, quantitative measurement on the mechanical properties

of TM after blast damage was limited.

1.3 Blast-induced damage to the middle ear

The increasing number of terroristic bombing attacks in the last few decades has

led to an increasing frequency of blast injuries in civilians as well as military personnel

(Champion et al., 2009; Mathews and Koyfman, 2015; Yeh and Schecter, 2012). In the

first decade of 21st century, the number of casualties of illegal bombing attacks has been

increased significantly (Fig. 1.7). There is an urgent requirement to understand the

mechanism and treatment of blast-induced injuries.
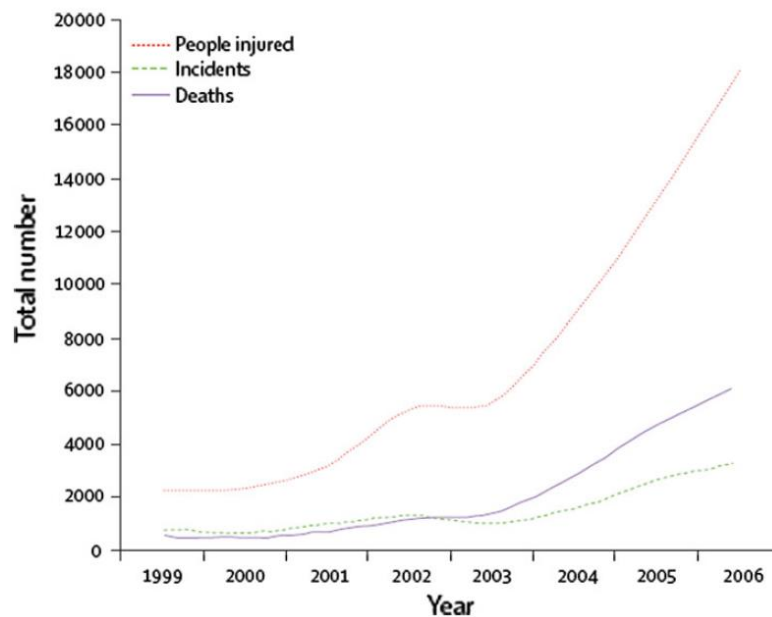
Figure 1.7 Worldwide trends in terrorist explosive events from 1999 to 2006 (Wolf et al., 2009)

1.3.1 Blast overpressure

Blast overpressure is defined as an abrupt disturbance in the ambient air pressure.

The typical waveform of the blast overpressure is called a Friedlander wave as shown in

Fig. 1.8. It starts with a sharp positive impulse which decays rapidly and is followed by a

prolonged negative pressure (Bauman et al., 2009). A typical free-field explosion generates blast waves which propagate radially from the source. In the places which were close to the source, the pressure history is very turbulent and unpredictable. The formation of Friedlander wave requires a certain distance away from the center of the blast (Chandra et al., 2012). The peak pressure generated by the explosion is inversely related to the distance cubed from the blast site. The blast wave is followed by a "blast wind" composed of compressed air which is usually strong enough to lift its victims and results in further injuries.
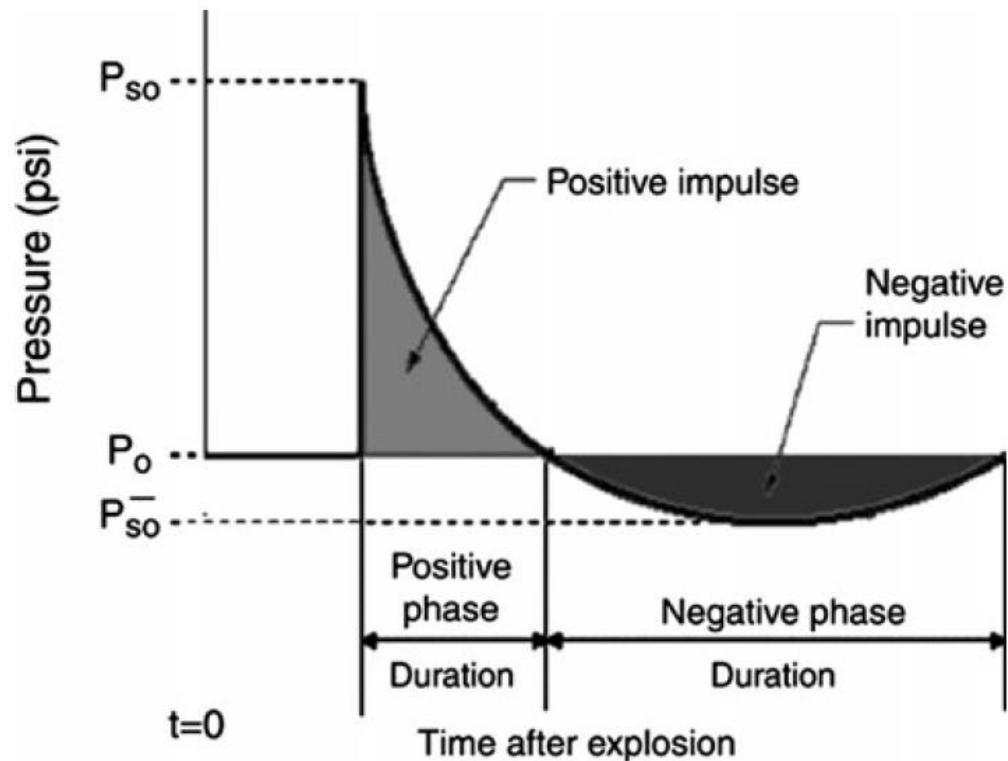
Figure 1.8 Friedlander wave(Bauman et al., 2009)

The injuries resulted from the blast overpressure are classified as classified as primary, secondary, tertiary, and quaternary. Primary blast injury is defined as the damage resulted directly from the interaction between the blast wave and the organ inside the body. Organs with the air-fluid interface, especially the ear and lung, are at particular

14

risk. Secondary blast injury is a result of penetrating injury caused by the debris or fragments created by the explosions. Tertiary and quaternary blast injuries are indirectly damage resulted from the explosion to the victims such as falling or collapsed structure and other possible injuries such as burns and asphyxia. This study focuses on the analysis of the primary blast injuries in the human auditory system.

1.3.2 Damage to the middle ear soft tissues induced by blast exposure

Due to the intrinsic structure, the ear is the most vulnerable organ when exposed to the overpressure (Gan et al., 2016; Mathews and Koyfman, 2015; Mayorga, 1997; Patterson and Hamernik, 1997; Yeh and Schecter, 2012). The rupture of TM is the most common primary blast injury and is usually considered as a sign of the blast pressure which has exceeded the threshold of resulting in possible lethal damage to organs other than the ear (especially lung) (Mathews and Koyfman, 2015). In one British report of a terrorist bombing in Northern Ireland, 45% of those who died from the blast had shown ruptures in the TM (Phillips and Richmond, 1991). As reported by Ritenour and Baskin, 2008, up to 47% of the survivors of the blast have shown ruptured TM. Disruption of the ossicles, especially the disarticulation of the ISJ are also observed in the victims of the blast exposure (Keller et al., 2017; Patterson and Hamernik, 1997). Choi (2012) reported that 34% of the ears undergoing tympanoplasty after blast exposure showed damage to the ossicular chain such as the disruption of the ISJ and incudomalleolar joint. However, not all damage is discernable right after the blast exposure. Injury to the tympanic membrane and ossicular chain occurs at pressure levels above those that injure the inner ear (Patterson and Hamernik, 1997). The damage to the inner ear can result in more severe hearing loss and other symptoms. The rupture of the TM can result in 0-30 dB conductive

15

hearing loss at low frequencies and 40-80 dB at high frequencies while the injuries in the inner ear may be irreversible and cause a hearing loss at a level of 0-100 dB (Mayorga, 1997).

Even though damage to the middle ear is observed in blast-injured ears, the role of ISJ and TM and their behavior under blast exposure remains unclear. The nonlinear transfer function of the middle ear has been observed under high-intensity stimulus (Cheng et al., 2017; Greene et al., 2017). However, there is no certain answer to the question that how do the TM and ISJ contribute to the nonlinearity of the middle ear under high-intensity sound pressure or blast overpressure due to the lack of knowledge about the behavior of the middle ear under blast conditions. Moreover, the detailed mechanism of how the damage was induced in TM and ISJ is also poorly understood which makes the prevention of the damage difficult. Therefore, there is a necessity to investigate the behavior of the TM and ISJ under blast overpressure.

As we reported in the section 1.2.1, the mechanical properties of ISJ were only measured under quasi-static conditions which indicated the dynamic properties of ISJ and its behavior under blast overpressure remains unclear. Although the mechanical properties of TM have been reported in both static and dynamic tests by several methods, the properties of TM in blast-damaged ear have not been investigated. Recently published results indicated that in TMs experienced low-pressure blast but were not ruptured, the microstructural level damage could change mechanical properties of the tissue as shown in Fig. 1.9 (Engles et al., 2017; Luo et al., 2016). The measurement on the rectangular strip harvest from TM indicated the storage and loss modulus of decreased significantly after the blast exposure (Engles et al., 2017). The microstructural damage was also found

to be direction-dependent (Luo et al., 2016). The Young's modulus of the post-blast TMs was reduced in the circumferential direction, while the modulus in the radial direction was reduced only at low strain rate. However, the relationship between the damaged fibers and the changed material properties of the tissue is not explicitly explained. The impact of the blast-induced microstructural damage on the sound-transmission function of the entire TM has not been thoroughly investigated.
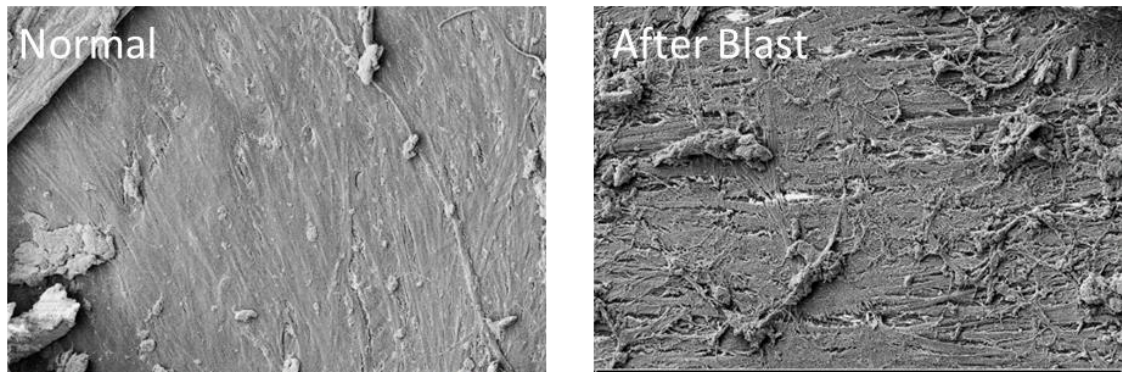
Figure 1.9 TM surface under Scanning electron microscopy before and after blast exposure.(Engles et al., 2017)

1.4 Objectives

Blast-induced hearing loss greatly reduces the quality of life of military personnel. However, the response of the ear to the blast overpressure is not well understood. Biomechanical measurement on the human ear under blast exposure is critical to improving our understanding of the mechanism and prevention of the damage. Moreover, FE models of the human ear is a practical tool to investigate the blast-induced damage and simulate the behavior of the ear under blast conditions. However, the dynamic properties of ISJ and the multilayer structure of TM have not been measured or investigated. The aim of this study is the investigate the behavior of human ISJ and TM

in normal and blasted ears and provide quantitative data for improving the FE models of the human ear for blast simulation.

1) To measure the mechanical properties of human ISJ in auditory frequency range and use FE model for data analysis to understand the structure-function relationship of ISJ in the normal ear

2) To measure the mechanical properties of the human ISJ under high strain rate to understand the behavior of the joint under blast exposure

3) To characterize the microstructural level mechanical properties change in TM by measuring the TM surface motion change after blast exposure

4) To characterize the response of the middle ear under blast overpressure by measuring the real-time movement of the TM under the blast.

1.5 Outline

Chapter 2 presents the measurement of human ISJ dynamic properties using frequency-temperature superposition method.

Chapter 3 presents the measurement of mechanical properties human ISJ under high strain rate deformation using miniature split Hopkins tension bar (SHTB).

Chapter 4 presents the measurement of human TM surface motion before and after blast exposure using scanning laser Doppler vibrometry (SLDV) combining with FE simulations.

Chapter 5 presents the motion of human TM under blast overpressure measured by dual-laser setup.

Chapter 6 presents the summary of this study and future studies.

Table 1.1 Table of abbreviations

TM	Tympanic membrane
ISJ	Incudostapedial joint
SAL	Stapedial annular ligament
FE	Finite element
PF	Pars flaccida
PT	Pars tensa
TB	Temporal bone
DMA	Dynamic mechanical analyzer
FTS	Frequency-temperature superposition
WFL	Williams–Landel–Ferry
SHTB	Split Hopkinson tension bar
SLDV	Scanning laser Doppler vibrometry
LDV	Laser Doppler vibrometry

Chapter 2   Dynamic properties of human incudostapedial joint—

Experimental measurement and finite element modeling

2.1 Introduction

Due to the limited published data of the mechanical properties of human incudostapedial joint (ISJ) and the importance of ISJ mechanical properties to the sound transmission function of the human ear, we report the dynamic properties of human ISJ using a dynamic mechanical analyzer (DMA, ElectroForce 3200, Bose, Eden Prairie, MN) with frequency–temperature superposition (FTS) in this chapter. DMA is a widely used system to measure dynamic properties of materials in the frequency domain. However, the testing frequency of the current commercial DMA has limited high-frequency access and a method to expand the working frequency to higher levels, the FTS principle has been reported (Ferry, 1950; Williams et al., 1955). The FTS principle is an empirical method which relates the effect of temperature change on dynamic properties of some materials (e.g. polymers) to that of frequency change (Ferry, 1980; Landel and Nielsen, 1993). In the recent two decades, researchers have applied FTS principle in dynamic tests of biological tissues including the bovine brain and vocal-fold (Chan, 2001; Miri, 2014; Peters et al., 1997). Recently, our lab has reported the mechanical properties of the human TM, human SAL, and chinchilla SAL measured using DMA with FTS to extend measured complex modulus data of tissues to higher frequencies (Hitt et al., 2017; Zhang and Gan, 2012, 2014).

In this chapter, the DMA with FTS was used for measuring dynamic properties of the human ISJ. Experiments were conducted in the frequency range of 1–80 Hz at three

different temperatures (5, 25 and 37 °C). The average complex modulus of the ISJs was obtained directly from the experiments. A 3D FE model of the ISJ consisting of the articular cartilage, joint capsule and synovial fluid was then constructed to identify the mechanical properties of ISJ components by matching the modeling results to the experimental data. The model was used to investigate the contribution of the mechanical properties of the ISJ (the capsule and synovial fluid) to the behavior of the joint under dynamic load.

2.2 Methods

2.2.1 Specimen preparation and experimental setup

Eight (four left and four right) fresh human temporal bones (TBs) with an average donor's age of 69 years were involved in this study. All TBs were provided by Life Legacy Foundation, a certified human tissue supplier for medical and military research. The experiments were conducted within seven days after the TBs were received. The TB samples were covered by wet paper, soaked in a prepared solution made of 0.9% saline and 15% povidone at 5 °C to maintain the physiological condition before the experiment. Light microscope examinations were conducted on each TB to ensure that the middle ear appeared normal. The middle ear ossicles were then exposed by opening the tegmen tympani and removing the TM together with the malleus. The scala vestibule of the cochlea was opened and the stapes footplate was exposed through the medial side. The TB specimen was then trimmed to a cube with a size of 1.5 cm ×1.5 cm ×1.5 cm. A #11 scalpel was used to cut along the SAL to separate the footplate from the oval window. The ISJ was kept unstretched during the separation process of the footplate from the bony

21

wall. Finally, the stapedial tendon was removed to assure the ISJ was the only stress-bearing soft tissue in the test.

The schematic diagram of the experimental setup is shown in Fig. 2.1A. The ISJ specimen was fixed onto a sample holder using copper wire and melted paraffin. The load cell (5 lb, WMC-5-455 Bose, Eden Prairie, MN) of the DMA (ElectroForce 3200, Bose, Eden Prairie, MN) was placed between the sample holder and the X–Y translational stage. The translational stage was used for aligning the ISJ with the load cell in the Z axis under a surgical microscope (Zeiss, OPMI 1-FC), viewing from the front and lateral directions. The long process of the incus was fixed to the middle ear bony wall using cyanoacrylate gel glue. This type of glue had been validated by previous studies to provide stable fixation on the surface of biological tissues (Zhang and Gan, 2010). After the glue dried, a sharp-tip tweezer was used to assure the incus was completely immovable. The specimen was then raised up to a position where the stapes footplate was directly in contact with the lower end of the adapter. Cyanoacrylate gel glue was applied between the stapes footplate and the wooden adapter connected to the upper grip of the DMA (Fig. 2.1B). During this process, the ISJ stayed straight as shown in Fig. 2.1B indicating the structure was intact before the experiment. After the glue dried, a preload of 0.02 N compression was applied on the ISJ specimen before the experiment was started to assure all samples were tested under the same initial conditions. The preload was zeroed out before the start of the dynamic tests. The specimen was placed in a temperature-controlled chamber with a size of 25 cm ×25 cm ×10 cm (Fig. 2.1A). The fluctuation of the temperature inside the chamber during the test was controlled within ±1 °C by a system consisting of a thermocouple, a negative feedback circuit and a fan delivering hot or cold

22

air. For the dynamic measurements, sinusoidal displacements with an amplitude of 0.1 mm at the frequencies of 1, 2, 5, 10, 20, 40, 60 and 80 Hz were applied on the stapes footplate, and the force was measured by the load cell. Each measurement was performed at three temperatures: 5, 25 and 37 °C. The moisture of the specimen was maintained by adding 0.9% saline solution every five minutes onto the specimen using a syringe. At each frequency and temperature, results recorded in the first five seconds of the test were abandoned to serve as the preconditioning process. Therefore, each dynamic test itself included the preconditioning process with exactly the same testing conditions.
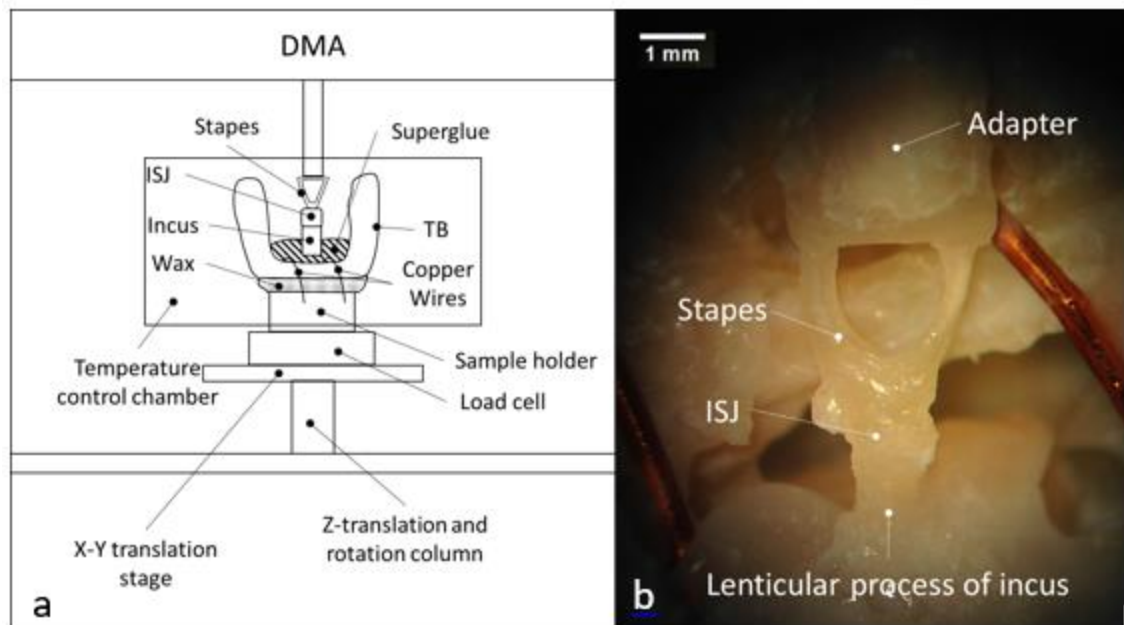
Figure 2.1 (a) Schematic diagram of the experiment setup. (b) ISJ specimen mounted on the machine observed under a microscope.

2.2.2 Dimensions and viscoelastic material model of ISJ specimen

The ISJ was separated after the completion of the dynamic test. The lenticular process of the incus and the head of the stapes were examined under a microscope. Images of the lenticular process of the incus were captured by a digital camera through the

microscope (Fig. 2.2). The stapes head was assumed to share the same geometry with the lenticular process of the incus based on the histological images provided by Zhang and Gan, (2010). Under the assumption that the cross-section of the ISJ was elliptical, the lengths of the long axis a and short axis b were measured by image analysis software (ImageJ). The measurement was based on a calculation of the pixels with a scale calibrated by a standard 1 mm scale bar next to the specimen as shown in Fig. 2.2. The largest values of a and b in perpendicular directions were accepted and the cross-sectional area of the ISJ was calculated by $A = \pi ab /4$. Table 2.1 lists the geometry data from eight ISJ specimens with the mean and standard deviation. The length of the ISJ could not be measured by direct observation. Therefore, we used the value of 0.28 mm, which was the length of the ISJ capsule measured from a histology section reported by Zhang and Gan, (2010). Based on the dimensions of each specimen, the ISJ was initially assumed as an isotropic viscoelastic body to derive its complex modulus. Even though the quasi-static test of the ISJ reported the nonlinear behavior of the ISJ, the material model of the joint can still be considered as linear viscoelastic in this study because the deformation is small. Both the displacement d applied on the stapes footplate and the force F measured with the load cell were sinusoid signals for each frequency f, defined as

$$d = d_0 e^{i2\pi ft} \tag{2.1}$$

$$F = F_0 e^{i(2\pi ft+\delta)} \tag{2.2}$$

where d_0 and F_0 are the amplitude of the displacement and force, respectively, and δ is the phase delay between the displacement and force. The complex modulus at frequency f is calculated by

$$|E^*| = \frac{\sigma_0}{E_0} = \frac{F_0/A}{d_0/L} \tag{2.3}$$

$$E' = |E^*|\, cos\delta \qquad\qquad (2.4)$$

$$E'' = |E^*|\, sin\delta \qquad\qquad (2.5)$$

where σ_0, E_0, A, L, E^*, E', and E'' are the stress amplitude, strain amplitude, cross sectional area, length, complex modulus, storage modulus, and loss modulus of the ISJ, respectively. The inner structure and the mechanical properties of joint components were

ISJ specimen (N=8)	1	2	3	4	5	6	7	8	Mean	SD
Length: a (mm)	0.95	0.80	0.87	0.86	1.01	0.93	0.91	1.02	0.92	0.07
Width: b (mm)	0.65	0.57	0.65	0.60	0.71	0.68	0.75	0.70	0.66	0.06
Cross sectional area: A (mm^2)	0.48	0.36	0.44	0.41	0.56	0.50	0.54	0.56	0.48	0.07

not taken into consideration at this step.

Table 2.1 Dimensions of the ISJ specimens.
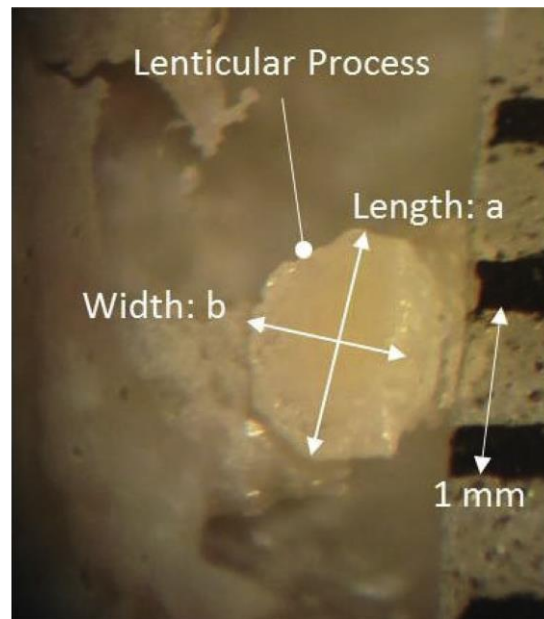
Figure 2.2 Microscopic image of the lenticular process of the incus after the dynamic test for geometric measurement

2.2.3 FTS principle

The FTS principle was employed to expand the frequency range of the experimental results. The FTS principle states that the curves of the complex modulus E^* obtained at a reference temperature T_0 (37 °C) can be expressed by

$$E^*(T_0, f) = E^*(T, f/\alpha_T) \tag{2.6}$$

where T is a lower temperature (5 or 25 °C), α_T is the shift factor quantifying the temperature's effect on a material's dynamic properties. The shift factor α_T must comply with the WLF equation which was first introduced by Williams, Landel and Ferry and widely used for the FTS principle

$$log_{10}\alpha_T = \frac{c_1(T-T_0)}{c_2+T-T_0} \tag{2.7}$$

where T and T_0 are the absolute temperatures in Kelvin. c_1 is a dimensionless constant and c_2 is a constant with a unit of Kelvin. c_1 and c_2 are empirical constants used to evaluate whethether the temperature shift is acceptable.

In order to use the FTS principle, the complex moduli measured from ISJ specimens at 5, 25 and 37 °C were first plotted as a function of frequency in a logarithmic coordinate system. Then the 25 °C curves were shifted together horizontally toward higher frequencies to align with the curves obtained from 37 °C (reference temperature). Subsequently, curves from 5 °C were shifted in the same way further horizontally to connect with the points belonging to the shifted 25 °C curves. In adjacent areas, the high-frequency results obtained from the higher temperature tests were connected with the low-frequency results obtained from the lower temperature tests. Note that the shapes of the curves were horizontally stretched (37 °C) and shrunken (25 °C) in the shifting process. Finally, the master curves of complex moduli at the reference temperature were

obtained. The values of α_T, c_1 and c_2 could be determined by Eqs. (2.6) and (2.7). There are three requirements in this shifting process for the FTS principle to hold: (1) the shifted curves in adjacent areas have to be matched perfectly with the curves from the lower temperature; (2) the shift factors for both loss and storage modulus curves are the same; (3) the shift factors have to obey the WLF equation, or in other words, values of c_1 and c_2 should have a small standard deviation among all specimens (Ferry, 1980; Hitt et al., 2017; Landel and Nielsen, 1993; Zhang and Gan, 2012, 2014).

2.2.4 Finite element model of ISJ

ISJ is a synovial joint with a complex inner structure. The relationship between the measured mechanical properties of the joint as an isotropic body and the mechanical properties of the components inside the joint requires further investigation. In this study, a 3D FE model of the ISJ was developed to attempt to identify the properties of the joint component. The structure of the FE model was similar to the one built in our previous study. Figure 2.3 shows the longitudinal cross-sectional (X-Z plane) view of the model with boundary conditions. The structure of the FE model was constructed based on the histology section shown in Fig. 2.4. The X-Y plane cross-section of the model was elliptical and X-axis represented the long axis. The length of the long and short axis was 0.92 and 0.66 mm, respectively, which were the mean values listed in Table 2.1. The thickness of the incus and stapes in this model were assumed to be 0.04 and 0.08 mm, respectively. The distance between the incus and stapes was $L = 0.28$ mm and the thickness of the capsule was $m = 0.08$ mm. The thickness of the cartilage covering the lenticular process and stapes head was set as $h = 0.08$ mm. The distance between the two cartilage layers was $D = 0.12$ mm.

The FE model was meshed with hexahedral elements in ANSYS 15.0 (ANSYS Inc., Canonsburg, PA). The lenticular process, stapes, and cartilage were assigned as linear elastic Solid 45 elements. The capsule was modeled by nonlinear Solid 185 elements of viscoelastic material and the synovial fluid was modeled as Fluid 80 elements with a constant viscosity. The mechanical properties used in the model are listed in Table 2.2. The Young's modulus of 14.1 GPa was used for the bony structures, incus, and stapes. The cartilage was considered as a linear elastic material with Young's modulus of 10 MPa, the same value as that used by Zhang and Gan, (2010). The bulk modulus and the viscosity of the synovial fluid were obtained from Zhang and Gan, (2010) as well.

The function of the ISJ largely depended on the properties of the joint capsule, and the viscoelastic properties of the joint capsule significantly affected the behavior of the ISJ over a frequency range of 600 to 6000 Hz (Gan and Wang, 2015). Therefore, the capsule was assumed to be viscoelastic and the values listed in Table 2.2 were determined by fitting the FE model-derived force-displacement curves with the experimental results. The generalized Maxwell model was used to represent the viscoelastic behavior of the capsule as

$$E'(\omega) = E_0 + \sum_{i=1}^{n} E_i \tau_i^2 \omega^2 / [1 + \tau_i^2 \omega^2] \tag{2.8}$$

$$E''(\omega) = \sum_{i=1}^{n} E_i \tau_i \omega / [1 + \tau_i^2 \omega^2] \tag{2.9}$$

where ω is the circular frequency (ω = $2\pi f$) and n equals to 3 (giving seven parameters $E_0, E_1, E_2, E_3, \tau_1, \tau_2, \tau_3$) (Hitt et al., 2017; Oskui and Hashemi, 2016; Zhang and Gan, 2014). The reason for using 7 parameters was to fit the experimental data at high frequencies which was difficult to accomplish using 5 parameters. A harmonic analysis with the same boundary conditions and frequency was conducted to simulate the dynamic

test. An iteration process was conducted to determine mechanical properties of the joint capsule by comparing the model-derived curves with the experimental data.
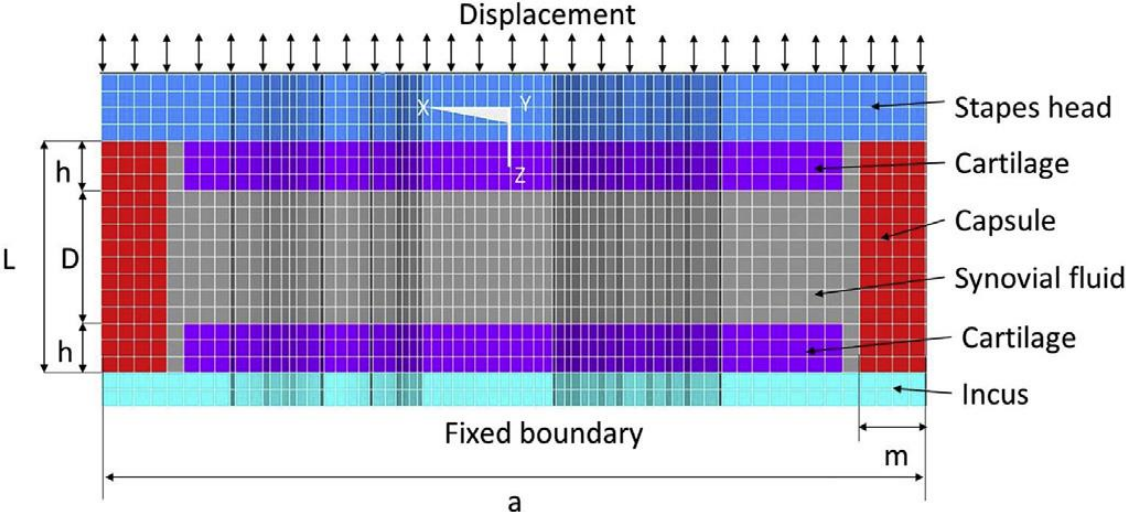
Figure 2.3 Axial cross section (X –Z plane) of the 3D FE model of the ISJ with boundary conditions.
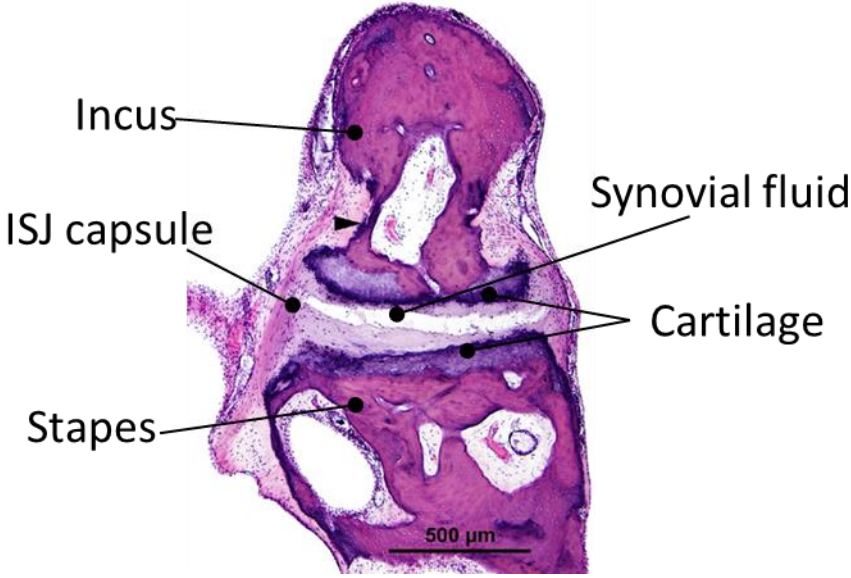
Figure 2.4 Histology section of human ISJ (Karmody et al., 2009)

Table 2.2 Components and mechanical parameters of the ISJ FE model.

Components	Young's modulus (Pa)	Poisson's ratio	Viscosity (cp)
Incus	1.41×10^{10}	0.3	
Stapes head	1.41×10^{10}	0.3	
Cartilage	1.00×10^{7}	0.3	
Capsule	$E_0 = 2.9$ MPa, $E_1=1.25$ MPa, $E_2= 1.9$ MPa $E_3= 0.12$ MPa, $\tau_1= 2.6$ ms, $\tau_2 = 0.14$ ms $\tau_3= 0.13$ ms	0.3	
Synovial fluid	2.20×10^{9} (Bulk modulus)		4×10^{2}

2.3 Results

2.3.1 Complex modulus from dynamic tests

Dynamic tests were conducted on eight ISJ specimens to obtain their storage modulus E' and loss modulus E''. Two typical results obtained from specimens ISJ-6 and ISJ-8 are shown in Fig. 2.5. The storage and loss modulus measured at each frequency point at different temperatures were plotted in the logarithmic coordinate system. Generally, the storage and loss modulus increased with increasing frequency or decreasing temperature. The loss modulus changed rapidly at frequencies below 5 Hz at 37 °C tests. Relatively large slopes were observed at high frequencies ($f >10$ Hz) in both storage and loss modulus at all three temperatures. The complex modulus of other ISJ specimens showed similar curves to those in Fig. 2.5.
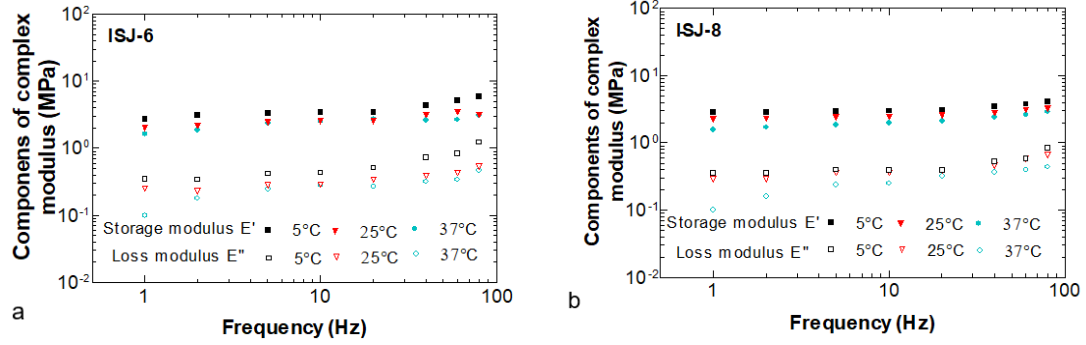
Figure 2.5 The components of complex modulus curves obtained from the dynamic tests of ISJ specimens. (a) Data acquired from ISJ-6. (b) Data acquired from ISJ-8. The curves of the complex moduli at 5 and 25 °C were shifted to high frequencies

following the FTS principles. The master curves of samples ISJ-6 and ISJ-8 are displayed in Figs. 2.6a and 2.6b, respectively. For specimen ISJ-6, the storage modulus was 1.63 MPa at 1 Hz and increased to 5.97 MPa at 15 kHz, while the loss modulus increased from 0.10 MPa to 1.23 MPa. For specimen ISJ-8, the storage modulus was 1.58 MPa at 1 Hz and increased to 4.15 MPa at 15 kHz, while the loss modulus increased from 0.10 MPa to 0.85 MPa. In Fig. 2.5, the complex modulus-frequency curves were smoothly connected at the adjacent area without discernible discontinuities. Therefore, the master curves were generally well-matched which satisfied the first requirement of the FTS principle. Occasional fluctuations of the loss modulus curves were caused by the instability of the DMA machine at 80 Hz tests. Both storage and loss modulus were shifted by the same α_T for each specimen, which satisfied the second requirement of the FTS. The shift factors, maximum frequencies and constants c_1 and c_2 obtained from eight samples were listed in Table 2.3. The mean value with SD of the shift factor from 5 to 37 °C (α_5) was 183 ± 13.4. The mean value with SD of the shift factor from 25 to 37 °C (α_{25}) was 15.5 ± 4.0. The maximum frequency ranged from 12.8 to 16.0 kHz, which could cover most of the human hearing frequency range. The SD of c_1 and c_2 were 2.8

31

and 17.2 K, respectively, which were smaller than the values in Zhang and Gan, (2014).

Therefore, the third requirement of the FTS is satisfied.
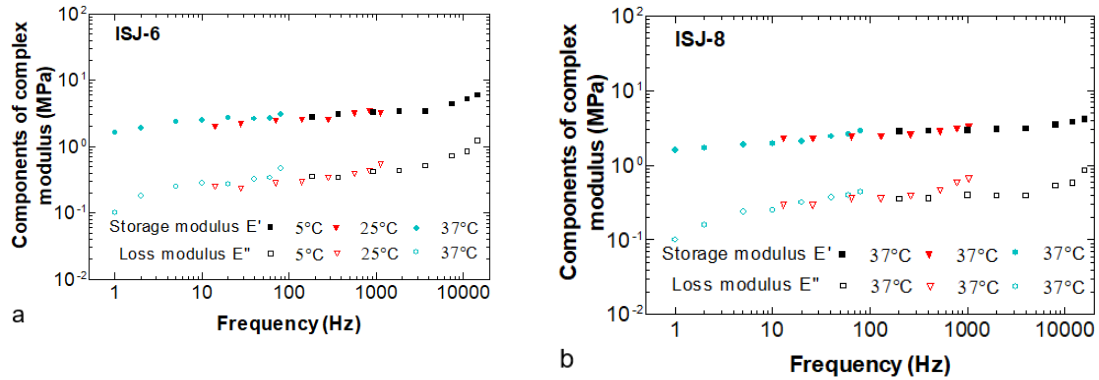
Figure 2.6 Two representative master curves of the components of complex modulus at a reference temperature (37 °C) obtained by FTS principle. (a) Data acquired from specimen ISJ-6. (b) Data acquired from specimen ISJ-8.

The master curves of the complex modulus of all eight ISJ samples were shown in Fig. 2.7. The mean complex modulus was calculated over the frequency range from 1 Hz to 8 kHz, the common frequency range for the eight ISJ samples. Frequencies below 8 kHz is a common range of interest in research on middle ear mechanics. At 1 Hz, the mean storage modulus with SD was 1.14 ± 0.53 MPa and the loss modulus was 0.07 ± 0.04 MPa. At 8 kHz, the storage modulus was 3.01 ± 1.06 MPa, and the loss modulus was 0.47 ± 0.17 MPa. The mean curves in Fig. 2.7 indicate that the storage and loss modulus gradually increased with the frequency and the loss modulus had a larger slope than the storage modulus, especially at frequencies below 20 Hz. This trend shared some similarities with the viscoelastic behavior of other middle ear soft tissues reported in the previous studies about SAL (Zhang and Gan, 2014).

32

Table 2.3 The shift factors, c1 and c2 of WLF equation, and maximum frequency of human ISJ samples.

Specimen	1	2	3	4	5	6	7	8	Mean ± SD
α_{25}	12	15	23	11	18	14	18	13	15.5 ± 4.0
α_5	195	190	177	160	170	184	189	200	183 ± 13.4
$\ln \alpha_5$	5.27	5.24	5.17	5.07	5.13	5.21	5.24	5.29	5.20 ± 0.07
$\ln \alpha_{25}$	2.48	2.70	3.13	2.39	2.89	2.63	2.89	2.56	2.71 ± 0.24
c_1	16.1	11.9	8.4	15.3	9.6	12.5	10.2	14.6	12.4 ± 2.8
c_2 (K)	-65	-41	-20	-64	-27	-45	-30	-56	-44.1 ± 17.2
Maximum frequency (kHz)	15.6	15.2	14.1	12.8	13.6	14.7	15.1	16.0	14.6 ± 1.0
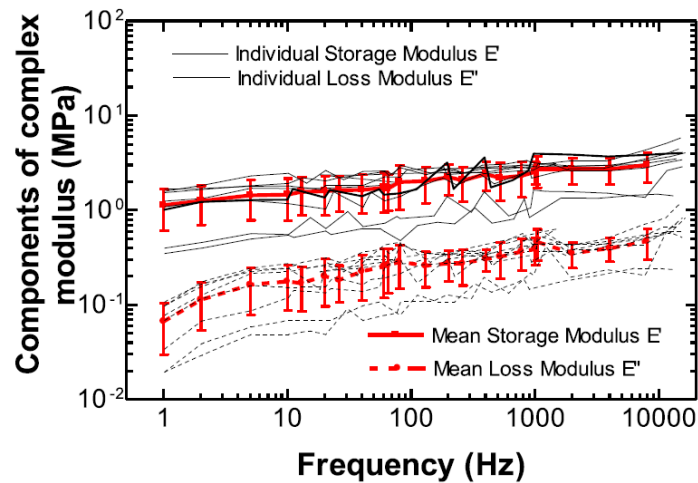
Figure 2.7 The master curves of the components of complex modulus at 37 °C from 8 ISJ samples and the mean master curves of the storage and loss modulus with SD.

2.3.2 FE model-derived data

The magnitude and phase of the force on the incus can be calculated by the complex modulus curves in Fig. 2.7 and the geometry data of the ISJ in Table 2.1 using Eqs. (2.1-2.5). By matching the FE model-predicted results to the experimental data, the mechanical properties of the joint capsule were determined and listed in Table 2.2. The

seven viscoelastic parameters for the ISJ capsule solved from the FE model were $E_0 =$ 2.9 MPa, E_1=1.25 MPa, E_2= 1.9 MPa, E_3= 0.12 MPa, τ_1= 2.6 ms, $\tau_2 = 0.14$ ms, and τ_3= 0.13 ms. The black solid line in Fig. 2.8a represents the mean (with SD) magnitude of the force on the incus measured from eight ISJ samples and the red broken line represents the result obtained from the FE model. The black solid and red broken lines in Fig. 2.8b represent the mean phase shift (with SD) between the displacement and the force obtained from the experiment and FE model, respectively. Overall, the model predicted results matched the experimental data except for phase values at frequencies below 10 Hz. Since 10 Hz is lower than the normal auditory frequency range, the deviations are acceptable. Note that in the frequency range of 10-80 Hz where the results were directly obtained from the experimental data without any extrapolation by the FTS principle, the experimental data and model prediction still matched well. The good matching between the experimental and model-derived data suggested that the generalized Maxwell model (n=3) was able to characterize the viscoelastic behavior of the joint capsule over the auditory frequency range.
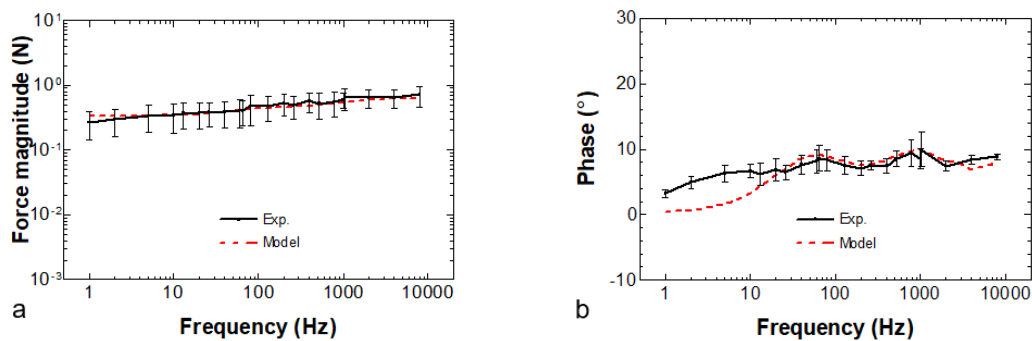
Figure 2.8 Comparison between the forces on the lenticular process of the incus obtained from experimental-derived master curves and the FE model simulation. (a) The force magnitude–frequency curves. (b) The phase–frequency curves.

34

2.4 Discussion

2.4.1 Comparison with published data

To the best of my knowledge, though the mechanical properties of human ISJ under quasi-static loading conditions were reported (Zhang and Gan, 2010), there was no published data on dynamic properties of the ISJ in human or experimental animals by the time this paper was composed. Results from tension, compression, and stress relaxation tests by Zhang and Gan, (2010) demonstrated that the human ISJ exhibited typical viscoelastic behavior. Considering the displacement amplitude used in the present dynamic test was 0.1 mm, the average elastic modulus obtained from the 0.1 mm quasi-static tension and compression reported by Zhang and Gan, (2010) was used for comparison. The mean storage modulus at 1 Hz (lowest testing frequency) in current experiment is 1.14 MPa (Fig. 2.7) and the result from quasi-static tests was approximately 1.17 MPa. Considering the strain rate of the sample in 1 Hz dynamic test was comparable to the condition of the quasi-static test, the mechanical properties of ISJ obtained in this study matched well to that reported in the previous study.

2.4.2 Contribution of the FE model of ISJ

Even though the quasi-static properties of the ISJ and the analysis of ISJ structural effect on middle ear transfer function have been reported, the dynamic properties of the joint remain unknown. In this study, the complex modulus of ISJ was obtained experimentally, and the mechanical properties of the joint capsule were predicted through the FE model of ISJ. To compare the ISJ mechanical properties obtained in this study with those used in the published FE models of the human ear, the ISJ model in Fig. 2.3 was replaced by two solid models of ISJ: linear elastic and viscoelastic replaced by two

solid models of the ISJ: linear elastic (Gan and Wang, 2007) and viscoelastic (Zhang and Gan, 2013), respectively. The linear elastic model of ISJ was based on the material properties used by Gan and Wang, (2007) with a Young's modulus of 0.6 MPa. The viscoelastic ISJ model was based on the material properties reported by Zhang and Gan, (2013) as the standard linear viscoelastic material with E_0= 0.4 MPa, E_1= 20 MPa, and τ_1= 20 μs. Figure 2.9 shows the results of two material models of the ISJ in comparison with the experimental data and FE model results of this study. As shown in Fig. 2.9a, the linear elastic ISJ is unable to simulate the frequency-dependent behavior of the joint, and there is no phase shift for the linear elastic ISJ in Fig. 2.8b. The force magnitude derived from the viscoelastic ISJ is lower than the experimental results at low frequencies and higher at high frequencies (f > 800 Hz). The phase angle of the derived force on the joint shown in Fig. 2.9b displays a huge increase at f > 30 Hz when the ISJ was molded as a viscoelastic material. This indicates that the absence of the synovial fluid, cartilage, and viscoelastic joint capsule may not represent the dynamic behavior of the ISJ over a broad frequency range. However, a future study on using dynamic properties of the ISJ in the human ear model may provide more insights for ISJ mechanical function for sound transmission. Figure 2.9 demonstrates that the model results can be used to simulate the ISJ in the human middle ear model with higher accuracy comparing to previous models over the auditory frequency range.
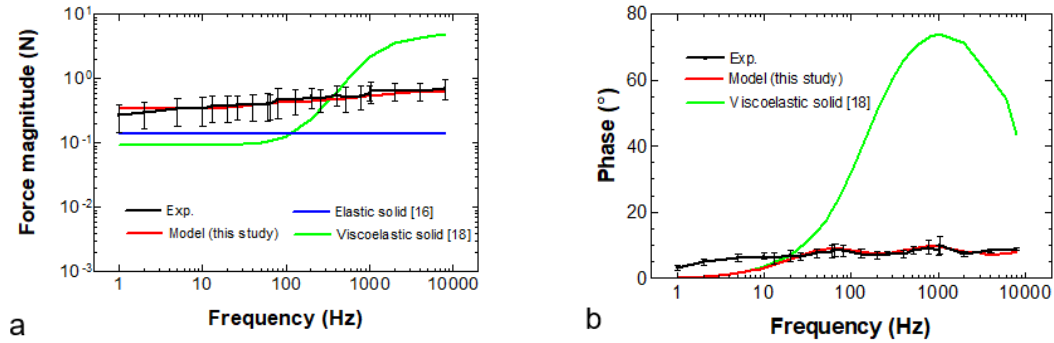
Figure 2.9 Comparison between the forces on the lenticular process of the incus obtained from experimental-derived master curves and the FE models based on different material properties. (a) The force magnitude–frequency curves. (b) The phase–frequency curves.
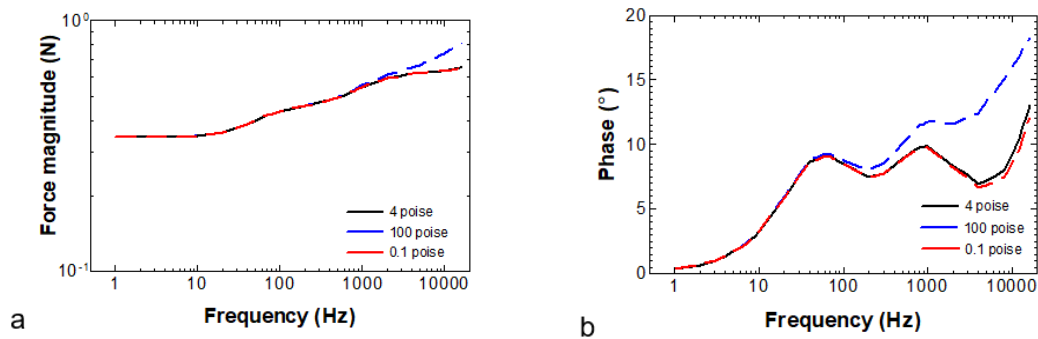
Figure 2.10 Curves describing the force on the lenticular process of incus derived from the FE model simulation with different levels of synovial fluid viscosity. (A) The force magnitude–frequency curves. (B) The phase–frequency curves.

In addition to providing the values of mechanical properties of the joint components, the FE model of the ISJ may also be used to evaluate the contribution of each component to the overall stiffness of the joint over the frequency range. The previous ISJ modeling suggested that the behavior of the joint was sensitive to the viscosity of the synovial fluid. To confirm this observation, we conducted an analysis in the current ISJ model by varying the viscosity of the synovial fluid from 100 to 0.1 poise and calculating the force induced on the incus over frequencies of 1 Hz to 8 kHz as shown in Fig. 2.10. The model-derived force magnitude in relation to frequency is shown in Fig. 2.10a and

37

the phase shift between the displacement and force is shown in Fig. 2.10b. Note that the viscosity of the synovial fluid inside the articular joint changed from 100 to 0.1 poise when the shear rate increased from 0 to 5000/s due to the shear-thinning effect of the synovial fluid (Fung, 2013). During the deformation process of the ISJ, the synovial fluid experienced shearing. Based on a broad frequency range of the results in Fig. 2.10 (1 Hz to 8 kHz), the shear rate of the synovial fluid would increase with the testing frequency which might make the shear-thinning effect unneglectable. Considering that the frequency of the results in Fig. 2.10 was obtained by extrapolation, the values of the shear rate of the synovial fluid were difficult to be determined quantitatively from the frequency values. Therefore, values between 0 and 5000/s were used to make a qualitative estimation on the shear rate of the synovial fluid in the ISJs in this study to illustrate how the thinning effect of the synovial fluid will affect the behavior of the joint. The viscosity of 4 poise was used as the normal value for the synovial fluid used in this study. As shown in Fig. 2.10, there was no significant difference in magnitude or phase of the force at low frequencies. The fluid viscosity started showing effects on the force magnitude at 1 kHz (Fig. 2.10a) and on the phase at 60 Hz (Fig. 2.10b). It can be said that the synovial fluid is a typical bioviscoelastic fluid whose storage and loss shear modulus increase with the shear rate (Fung, 2013). In this study, the shear rate of the fluid is proportional to frequency in dynamic tests. Higher testing frequency results in higher storage and loss modulus of the synovial fluid, which increase the stiffness and energy dissipation of the entire ISJ structure. The change of mechanical properties of the ISJ was demonstrated by the increased force magnitude and phase of the incus in the FE model. Conclusively, the

38

viscosity of the synovial fluid contributes to dynamic behavior of the ISJ mostly at high frequencies.

This study is the first report on dynamic properties of the human ISJ and we attempt to describe the properties of ISJ components based on an FE model of the joint. However, the measurement of the ISJ geometry was relatively coarse, especially the parameters which are unable to be measured directly in this study, such as the m, L, h and D as shown in the model of Fig. 2.3. Zhang and Gan, (2011) reported that the thinner cartilage (h decreased) would result in a reduced compressive stiffness of the ISJ. Therefore, if the h value used in the FE model is lower than the value in the experiment, the viscoelastic parameters of the joint capsule (E_0, E_1) obtained from the simulation would be higher than the true values. Moreover, the thickness of the capsule m is not directly measured either. Given the displacement-force relationship obtained from the FE model unchanged, the stiffness of the joint capsule would be negatively correlated with the value of m. In our future studies, we will explore the optic coherence tomography technique for measuring the ISJ structure. The accurate morphological data of ISJ will improve not only the experimental results but also the FE model of the joint (Park et al., 2016). In addition to the ISJ's geometry parameters, the material properties of some components such as the cartilage are simplified as linear elastic in FE simulation. The frequent-dependent behavior of the cartilage was not involved in modeling analysis. The results provided by Zhang and Gan (2011) indicated that the stiffness of the ISJ increased with the elastic modulus of cartilage, but the effect was less significant than that of cartilage thickness. Gan and Wang (2015) suggested that the effect of the elastic modulus of the cartilage on the mobility of the incus was decreased with frequency if the cartilage

was linear elastic. Another recent study indicated that the transfer function of the middle ear was closely related to the pretension inside the ossicular chain (Koch et al., 2016). In this study, the pretension of the ossicular chain was released during the specimen preparation process and the initial status of the ISJ tested in the experiments was different from the physiological condition. In future studies, we may consider conducting the mechanical measurement with an intact ossicular chain.

2.5 Conclusion

Dynamic properties of human ISJ samples at 1–80 Hz were measured by DMA and the frequency range of the results was extrapolated by FTS principle to 8 kHz. The experimental data have been analyzed with an FE model of the joint. The mean value of storage modulus increased from 1.14 MPa at 1 Hz to 3.01 MPa at 8 kHz and the loss modulus increased from 0.07 MPa at 1 Hz to 0.47 MPa at 8 kHz. The 3D FE model of the human ISJ was used for identifying mechanical properties of the joint components by matching the model-derived data to the experimental results. The viscoelastic properties of the joint capsule were determined by using a 7-parameter generalized Maxwell model. The FE analysis indicated that the mechanical properties of the ISJ capsule and the viscosity of the synovial fluid affect the dynamic behavior of the joint. The results reported in this paper provide useful data for improving the accuracy of FE models of the human middle ear and contribute to a better understanding of the structure-function relationship of the ISJ.

Chapter 3   Mechanical Properties of Incudostapedial Joint at High Strain Rate Measured by Split Hopkinson Tension Bar

3.1 Introduction

The dynamic properties of human ISJ presented in chapter 2 indicate that the average complex moduli of the joint changed significantly over the frequency range. Therefore, the viscoelastic behavior of the joint suggests that the stiffness of the ISJ should be sensitive to the strain rate of the deformation. As mentioned in the first chapter, the disarticulation of ISJ is a typical blast-induced injury in the auditory system. It is important to understand the behavior the ISJ during the blast exposure. However, there is no published data on the mechanical properties of ISJ under high-strain-rate deformation as well as the real-time characterization of the behavior of the joint under impact load.

Split Hopkinson tension bar (SHTB) is a system designed for characterizing the tensile stress-strain response at high strain rate for materials. The SHTB has been used to measure the mechanical properties of a variety of engineering materials usually with high strength and toughness such as polymers (Chen et al., 2002; Fan et al., 2015) and composite materials (Gilat et al., 2002). Adjustment of the setup is necessary to deal with the problems from the measurement on soft material such as rubber because of the low strength, stiffness and wave impedance (Chen and Song, 2010; Nie et al., 2009). Therefore, to measure the dynamic properties of middle ear soft tissues with low strength, stiffness and toughness a specially designed miniature SHTB has been developed in our laboratory and the tests have been successfully conducted on normal and blast-injured human TM sample (Luo et al., 2009, 2016).

The stress-strain relationship of the sample obtained by the SHTB is based on the theory of one-dimensional propagation of the stress waves (Chen and Song, 2010). As shown in the Fig. 3.1, the apparatus consists of three parts a loading device, bar components, and a data acquisition and recording system. The loading device consists of the tubing striker, impact flange, and the pulse shaper. The friction between the tubing striker and the inside bar should be minimized. The bar components consist of an incident bar, a transmission bar, and a momentum trap bar. To ensure the one-dimensional wave propagation along the bars, the bars need to be long, physically straight, aligned in a line, and free to move on their supports with minimized friction. Typically all bars share the same diameter and material. The data acquisition and recording system consisting of two pairs of strain gages placed on the incident and transmission bars, two Wheatstone bridges, two signal amplifiers, and oscilloscope with the high sampling rate (>10 MHz). The strain gages are usually attached symmetrically on the surface of the bars across a bar diameter. The strain signals (millivolts level) collected by the strain gages are conditioned by the Wheatstone bridge. The data acquisition system needs to have a frequency response high enough for acquiring and processing signals shorter than one millisecond.
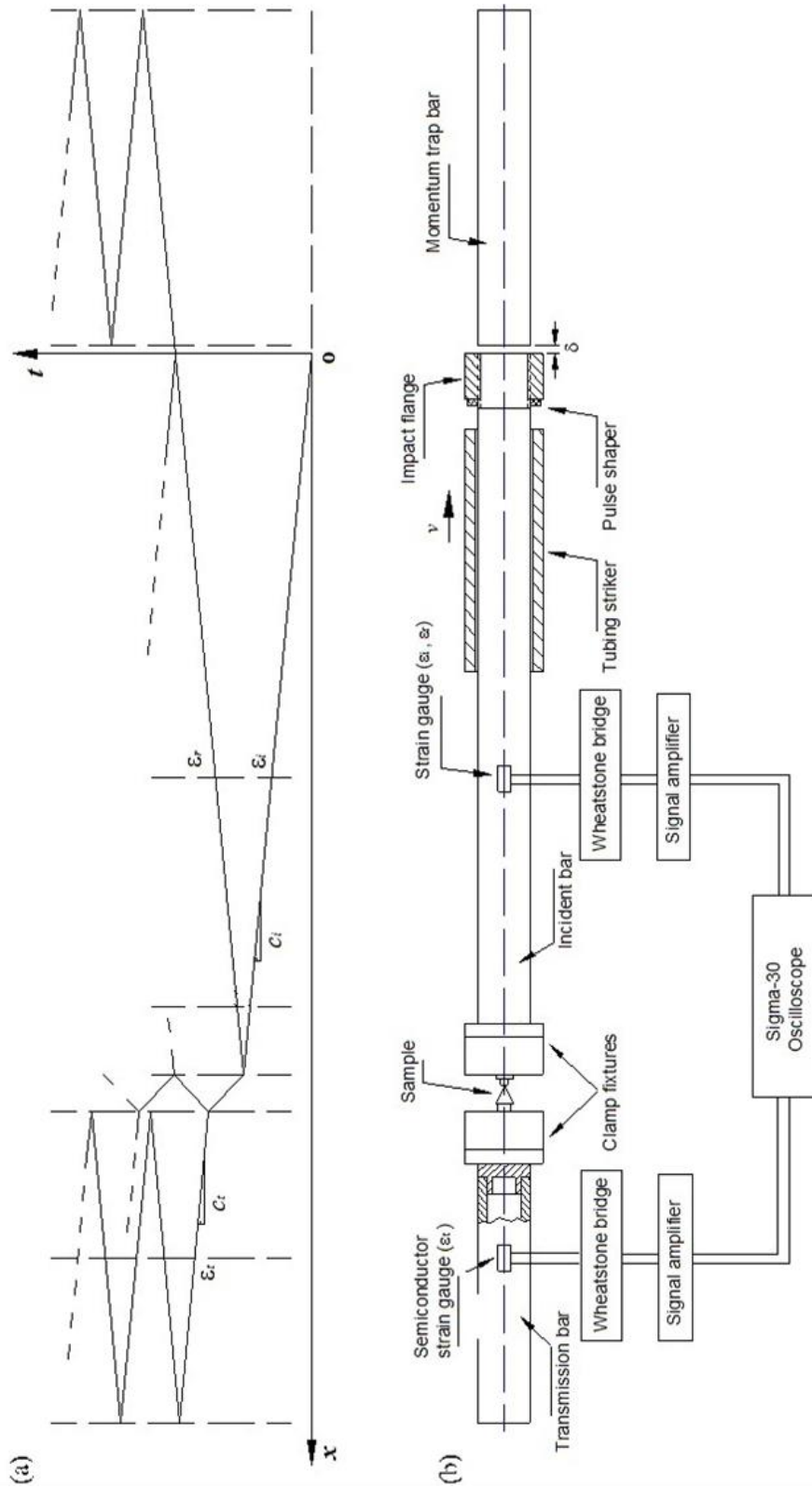
Figure 3.1 (a) X-t graph stress wave propagation along the SHTB and (b) Schematic diagrams of the design of the miniature SHTB in our laboratory. (Luo et al., 2009)

43

In a typical SHTB experiment, the high-strain-rate stress wave is generated by the impact between the striker tubing striker and impact flange as shown in the Fig. 3.1a at t = 0. The flange is sandwiched between the striker and the impact flange to improve the quality of the generated signal. Then the stress wave then propagates along the incident bar in direction of the arrow on the x-axis as shown in Fig. 3.1a. When the tension wave in the incident bar propagates to the interface between the incident bar and the specimen, part of it is reflected back into the incident bar while the rest transmits into the specimen. Due to the mismatch of the wave impedance between the specimen and the bars, the stress wave gets reflected back and forth inside the specimen. When the first time the tension wave reaches the interface between the specimen and the transmission bar, the reflection, and transmission of the stress wave happens again. The interaction of the stress waves in the specimen with the specimen-transmission bar interface builds the profile of the transmitted stress in the bar.

The initial incident pulse of tension wave is captured by the strain gauges located on the incident bar as well as the reflective pulse returned from the interface as a compression wave (Fig 3.1b). The stress wave propagates through the specimen to and the transmission is captured by the strain gages placed on the surface of the transmission bar. Assuming that the stress waves propagate in both the incident and transmission bars without dispersion, the pulses recorded at the strain gage locations represent those at the bar ends in contact with the specimen. Based one-dimensional stress wave theory, the particle velocities at both ends of the specimen can be expressed by the incident, reflected and transmitted strain pulses as shown in Equation 3.1 &3.2. The movement of the specimen in the relation to the incident reflected and transmitted strains are shown in the

Fig. 3.2 (Chen and Song, 2010). Note that even though the stress wave moves back and forth in the bars and specimen, only the first incident, reflected and transmitted signals are recorded for data analysis. The velocities at the end of the incident bar and transmission bar are v_1 and v_2 respectively. C_B is the speed of the stress wave in the bar.
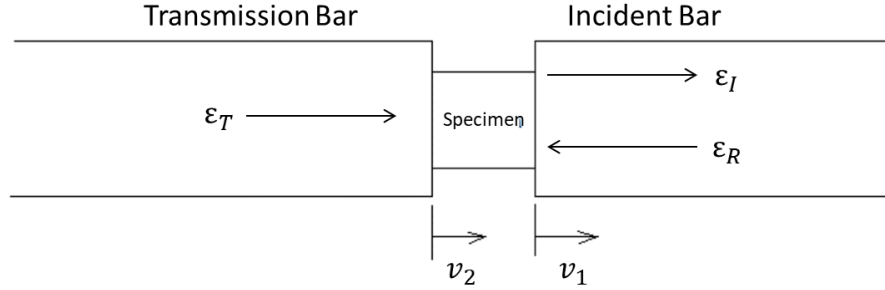
Figure 3.2 Diagram of the testing section of the SHTB

$$v_1 = C_B(\varepsilon_I - \varepsilon_R) \tag{3.1}$$

$$v_2 = C_B\varepsilon_T \tag{3.2}$$

The subscripts, I, R, and T, represent the incident, reflected, and transmitted pulses, respectively. The average engineering strain rate and strain in the specimen are

$$\dot{\varepsilon} = \frac{v_1 - v_2}{L_S} \tag{3.3}$$

$$\varepsilon = \int_0^t \dot{\varepsilon} \, dt = \frac{C_B}{L_S} \int_0^t (\varepsilon_I - \varepsilon_R - \varepsilon_T) \, dt \tag{3.4}$$

where L_S is the length of the specimen at the start of the experiment. The stress at both ends of the specimen are calculated with the following equations,

$$\sigma_1 = \frac{A_B}{A_S} E_B(\varepsilon_I + \varepsilon_R) \tag{3.5}$$

$$\sigma_2 = \frac{A_B}{A_S} E_B\varepsilon_T \tag{3.6}$$

where A_B and A_S are the cross-sectional areas of the bars and the specimen,; and E_B is Young's modulus of the bar material. Based on the equilibrium assumption that the due to the small size of the sample the stress is equally distributed in the sample (Eq. 3.7).

$$\sigma_1 = \sigma_2 \tag{3.7}$$

Therefore, from Eq. 3.5-3.7, as long as the stress equilibrium is satisfied, the incident, reflected and transmitted strains satisfy the relationship described in Eq. 3.8. By obtaining the stress and strain of the specimen, the properties of the tested specimen can be successfully characterized.

$$\varepsilon_I + \varepsilon_R = \varepsilon_T \tag{3.8}$$

Equation 3.1-3.8 demonstrate the fundamental theory of the SHTB in the high-strain-rate mechanical measurement. It can be observed that the results will be affected by the material and dimensions of both the bars and the specimen. Therefore, the parameters and method are usually modified under certain circumstances to facilitate and the accuracy of the measurement.

The aim of this study is to apply this technology to measure the mechanical properties of human ISJ at different levels of strain rate and analyze its viscoelastic behavior under impact loading by a 3-D FE model.

3.2 Methods

3.2.1 Sample preparation

Eleven (7 left and 4 right) fresh human TBs with an average donor's age of 72 years were involved in this study. The TBs were provided by a certified human tissue supply source for medical and military research named Life Legacy Foundation. The sample preparation is the same as it is described in the chapter 2 section 2.2.1. It has also

been reported by Jiang and Gan, (2018). To be brief, each TB were processed with saline and povidone solution to maintain its physiological condition after it arrived in our lab and examined to ensure the non-existence of middle ear abnormities. The middle ear cavity was opened to expose the middle ear ossicular chain. The ISJ was harvested by separating the incus from the IMJ and the stapes from SAL. Each ISJ sample was extracted out from the ossicular chain with intact stapes and incus.

The setup of SHTB experiment required the ISJ to be aligned along the central line of the bars. Considering the complex geometry of the ISJ sample, the end of the incident bar was adjusted to a cylindrical adapter with the upper half removed to form a 90-degree angle to fit in the ISJ specimen (Fig. 3.3a). A specially made clamp fixture with 90-degree angle clamped the long process of the incus to the perpendicular surface of the end of the incident bar through a pair of mini bolts. A window is opened at the center of the clamp fixture to allow the stapes to extrude out (Fig 3.3b). The end of the transmission bar was cut into the upper and lower halves. A flat-headed adapter was clamped between the two parts and worked as an extension of the transmission bar out from its flat surface at the end. After the ISJ is aligned under the microscope (Zeiss, OPMI 1-FC) in both the horizontal and vertical directions, super glue was applied to connect the stapes footplate to the adapter attached to the transmission bar and fix the long process of incus to the incident bar as shown in the Fig. 3.3. During the mounting process, the moisture of the ISJ specimen was maintained by adding a drop of saline solution to the ISJ every 5 minutes.

The dimension of the ISJ specimen was measured after the completion in the same manner as it was described in the section 2.2.2. The lengths of the long axis *a*, short axis

b, and cross-sectional area A of 11 ISJ specimens are listed in Table 3.1. Other geometry parameters of the ISJ were assumed to be the same as the data used in Zhang and Gan (2011), which is the value used in chapter 2.
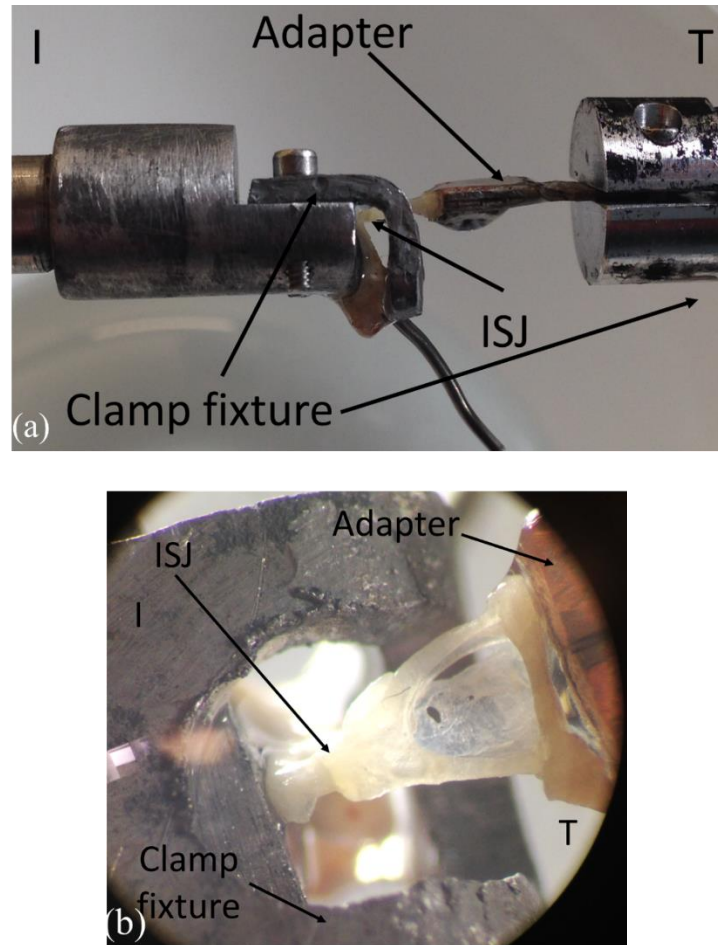
Figure 3.3 (a) Lateral and (b) top view of the ISJ sample mounted between the clamp fixtures. I, incident bar; T transmission bar.

Table 3.1 Dimensions of the ISJ specimens.

N=11	1	2	3	4	5	6	7	8	9	10	11	Mean	SD
a(mm)	0.97	1.00	0.79	0.86	0.94	0.91	0.81	1.04	0.93	0.91	1.01	0.92	0.08
b(mm)	0.66	0.72	0.55	0.67	0.68	0.66	0.69	0.72	0.68	0.75	0.78	0.69	0.06
A (mm^2)	0.50	0.57	0.34	0.45	0.50	0.47	0.44	0.59	0.50	0.54	0.62	0.50	0.08

3.2.2 SHTB Experimental Setup

A high-sensitivity miniature SHTB established by Luo et al., (2016) was used in this study. The experimental setup for the ISJ is similar to the TM study (Luo et al., 2009, 2016) except the sample adapters were modified for mounting ISJ specimen. The schematic diagram of the setup is presented in Fig. 3.1 and a photo of the equipment are shown in Fig 3.4. The incident bar was a 3.66 m long aluminum 7075-T6 bar with 6.4 mm diameter. The transmission bar, however, was hollow which is specially designed for small-size and low stiffness biological tissues. The transmission bar is made of aluminum 6061-T6 with 5 mm inner diameter and 6.4 mm outer diameter. The clamp fixtures were made by 7075-T6 aluminum. An aluminum tube striker bar was launched to make an impact with a flange which was threaded to the incident bar end to load the specimen.
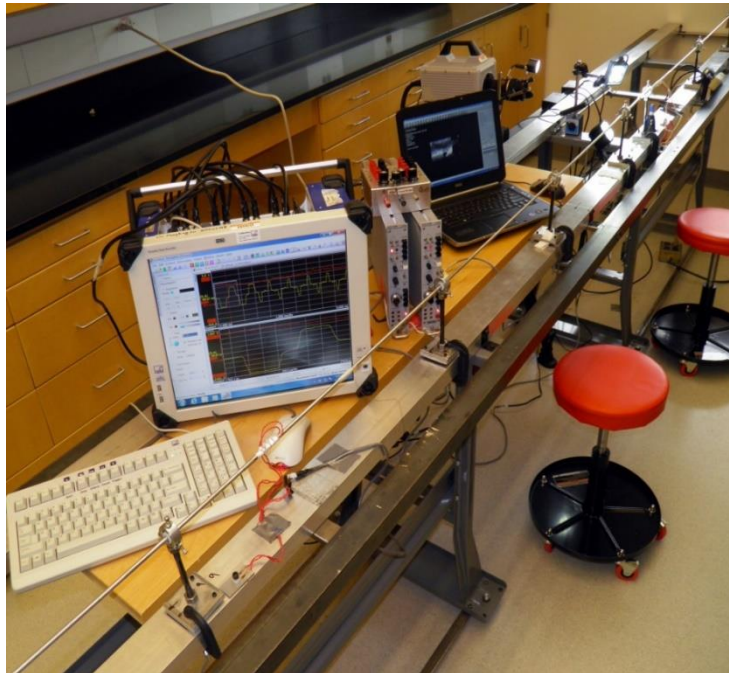
Figure 3.4 SHTB bars and electronic equipmen**t**

The impulse load was created by a pendulum hit the striker tube and the intensity was controlled by the height of the pendulum. Two semiconductor strain gages with a gage factor of 176 were attached to the opposite surfaces of the transmission bar. The distance

between the clamp fixture and the strain gages on the transmission bar was 17.8 cm. The schematic circuit of the Wheatstone bridge is shown in Fig. 3.5, which is a typical half bridge configuration. The R1 and R4 were the strain gages placed on the bars while the R3 and R2 were dummy resistors match with the R1 and R4 values. Since the strain gage was placed on the SHTB on the opposite sides, bending deformation of the bar would result in the change of the resistor values of the R1 and R2 in the opposite way. However, the circuit showing in Fig. 3.5 was able to eliminate the inversely change in the R1 and R4 values in the output signal and only amplifies the tension or compression signals (Chen and Song, 2010). The signal amplifiers were Vishay 2310B signal-conditioning amplifier (up to magnification of 11,000, 180 kHz response frequency). The oscilloscope used for data acquisition was HBM Genesis 5i digital oscilloscope (25 MHz sampling rate, 15-bit resolution, 1 MHz frequency bandwidth). The strain values were calculated from the final output voltage normalized by the total gain from the strain gage, Wheatstone bridge, signal conditioner and the oscilloscope.
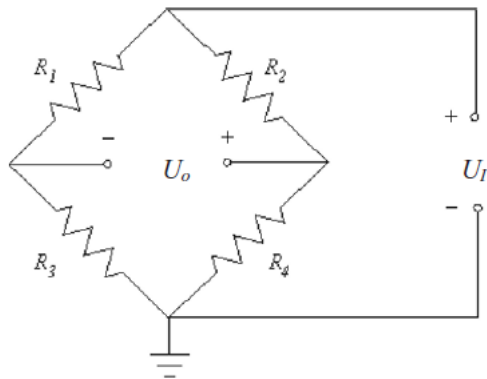
Figure 3.5 The Wheatstone bridge (half bridge)

Based on the theory explained by Eq. 3.1-3.8 and the adjustment made for the miniature SHTB in this setup, the formula for the stress and strain rate of the ISJ sample is given as (Luo et al., 2006, 2009, 2016)

$$\sigma_s(t) = \frac{A_t}{A_s} E_t \varepsilon_t(t) \tag{3.9}$$

$$\dot{\varepsilon}(t) = \frac{1}{L_s}[(c_i - c_t\beta)\varepsilon_i(t) - (c_i + c_t\beta)\varepsilon_r(t)] \tag{3.10}$$

$$\beta = E_i A_i/(E_t A_t) \tag{3.11}$$

where *E, c, ε, r, A,* and L are Young's modulus, bar wave speed, strain, stress, cross-sectional area, and length, respectively; the subscripts *i, t, r* represent the incident, transmitted, reflected signals, respectively. The subscript s indicates specimen. The strain history is obtained through the integration of strain rate with respect to time. The preconditioning process of the ISJ sample was conducted by gently pushed the transmission bar a few time to slightly stretch the specimen. The deformation of ISJ is during the preconditioning process is controlled under a microscope. Tensile tests ISJ specimens were conducted within two ranges of strain rates, namely, 300–700/s and 1200–1700/s.

3.3 Results

3.3.1 Typical SHTB signal

A typical result obtained from the experiment is presented in Fig. 3.6. The red curve is the voltage signal measured from the strain gage on the incident curve while the blue curve is the data measured from the transmission wave. The positive values in voltage indicate the deformation is tension and the negative values indicate compression. The ε is the magnitude of the strain which is amplified and transformed into voltage values recorded by the oscilloscope and the subscripts *i, t, r* represent the incident,

transmitted, reflected signals, respectively. Fig 3.6 demonstrates that the pulse of stress wave reaches the strain gage on the incident bar, and is recorded as ε_i. Part of the signal passed through the specimen and detected by the strain gages on the transmission bar to form ε_t. The rest of the energy reached the end of the incident bar and returned back to the strain gages to form a negative wave of ε_r, which represented a compressive deformation in the incident bar. The square waves shown in the Fig3.6 proved that the high-strain-rate deformation was built up in a time length short enough to be considered as an impulse load and no significant wave dissipation was observed. The existence of ε_t suggested that the ISJ specimen successfully transmitted the stress wave into the transmission bar before broken.
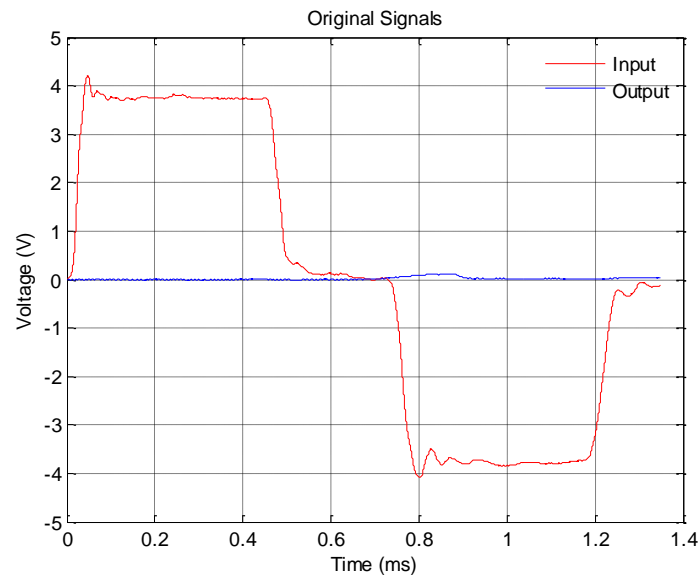
Figure 3.6 Typical signal captured by the oscilloscope

3.3.2 Stress-Strain Curves of ISJ specimens

Eleven ISJs were divided into two different group. Results of six ISJs from the high-strain-rate group with an average strain rate of 1400/s is plotted in Fig. 3.7 in 6

different colors. Noted the fact that all specimens experienced deformation large enough to break the joint at the end of the test, the rage of a strain selected to be shown in the figure for each specimen was 0.02 above the level at which it reached its maximum stress. In Fig. 3.7, the maximum strain levels of six ISJs ranged from 0.06 to 0.12 while the maximum stress varied from 2.2 to 4.8 MPa. All of the curves showed linearity at strain levels lower than 0.03 with good consistency. Four samples showed good linearity at strain levels below 0.05 but the green and yellow curves showed much lower stress with the increase of the strain. The average stress-strain curves of all 6 samples were shown as the black broken lines with SD bars. It can be observed that the curve is almost linear at low strain levels and the SD increased with the strain level increased. The maximum average stress reached 3.60 MPa with an SD value of 0.942 at the strain of 0.07. A linear regression was made and was plotted in black solid line in Fig. 3.7. A slope, which is the average elastic modulus of 54.6 MPa was found with an r^2 equaled to 0.978 and the 95% confidence interval was 46.28 to 62.93 MPa. This results indicated that ISJ exhibited linear stress-strain relationship at strain rate level of 1400/s.

Stress-strain curves obtained from five ISJs under low-strain-rate deformation is presented in Fig. 3.8. The average strain rate of five specimens was 350/s. Figure 3.8 shares the similar organization with Fig. 3.7. At strain levels below 0.2, the stress of two samples reached their maximum value at 0.7 MPa and decreased with the strain after the peak value. The maximum strain for these two samples was approximately 0.07. However, the stress of the other three ISJs continuously increased with the strain which indicated that the joint is not damaged at strain levels below 0.2. The linearity of
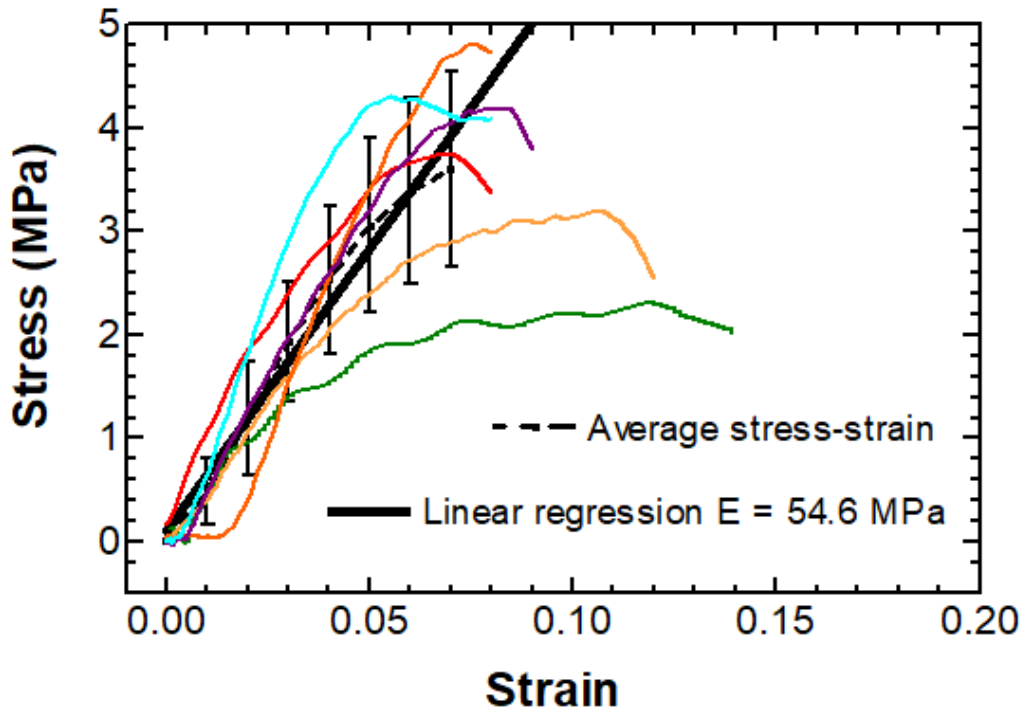
Figure 3.7 Stress-strain curves with mean and SD from 6 ISJ samples measured under average strain rates of 1400/s
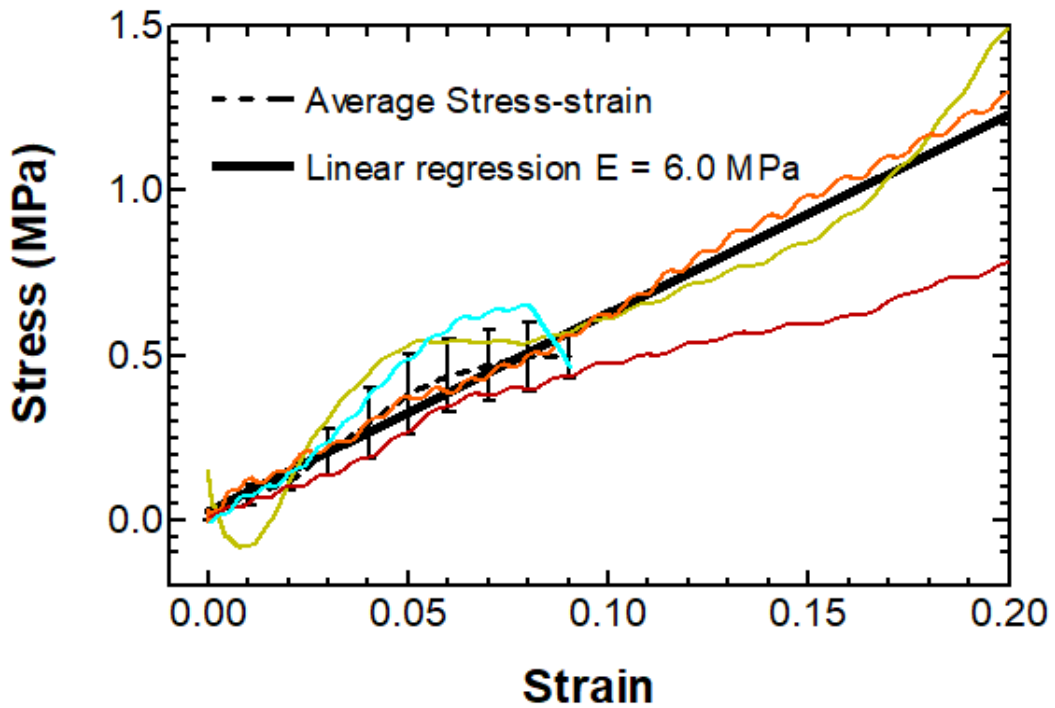
Figure 3.8 Stress-strain curves with mean and SD from 5 ISJ samples measured under average strain rate of 350/s

the curves can be observed over the entire strain range. The average stress-strain curves were plotted in black broken line with bars showing the SD at each strain level. The maximum stress was 0.497 MPa at the strain of 0.09 with an SD of 0.065 MPa. The linear regression result was shown as the black solid line with a slope of 6.0 MPa which represented the average Young's modulus of the ISJ at the strain rate of 350/s. The r^2 for the linear regression was 0.96 and the 95% confidence interval was 5.0 to 7.1. The linear stress-strain relationship of the ISJ at the strain rate of 350/s was observed at strain levels as high as 0.2.

3.4 Discussion

3.4.1 Finite elemental analysis

The stress-strain relationship of ISJ at the strain rates of 1400/s and 350/s was successfully measured using SHTB, however, the strain-rate-dependent structure-function relationship of the ISJ was not thoroughly investigated. An FE model with the same structure in chapter 2 (Fig 2.3). The geometry of the FE model was adjusted based on a and *b* values listed in Table 3.1 (a = 0.92 mm and b = 0.69 mm). The values of t, L, D, h, remained unchanged, as well as the element types. The material properties of the components inside the ISJ are listed in Table 3.2. The data followed values used by Zhang and Gan, (2011) and the study conducted in chapter 2 except the material properties of the joint capsule. Noted that it was fundamental to the stiffness of the joint, the linear viscoelastic properties of the joint capsule were described by a one-term standard linear solid model as shown below(Fung, 2013; Zhang and Gan, 2010).

$$E(t) = E_0(1 - p_1(1 - e^{-\tau/t1})) \tag{3.12}$$

The boundary condition on the bottom surface of the incus was defined as fixed with no displacement and a displacement in the direction of stretching the ISJ with a maximum value of 0.056 mm was applied on the top of the stapes. The 0.056 was calculated from the length of the capsule of 0.28 mm which resulted in a maximum strain of 0.2. A series transient analyses were conducted to simulate the deformation of the ISJ at the strain rates of 400, 800, 1200, and 1600/s. The stress was calculated by the force obtained on the incus surface divided by the mean cross-sectional area of the ISJ listed in Table 3.1 ($A=0.5$ mm^2). Finally, the viscoelastic parameters of the joint capsule were determined by a matching the simulation results to the experimental data and listed in Table 3.2. Results showed that the values of E_0, p_1, and τ_1 were 70 MPa, 0.94 and 20 μs, respectively.

Table 3.2 Components and material parameters of the model

Components	Young's modulus (Pa)	Poisson's ratio	Viscosity (Ns/m^2)
Incus	1.41×10^{10}	0.3	
Stapes head	1.41×10^{10}	0.3	
Cartilage	1.00×10^7	0.3	
Capsule	Relaxation modulus (one-term Prony series) $E(t) = 70(1 - 0.94(1 - e^{-t/0.00002}))$ MPa	0.3	
Synovial fluid	2.20×10^9 (Bulk modulus)		0.4

.
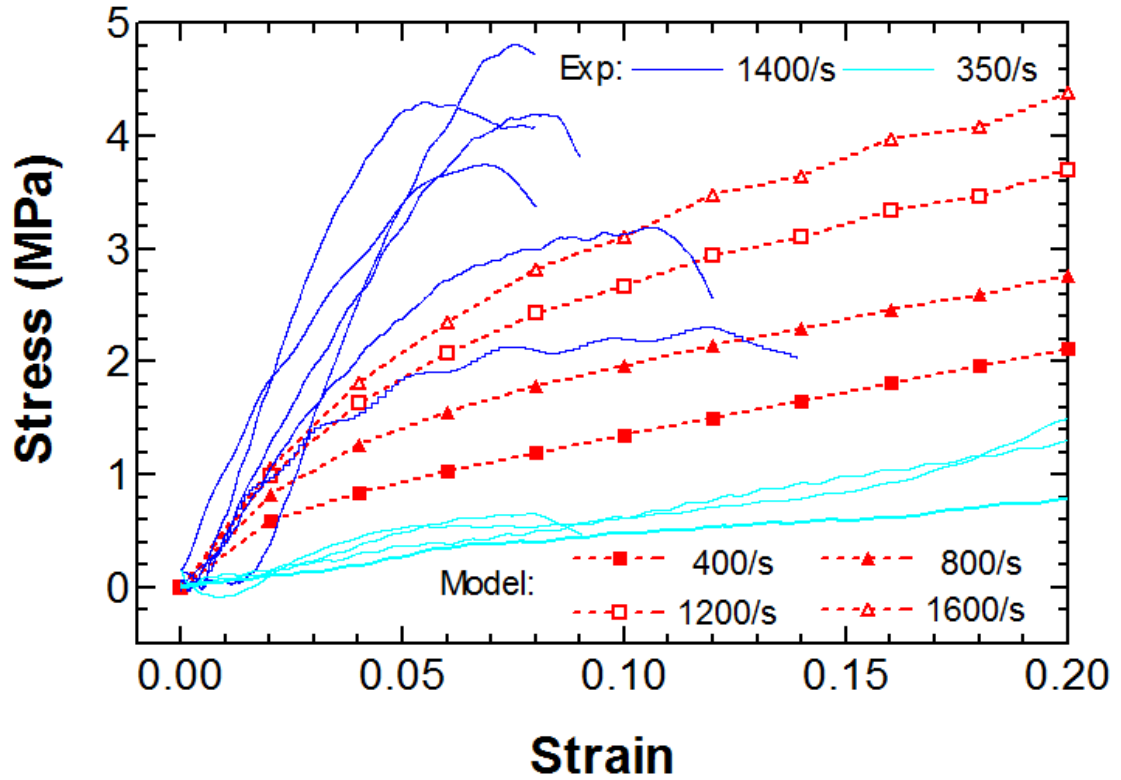
Figure 3.9 Comparison between the stress-strain curves obtained from a model derived results (red dash curves) and experimental data at various strain rates.

The stress-strain curves at different strain rates obtained from the FE simulation are presented in Fig. 3.9 together with the experimental data. The blue curves represent results measured from the experiments while the red dotted curves represent results obtained from the FE simulation at 4 different strain rate levels. Overall, the experimental data and the model prediction have similar shapes of the curves but show more difference in stress values with the increase in the strain. The 400/s curve predicted by the model is paralleled to the 350/s experimental curves at strain levels higher than 0.04. However, the stress level predicted by the model is higher than the experimental data. The model predicted curves at 400/s, 800/s, 1200/s, and 1600/s show similar curve shapes with slope decrease with the strain and stress levels increase with the strain rate. The model predicted curve at 1600/s partially overlaps with one of the low-stiffness experimental results in the

1400/s group. The current FE model simulation is generally consistent with the experimental data but is unable to perfectly repeat the experimental results.

3.4.2 Comparison with published data

The mechanical properties of human ISJ have been measured under quasi-static and dynamic conditions(Jiang and Gan, 2018; Zhang and Gan, 2010). Zhang and Gan (2010) reported that the mean stress measured from the quasi-static test at a strain of 0.2 was approximately 0.15 MPa, which was lower than the result reported in this study. Considering the viscoelastic behavior of the ISJ, it was reasonable that the joint exhibited higher stiffness in tensile tests under high-strain rate than quasi-static conditions. In chapter 2, we reported that the ISJs were measured by DMA with a mean storage modulus of 1.14 MPa at 1 Hz that increased to 3.01 MPa at 8 kHz, and a loss modulus that increased from 0.07 to 0.47 MPa, which indicated the stiffness of the joint was lower than the results shown in the Fig. 3.7 and 3.8 (Jiang and Gan, 2018). Noted that the amplitude of the displacement used in chapter 2 was 0.1 mm, the frequency range of 1 Hz to 8 kHz would indicate during the vibration process, the strain rate experienced by the ISJ. However, the methods used in two studies were very different and both compression and stretching deformation were involved in the experiment in chapter 2. Even though the mechanical properties measured from this study showed some difference with the previously published data, the viscoelastic behavior of the joint, which showed the increase of the stiffness with the frequency or shear rate, were successfully observed in the previous and current studies.

The viscoelastic properties of the ISJ capsule obtained through the FE simulation based on experimental data have been reported by Gan and Wang (2015) and Jiang and

Gan (2018). The standard linear solid model was used to describe the behavior of the ISJ capsule. Gan and Wang (2015) reported that the $E_0 = 0.4$ MPa, $E_1 = 20$ MPa and $\tau_1 = 20$ μs. Jiang and Gan (2018) reported the material of the ISJ capsule as the 7-term standard linear solid model as $E_0 = 2.9$ MPa, $E_1 = 1.25$ MPa, $\tau_1 = 2.6$ ms, $E_2 = 1.9$ MPa, $\tau_2 = 0.14$ ms, $E_3 = 0.12$ MPa and $\tau_3 = 0.13$ ms. From Equation 3.12, the material properties of ISJ capsule reported in this study were $E_0 = 4.2$ MPa, $E_1 = 65.8$ MPa, $\tau_1 = 20$ μs. It can be observed that comparing to the results measured from DMA (Jiang and Gan, 2018), the results obtained in this study was closer to the value used by Gan and Wang, (2015), which was the value derived from FE models of the human ear and used for simulating the function of ISJ in the sound transmission of the middle ear. Special attention was paid to the low E_0, high E_1, τ_1 at the level of microsecond which indicated the strong dependence of the behavior of the ISJ on the strain rate or frequency. Therefore, the results obtained in the current study were able to characterize the function of ISJ under physiological conditions as it was proved by the FE simulation.

3.4.3 Contribution and limitation of this study

In this study, the stress-strain relationship of ISJ under high strain rate was measured for the first time by using a miniature SHTB. The data provided in this study revealed the transient response of the human ISJ under impulse load, which was critical for characterizing the structure-function relationship of the human ISJ under blast exposure and the blast pressure propagation through the ossicular chain. It also provided important data for the analysis and prevention of the blast-induced injuries in the middle ear ossicular chain. The FE model of ISJ constructed in this study simulated the behavior

of joint under high-strain-rate deformation, which could work as a part of the FE model of the whole ear for blast-related hearing damage simulations.

However, there are also limitations of this study. Firstly, the complex structure of the stapes, incus and the clamp fixture (Fig. 3.3) reduced the quality of the transmission signal and the accuracy of the results. The SHTB is built based on one-dimensional stress wave propagation which requires the specimen has a structure as simple as possible. In previous experiments, the testing material was usually cut into a cylindrical shape which shared the same diameter with the incident and transmission bars (Chen and Song, 2010). The cross-sectional area of the specimen is much smaller than the bars. These problems may induce inevitable dissipation of the stress waves during the measurement. The SHTB measurement on soft tissues also requires the elastic modulus of the bar significantly higher than the tested material (Luo et al., 2009). In this study, the glue and bones involved in the specimen which had relatively lower elastic modulus than the aluminum bars might result in inaccuracy of the results. The second possible problem is the alignment of the specimen. Unlike the experimental setup in chapter 2, it was difficult to perfectly align the ISJ along the direction of the bars. The direction of the tension applied on the ISJ was possibly not perpendicular to the articular surface of the stapes and incus. An FE analysis evaluating the effect of the tilted angle of the tension applied on the ISJ would be necessary. The third problem is that only the tensile tests of the ISJ were involved in this test while the behavior of the ISJ under high-strain-rate compression remained unclear. However, normal ISJ will experience both tension and compression when the blast overpressure propagates through the structure. For future studies, a miniature split Hopkinson pressure bar will be built for the compression tests.

3.5 Conclusion

The mechanical properties of 11 human ISJ under mean strain rates of 350/s and 1400/s were successfully measured using miniature SHTB. The average Young's modulus of the ISJ changed from 54.6 MPa at 1400/s to 6.0 MPa at 350/s. The viscoelastic behavior of the ISJ was observed and an FE model of ISJ was built to derive the linear viscoelastic properties of the joint capsule. The results were generally consistent with the published experimentally-measured and model-predicted data. The experimentally-measured and model-derived data are important for understanding the structure-function relationship of the ISJ under impulse load and the transfer function of the middle ear under the blast overpressure.

Chapter 4   Experimental Measurement and Finite Elemental Simulation on Surface Motion of Human Tympanic Membrane after Blast Exposure

(Under review)

4.1 Introduction

The full-field surface motion of the TM is a sensitive indicator to evaluate the sound transmission function of the ear (Cheng et al., 2010; de La Rochefoucauld and Olson, 2010; Rosowski et al., 2011, 2009; Wang et al., 2016; Zhang et al., 2014). Distinct TM vibration modes were observed in TMs whose surface geometry or mechanical properties are different due to disease or species (Cheng et al., 2010; de La Rochefoucauld and Olson, 2010; Rosowski et al., 2011, 2009; Wang et al., 2016; Zhang et al., 2014). The scanning laser Doppler vibrometer (SLDV) has been applied to measure comprehensive data of TM surface motion in human cadaveric and experimental animal samples under both normal and diseased circumstances over a wide frequency range, but has not yet been applied to detect the blast-induced damage in the membrane (de La Rochefoucauld and Olson, 2010; Wang et al., 2016; Zhang et al., 2014). Therefore, the SLDV is used in this study to capture the change of the TM vibration mode before and after the blast to improve our understanding of the blast-induced microstructural damage.

The effect of the TM mechanical properties on the middle ear sound transmission has been proved to be critical in research on the finite element (FE) models of the middle ear. With the development of the FE models of the ear, the material properties of TM have been changed from isotropic to direction-dependent (orthotropic) by taking the fibrous microstructure into consideration (Gan and Wang, 2007; Tuck-Lee et al., 2008;

Volandri et al., 2011). However, a multilayer fibrous structure has not been constructed in existing FE models of TM. Therefore, there is a lack of an appropriate tool to analyze the effect of the damage to the fibers and mechanical property change observed in the experiments on the surface motion of the TM (Engles et al., 2017; Luo et al., 2016). The existing FE isotropic and orthotropic models of TM are difficult to simulate these types of blast-induced damage on fibers directly. A new TM FE model with detailed microstructure including radial and circumferential fibers embedded into a multilayer matrix is necessary to investigate the detailed mechanism of how the blast-induced microstructural damage in TM changes the surface of TM and provides a novel approach for future analysis on the stress-distribution and rupturing process of TM under blast overpressure.

In this paper, we measure the TM vibration mode over a frequency range of 1–8 kHz before and after the blast exposure using the SLDV in cadaveric human temporal bones. To investigate the mechanism of how blast-induced damage affects the surface mobility of the TM, a FE model of the human TM composed of multilayer matrix embedded with radial and circumferential fibers was established based on the SEM observation and directional-dependent mechanical properties of the TM (Engles et al., 2017; Gan and Wang, 2007; Luo et al., 2016). The microstructural damage is simulated by altering the mechanical properties and structure of the fiber network. The experimental data and model simulation show good consistency in normal and damaged cases which suggests the FE model is capable to investigate the mechanism of the blast-induced injuries in TM. The data reported by experimental measurement and FE modeling may provide better elucidation of the blast-induced microstructural damage in the TM and

63

provide a novel approach for analyzing the response of middle ear to the blast overpressure.

4.2 Methods

4.2.1 Human temporal preparation

Two pairs of fresh human temporal bones (TBs), obtained from a 67-year-old male and 71-year-old male donors obtained from Life Legacy Foundation were involved in this study. The study protocol was approved by the US Army Medical Research and Material Command (USAMRMC), Office of Research Protections (ORP). All temporal bones were shipped with dry ice and the experiments were conducted within one week after the samples arrived in our laboratory. Each TB was processed with saline solution containing 15% povidone to maintain its physiological condition before the experiment. Otoscopic examination on the TB ensured that the TM appeared normal and no evidence of diseased middle ear.

The TM was fully exposed through a surgery conducted under a microscope (OPMI-1, Zeiss, Thornwood, NY) to allow the laser beam to reach the laser target placed on the umbo. The inferior half of the pinna was separated from the outer bony wall of the TB with a #10 scalpel starting from the inferior edge of the TB. During the process of the separation surgery, the soft tissues layer was gradually lifted up until the cartilage of the ear canal was exposed. The inferior half of the ear canal was cut through and the flipped part of the soft tissue was clamped to the sample holder to fully expose the TM for the surface motion measurement.

4.2.2 Surface motion of normal TM measured with SLDV

Figure 4.1 was a schematic diagram of the experimental setup. The experiment was conducted followed the protocol made by Zhang et al., 2014. To be brief, the TB was firmly fixed on a sample holder on an anti-vibration table. A chirp stimuli at a sound pressure level (SPL) of 80 dB with a frequency range of 0.5 to 8 kHz was produced by a signal generator (Polytec Ethernet Generator, Polytec Inc., Irvine, CA), an amplifier (RCA SA-155, Radio Shack, Fort Worth, TX), and a speaker (CF1, Tucker-Davis Technologies, Alachua, FL). The sound was delivered through a tube with a diameter of 2 mm. The SPL at the TM surface was monitored by a probe microphone (Model ER-7C, Etymotic Research, IL) placed at the tympanic annulus.

The full-field velocity of the TM in response to the sound stimuli was measured by the SLDV (PSV-500, Polytec Inc., Irvine, CA). The scanning head of the SLDV was placed 80 mm in front of the TB and the area of interest was recorded by the camera shown in Fig. 4.2a. Scanning grids of 400-500 measurement points were distributed evenly over the entire surface of the TM (Fig. 4.2b). The laser beam, which was directed by two moving mirrors with orthogonal axes driven by galvanometer actuators and control unit inside the scanning head, moved along the scanning grid to make a repeated measurement at each scanning point. The velocity at each point was obtained by the laser beam, transformed into the displacement and normalized by the simultaneously measured SPL in the software (PSV 9.2, Polytec Inc., Irvine, CA). The full-field surface motion of the TM over the frequency range of 1 to 8 kHz was obtained from the single-point data. During the entire scanning process, the laser beam was approximately in the direction

perpendicular to the surface of the tympanic annulus and the laser beam was focusing on

the surface of the TM.
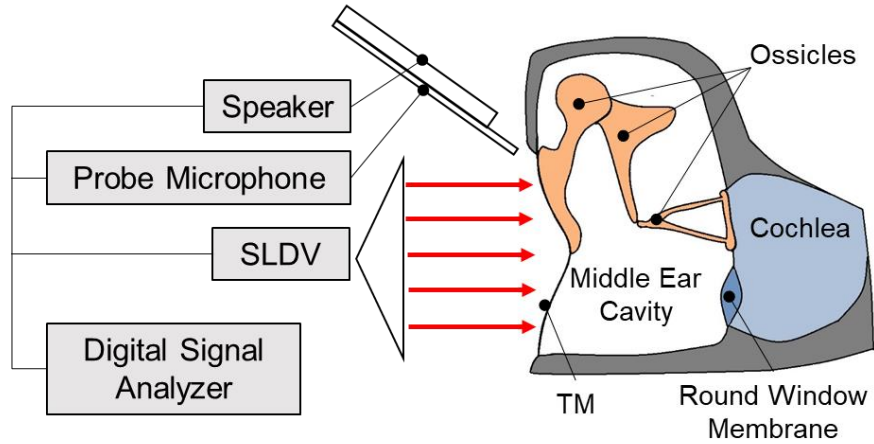
Figure 4.1 Schematic diagram of the experiment setup
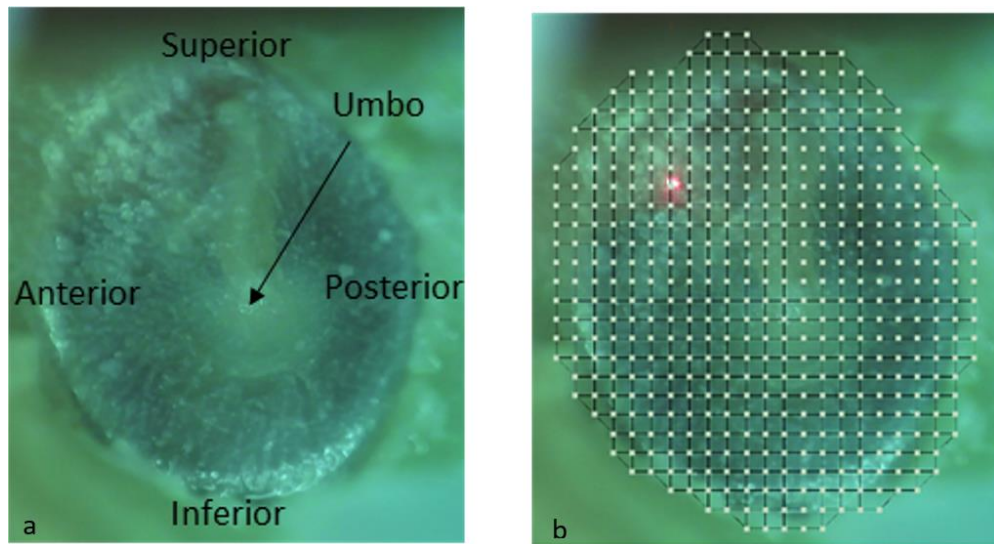
Figure 4.2 (a) One left TM sample image captured by the camera of the SLDV; (b) the scanning grid on the surface of the TM and a laser beam moving from point to point.

4.2.3 Surface motion of post-blast TM measured with SLDV

Upon the completion of the scanning, the specimen was removed from the sample

holder and the exposed bony surface of the TB was covered by the soft tissue. The ear

canal was reconstructed and the pinna was fixed to the TB by suturing. Special attention was paid to the connection between the partially separated ear canal. Then the TB was mounted on a "head block" and placed under the blast apparatus inside an anechoic chamber (Fig. 4.3). The design of the head block, blast apparatus, pressure monitoring system, and chamber followed our previous published blast-related studies (Engles et al., 2017; Luo et al., 2016). The compressed air ruptured polycarbonate films (McMaster-Carr, Atlanta, GA) to produce blast overpressure which struck the front side of the "head block". The input pressure at the entrance of the ear canal was monitored by a pressure sensor (Model 102B16, PCB Piezotronics, NY) mounted on a column approximately 1 cm away from the head block (Fig. 4.3). The data acquisition system consisted of a cDAQ 7194, A/D converter 9215 (National Instruments Inc., Austin, TX), and a software package LabVIEW (National Instruments Inc., Austin, TX). The sampling rate of the acquisition system was 100k/s which was proved to be appropriate in previous studies (Engles et al., 2017; Gan et al., 2016; Luo et al., 2016). The blast waveform had a prominent single peak whose pressure level was recorded to represent the level of the blast. Each TB specimen experienced 4 repeated blasts at a level of 46.2 ± 7.8kPa. Considering that the rupture threshold of human TM was 52.4–62.1 kPa (Engles et al., 2017; Kingery and Pannill, 1964), the aim was to induce discernable microstructural damage in TM without rupturing it. After the completion of the blast exposure, microscopic examination was applied on each TM to ensure the non-existence of the rupture. The full-field motion measurement was conducted again immediately after the completion of the blast exposure following the same protocol reported in the section 4.2.2 and the results were compared with the pre-blast data in each TB.

67
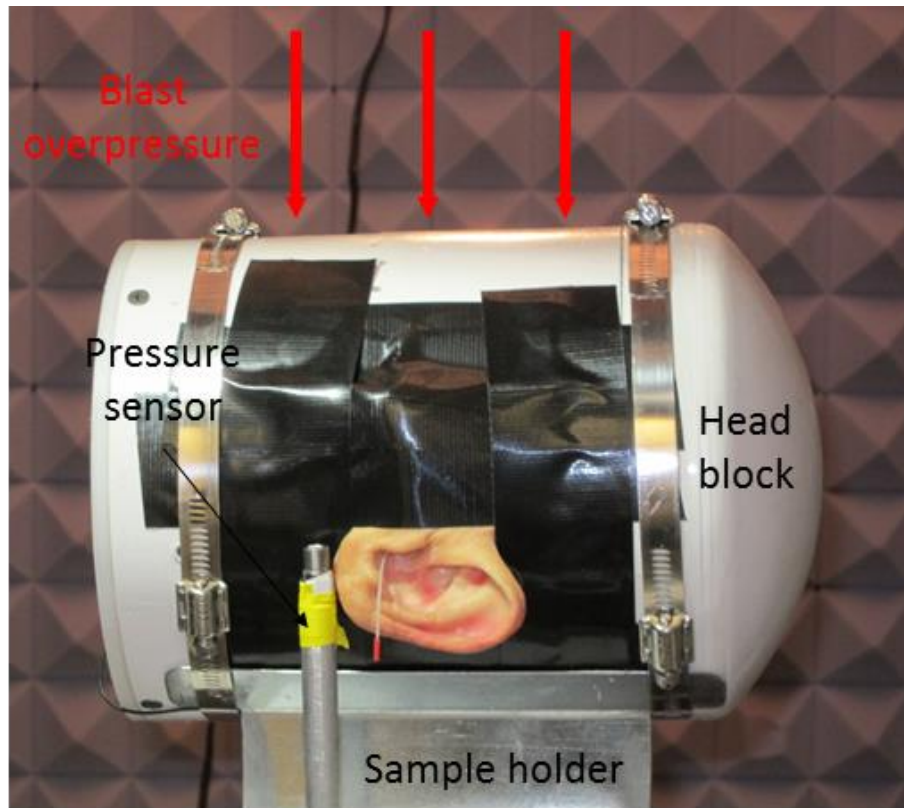
Figure 4.3 Experimental setup for the blast exposure in the blast chamber

4.2.4 Finite element model of human TM

A multilayer FE model of the human TM with fiber network was established based on the ear model built by Zhang and Gan (Gan et al., 2011; Zhang et al., 2014). The ear canal, ossicles, middle ear soft tissues, middle ear cavity and a spiral cochlea were directly obtained from Gan and Zhang's 2011 model as shown in the Fig. 4a. Keeping the TM geometry unchanged, a surface mesh was created on the pars tensa along the radial and circumferential directions and the fibers were distributed along the mesh lines (Fig. 4.4b). The fiber orientations of the model followed the directions of two major types of collagen fibers observed in the TM: the radial fibers originated from the manubrium and ended at the annulus; the circumferential fibers were started and ended

at the manubrium, parallel to the TM annulus and orthogonal to the radial fibers (Fay et al., 2005; Luo et al., 2009; Tuck-Lee et al., 2008; Volandri et al., 2011). The structure of the TM model in the thickness direction is shown in Fig. 4.4c. The TM was separated into five layers: epidermal layer, radial layer, middle layer, circumferential layer and the mucosal layer from the lateral to the medial side. The thicknesses of each layer were: 10 μm, 30 μm, 5 μm, 20 μm and 10 μm, respectively. The total thickness of 75 μm was following the value from Gan and Wang 2007 paper, which was the TM thickness used in a series of FE modeling studies(Gan and Wang, 2007; Gan et al., 2011; Zhang et al., 2014). The thickness of each layer was assumed based on Fay et al. 2005 (Fay et al., 2005). The middle layer was a virtual layer which was designed to allow the relative motion between the circumferential and radial layers. The radial fibers were embedded between the radial and middle layers while the circumferential fibers were between the circumferential and mucosal layers (Gentil et al., 2016). The five layers of the solid element were considered as the matrix of the TM. The pars flaccida was modeled as a non-fiber matrix.

The element types and material properties used in this model were the same as it was reported by Zhang and Gan (2011)(Gan and Wang, 2007; Gan et al., 2011) except the TM. The fibers are modeled using beam elements (beam 188) and the matrix was modeled as solid elements (solid 185). The fibers, matrix, pars flaccida, TM annulus and manubrium were all modeled as linear elastic materials. The elastic moduli of the TM annulus, manubrium and pars flaccida were 0.6 MPa, 4.7 GPa, and 10 MPa which were following the data used in Gan and Wang (2007). The matrix of the pars tensa was considered to share the same elastic moduli with the pars flaccida.

69

Since the density and elastic moduli of the fibers both contributed to the stiffness of the TM, determine these values were the key to the TM model. The fiber density was represented by the volume fraction of the fibers in the TM. As shown in Fig. 4.4c, the radial fiber shares the equal length with the radial side of the matrix element, and the circumferential fiber with the circumferential side, respectively. The cross-sections of the fiber beam elements were simplified as rectangles with thicknesses equaled to the radial or circumferential layers. Therefore, the volume fraction of the fiber in a certain direction at a node on TM was estimated as the width of that fiber divided by the distance between the current and the next adjacent node in the given direction inside the layer of the fiber. With the length is given by the mesh (Fig. 4.4b) and thickness equaled to the respective layer, the volume and thus the volume fraction of the fiber inside the TM was controlled by the width of the beam element. This method of multiscale modeling of fiber-embedded tissues was adopted from Shirazi, R., & Shirazi-Adl, A. (2005) and Freutel, M., et al. (2014). For the volume fraction of the fibers in the TM, Fay et al. suggested the fibrils occupied 30-50% volume of the TM. Therefore, the width of the radial and circumferential fiber elements was 90 μm which resulted in an approximately volume fraction of 20-40% in both radial and circumferential direction at the edge of the TM. Noted that the volume fraction would increase from the edge to the center of the TM so the average volume fraction was higher than the values at the boundary. The fibers in human TM mostly consisted of collagen type I and type II fibrils whose elastic modulus varied around 1 to 10 GPa (Fay et al., 2005; Wenger et al., 2007) and the average elastic modulus in the radial direction was about 1.5 to 2 times of that in the circumferential direction (Gan and Wang, 2007; Luo et al., 2009, 2016). After a cross-calibration process

to match the model-derived TM surface motion to the experimental data, the elastic modulus of radial fiber was determined to be 10 GPa while 6 GPa in the circumferential direction. The mechanical properties used in the TM model is listed in Table 4.1
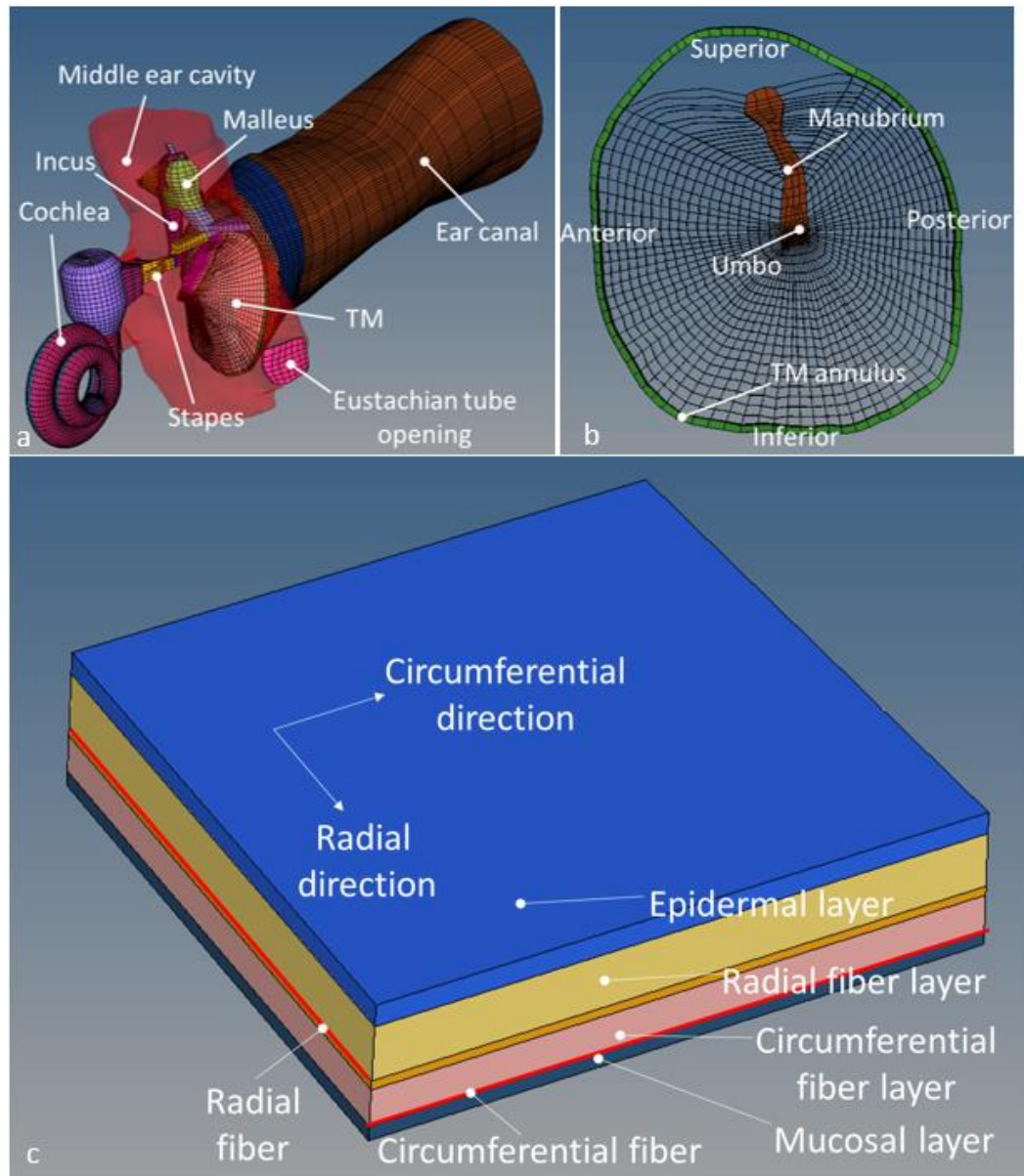
Figure 4.4 The FE model of the human ear: (a) Overview; (b) fibrous structure of the TM;(c) a detailed view showing the structural relationship between the matrix and the fiber elements.

Table 4.1 Mechanical properties of the TM in FE model

	Elastic modulus	Sources
Radial fiber	10 GPa	
Circumferential fiber	6 GPa	
Matrix	10 MPa	*Gan and Wang (2007)*
Parse flaccida	10 MPa	*Gan and Wang (2007)*
TM Annulus	0.6 MPa	*Gan and Wang (2007)*
Manubrium	4.7 GPa	*Gan and Wang (2007)*

4.3 Results

4.3.1 TM full-field surface motion measured by SLDV

Figure 4.5 demonstrates the full-field surface motion of the specimen TM 60 at the frequencies of 1, 2, 3, 4, and 8 kHz before and after the exposure. The color bars on the right column indicate the displacement amplitude normalized by the SPL. The control and blasted TMs share the same color bar at each frequency point. TM 60 is a right TM and the deflection shapes of TM motion are captured from the lateral (ear canal) side which indicates the posterior side of the TB is on the left, and the anterior side is on the right as it was shown at the upper left corner in Fig. 4.5.

At 1 kHz, the contour of the normalized displacement of the untreated TM exhibits two high-displacement areas in the posterior region of the membrane. The maximum displacement emerged in the anterior-posterior region with a value close to 180 nm/Pa. The posterior half of the TM showed higher mobility than the anterior side. After the blast exposure, the location of the maximum displacement stayed at the posterior region of the

72

membrane, but the two peaks merged together to form a major peak at a maximum displacement amplitude around 100 nm/Pa. A low-displacement region located at the manubrium separated the membrane into a posterior region with higher displacement and an anterior region with less mobility in both TMs. The blast exposure did not alter the shape of deflection and location of the peaks at 1 kHz.

At 2 kHz, Fig. 4.5 exhibits high displacement areas in the posterior region of the TM before the blast. Multiple peaks emerged at the levels around 80 nm/Pa and the largest peak was located at the posterior-inferior corner. After the blast exposure, a major peak with a maximum displacement value of 200 nm/Pa appeared in the posterior area of the TM and a fusion of minor peaks into one major peak was similar to what was observed at 1 kHz, but the significant increase of the normalized displacement amplitude in the posterior region was different. The low-mobility area of the manubrium separated the TM into the posterior and anterior sides unsymmetrically, which was shown more clearly in the TM experienced blast exposure. The blast exposure induced changes in the magnitude instead of the location of the displacement peaks.

The displacement contours at 3 kHz of both normal and blasted TMs exhibit no conspicuous difference comparing to the 2 kHz results except the normalized displacement values. The displacement magnitude was uniformly decreased over the entire surface when the frequency increased from 2 to 3 kHz. The maximum normalized displacement in the TM before blast exposure was 70 nm/Pa in normal but increased to 180 nm/Pa in blasted TMs. The high-mobility area still located in the posterior region which was consistent with the 2 kHz results.

At 4 kHz, the shapes of the displacement contours started to change. In pre-blast TM, although the posterior high-displacement area still existed, anther high-displacement area appeared in the anterior region. In the blasted TM, multiple peaks emerged at the posterior, anterior and inferior regions. The posterior and anterior peaks shared a maximum displacement of 60 nm/Pa while the anterior peak was greater in the area. The TM after experiencing blast exposure still exhibited contours with a shape similar to the normal TM, which had high-mobility areas in the posterior region. The changes induced by the blast exposure include the increased maximum displacement and a newly appeared peak in the anterior region.

When the frequency increased to 8 kHz, no prominent major peaks could be observed on the TM before and after blast exposure due to the complexity of contours and the decrease of the displacement amplitude. The whole TM surface was vibrating at a displacement level lower than 20 nm/Pa. The superior region including the manubrium showed the lowest mobility on TM. Multiple minor peaks were observed in the anterior region. Neither displacement magnitude nor the distribution of the contours showed discernable difference before and after the blast exposure.

Results obtained from TM 60 indicate that at the middle frequencies (2-4 kHz), the areas with high mobility concentrated at the posterior region of the membrane and the blast will only increase the displacement at that certain region without changing the shape of the contours. Therefore, the displacement contours of four TMs at 3 kHz are presented in Fig. 4.6 to observe whether this same phenomenon exists in all samples. The left column of pictures in Fig. 4.6 demonstrate the distribution of normalized displacement on TMs before the blast exposure at 3 kHz. Pictures in the right column show results

74

obtained from TM after blast exposure. The TM surface motion of TM 57, 58, 59 and 60 are displayed from the top to the bottom row. A color bar is designed for each specimen to illustrate the magnitude of the displacement normalized by the SPL on the right and the orientation of each specimen is shown on the upper left of each row. A major peak of displacement in the posterior region of the TM was observed in all 4 samples. The maximum displacement on TM was increased from 80 to 140 nm/Pa in TB 57, 58, and 59 and from 70 to 180 nm/Pa in TB 60 after the blast exposure. The shapes of the contours remained unchanged before and after the blast exposure. A single major peak was observed in the central posterior region in TM 57, 58 and 60 but TM 59 showed a more complicated shape of deflection. Multiple minor peaks form a few narrow high-displacement areas paralleled to the manubrium were observed in TM 59, which was probably resulted by its geometry. However, the maximum displacement still located in the posterior region and the blast-induced damage increased the displacement amplitude at the same level comparing to other three specimens.

The displacement contours of all four TMs before and after the blast exposure at 4 kHz are shown in Fig. 4.7, which shares the same organization of Fig. 4.6. Similar to what is presented in Fig. 4.6, the blast exposure increases the displacement in the posterior region of the membrane without changing the distribution of the peaks at 4 kHz. In TM 57, the maximum displacement in the posterior region increased from 40 nm/Pa to 100 nm/Pa after the blast. But in TM 58, the size instead of the value of the displacement peak increased due to the blast. In TM 59, the maximum displacement increased from 50 to 80 nm/Pa while from 30 to 60 nm/Pa in TM 60. Noted that at 4 kHz, high-displacement areas emerged in the anterior region of some of the TMs after the blast exposure. In TM 57, the

long and narrow high-displacement area appeared in the anterior region of TM after the blast exposure. In TM 59 and 60, the displacement magnitude in the anterior-high-displacement area increased after the blast exposure. In TM 58, however, such area existed in the anterior region but slightly decreased in size after experiencing the blast. This phenomenon indicated that the vibration mode of single posterior peak domination started to change at 4 kHz and higher frequencies, but the blast-induced damage was likely to make this change happened at frequencies lower than 4 kHz.
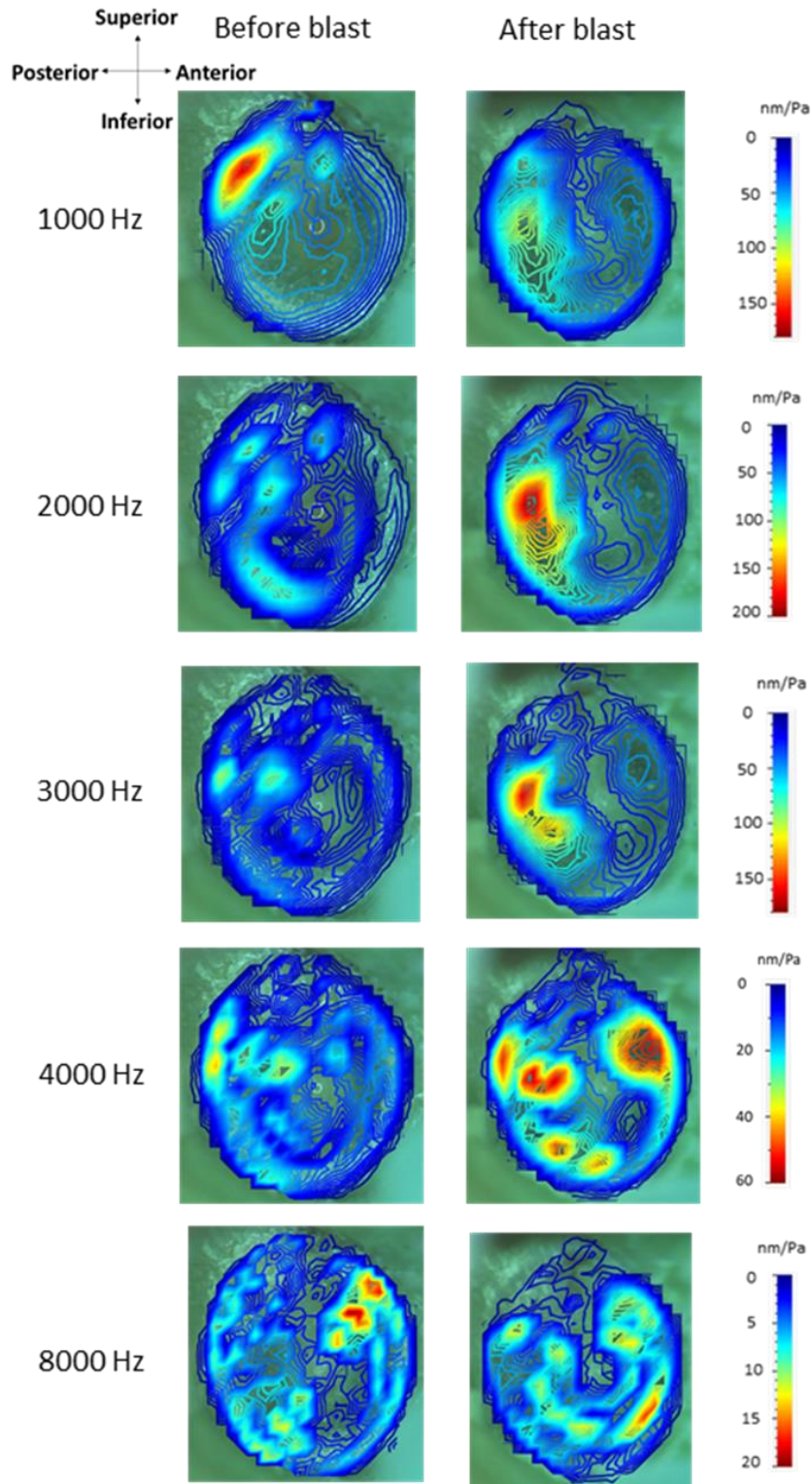
Figure 4.5 The contour plots of normalized TM displacement magnitude measured from sample TB-60 at the frequencies before and after the blast exposure 1, 2, 4, 8 kHz.
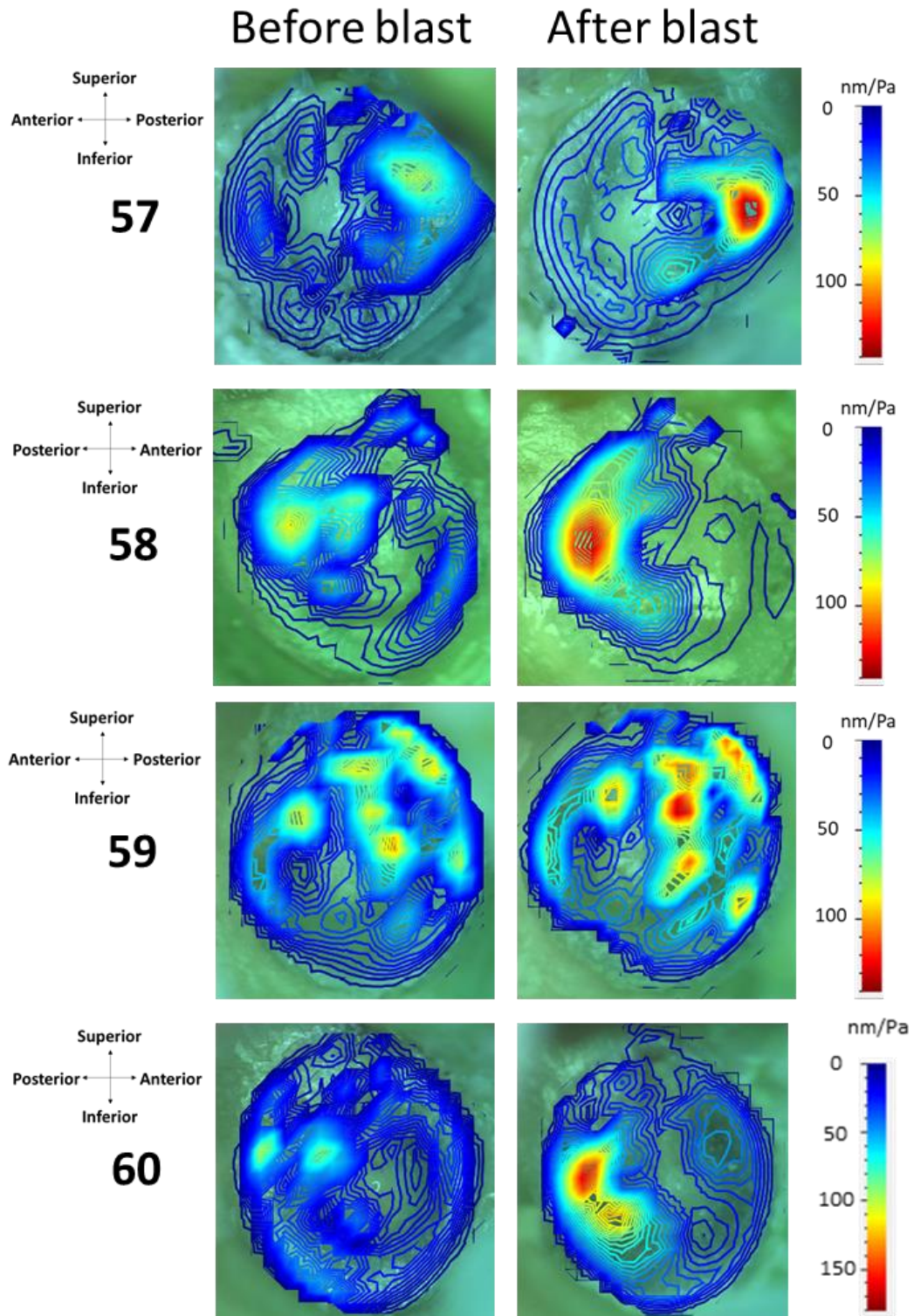
Figure 4.6 The contour plots of normalized TM displacement magnitude measured from four samples at 3 kHz.
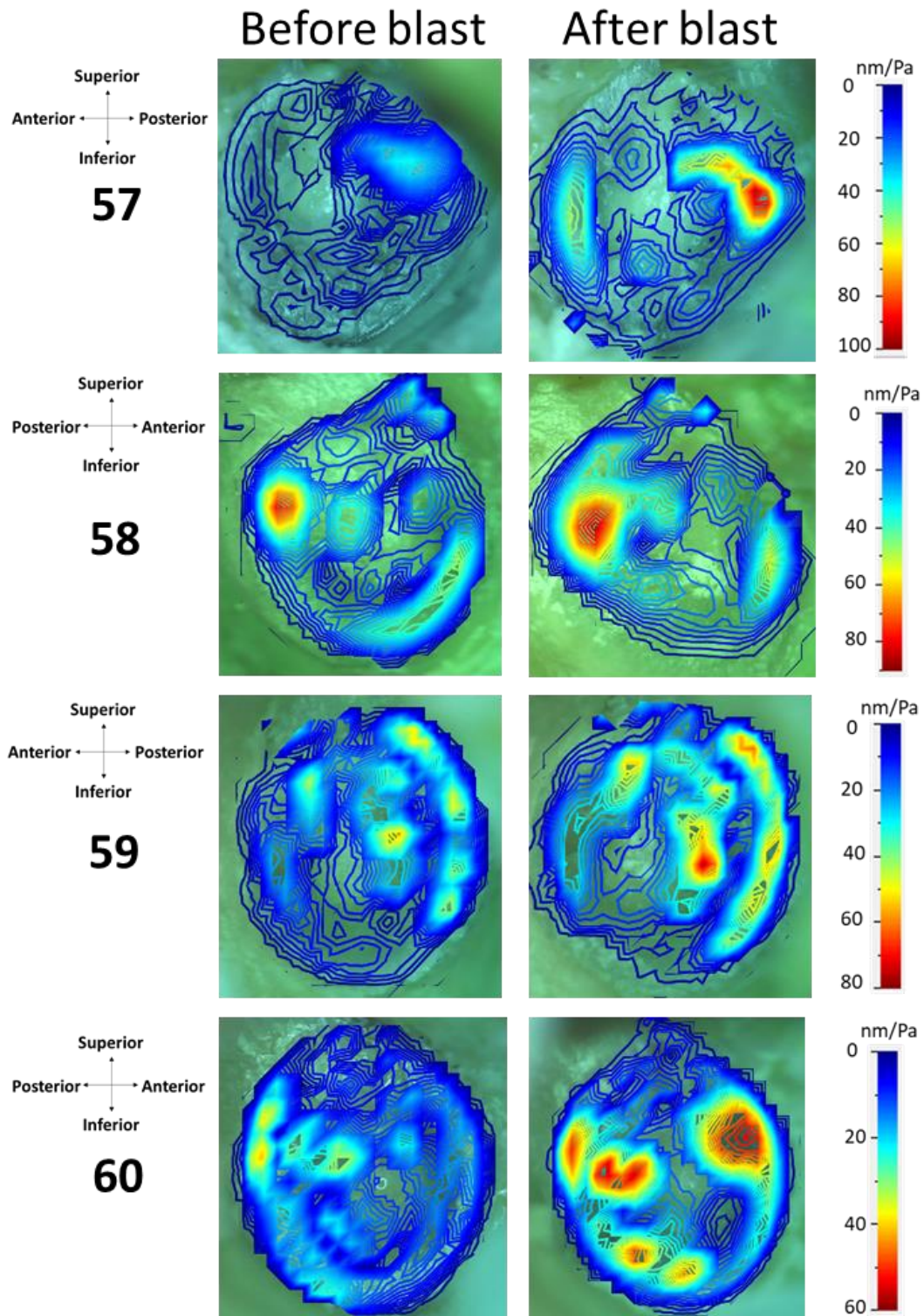
Figure 4.7 The contour plots of normalized TM displacement magnitude measured from four samples at 4 kHz.

4.3.2 TM surface motion simulated by FE model

Experimental results indicated that there was a prominent high displacement area existed in the posterior region of the TM at frequencies lower than 4 kHz (Fig. 4.6&4.7). The increased displacement of this area after the blast exposure was observed in all four samples (Fig. 4.7). The mechanical test had revealed that the exposure to blast overpressure resulted in directional dependent mechanical properties change in human TM (Engles et al., 2017; Luo et al., 2016). To investigate the relationship between the change of the mechanical properties and the surface motion, the blast-induced damage was simulated in three different ways in the FE model. The first method was to reduce the elastic modulus of the fibers since the decrease modulus of the TM mechanical properties was reported by Engles et al. (2017). The elastic moduli of the radial and circumferential fibers were set to be 1 and 0.6 MPa, which simulated the situation that all fibers were severely damaged and having elastic moduli lower than the matrix. The second method was to reduce the volume fraction of the fibers. The width of the fibers was reduced to 9 μm which reduced the volume fraction of the fiber to 1/10 of its original value. The third approach was to remove a part of the fiber network. In the FE model, based on the assumption that the increased displacement after the injury resulted from the blast-induced structural damage, we removed the fiber network at the respective region to simulate the damage as it was shown in Fig. 4.8. The model-predicted TM surface motion was compared with the experimental data over the frequency range from 1 to 8 kHz.

The deflection shapes of the TM at frequencies of 1, 2, 3, 4, and 8 kHz derived from FE model are shown in Fig. 4.9. As it was explained in section 2.4, the pictures were

taken from the lateral side of a left ear, whose orientation was labeled at the top left of Fig. 4.9. Three types of the blast-induced damages: reduced fiber elastic modulus, reduced fiber volume fraction, and partially removed fibers (hole) were simulated in FE models and the results were shown in the Fig. 4.9. The displacement in the direction perpendicular to the surface of TM annulus was normalized by the SPL and plotted on the TM surface in different colors following the scale provided in the rightmost column in Fig. 4.9 at 5 different frequency levels. The FE model-derived TM surface motion was generally consistent with those from the experimental results measured by SLDV (Fig. 4.5-4.7).

For the normal TM, a prominent major peak was observed in the posterior-inferior region at all frequencies, whose dominance decreased with the frequency. A secondary peak emerged in the anterior region at frequencies equal to or higher than 3 kHz and multiple high-displacement areas formed a complicated shape of deflection at 8 Hz. The magnitude of the maximum displacement gradually decreased with the frequency from 118 nm/Pa at 1 kHz to 4.5 nm/Pa at 8 kHz. The normal TM exhibited the lowest surface mobility over the entire frequency among four different TM FE models.

For three different methods simulating the damaged TMs, the major peak in the posterior region was discernable at the frequencies lower than 3 kHz in the elastic modulus group, 4 kHz in the volume fraction group, and 8 kHz in the "hole" group. The location of the major peak was consistent with what was observed in the normal TM and the maximum displacement value was greater in damaged TMs. At 1 kHz, there was only one major displacement peak in all TMs and the TM with reduced elastic
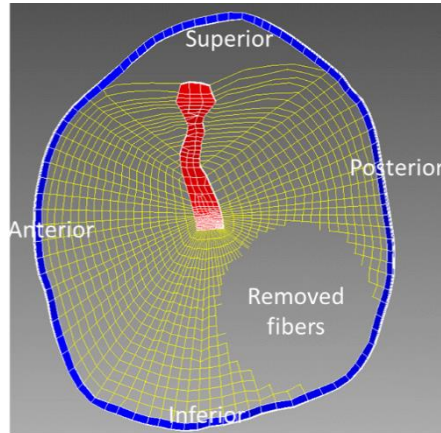
Figure 4.8 Fibrous structure of the TM simulating the regional loss of fiber ("the Hole") viewing from the lateral side.

modulus showed the highest maximum displacement of 632 nm/Pa. At 2 kHz, the second peak in the anterior region emerged in the TM with reduced elastic modulus, but the other two damaged TMs kept the similar deflection shape as the normal TM. The highest displacement at a value of 149.5 nm/Pa emerged in the location where the fiber network was removed in the TM with a hole. At 3 kHz, multiple peaks appeared to form a half-ring-shaped high displacement area in the TM with lower elastic modulus. The low volume fraction and the "hole" TMs showed deflection shape close to the normal TM with increased mobility. The maximum displacement decreased to 49.1 nm/Pa. At 4 and 8 kHz, the trend continued in all four TMs. A ring-shaped high-displacement area emerged on the surface of the TM with reduced elastic modulus, and the displacement values were uniformly distributed on the entire membrane. The behavior of the TM with reduced volume fraction at high frequency was similar to what was observed in the low modulus TM at relatively lower frequencies. The partially damaged TM was unique, whose deflection shape remained unchanged over the entire frequency range. The high-displacement area remained at the same location but the maximum displacement gradually decreased from 400 nm/Pa at 1 kHz to 5.9 nm/Pa at 8 kHz.
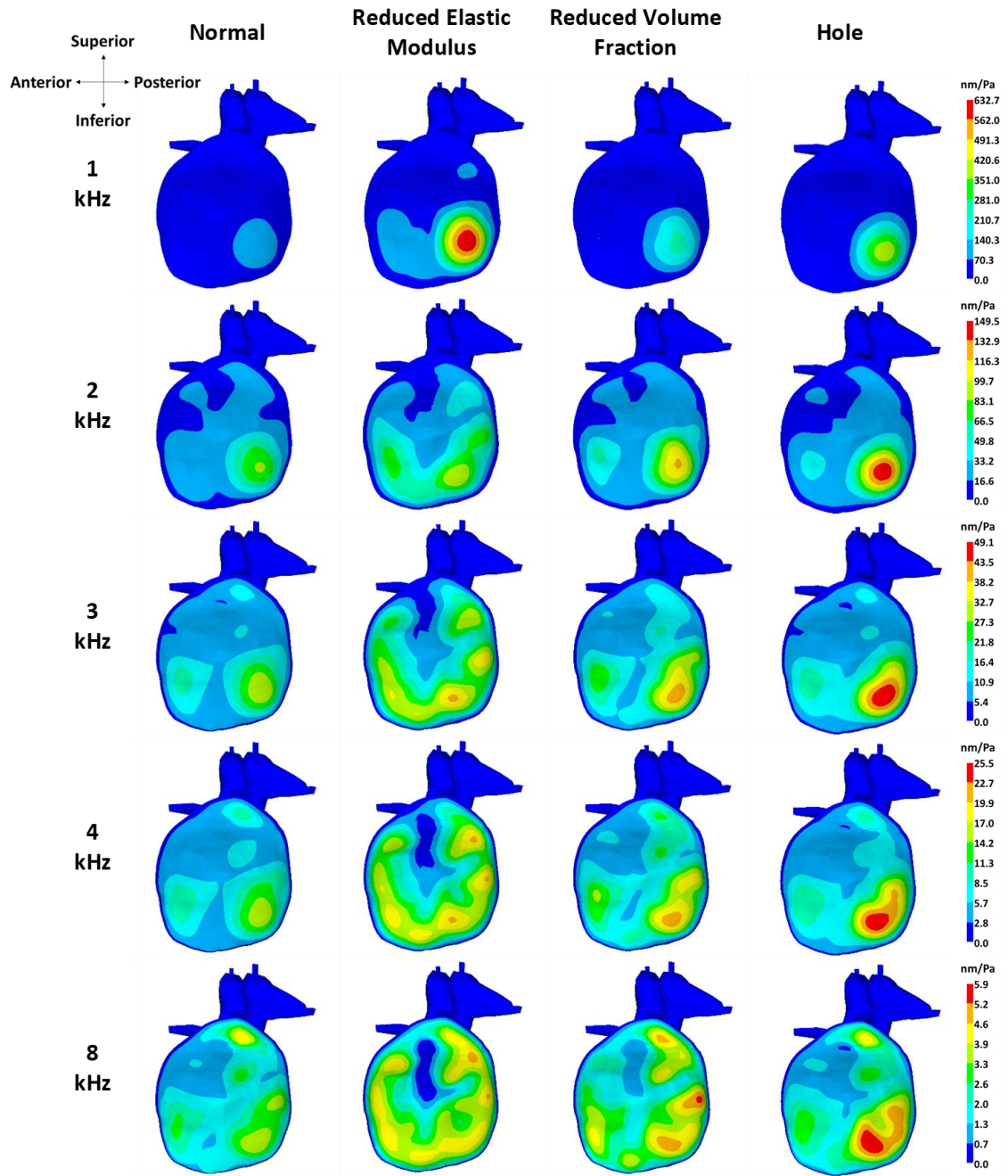
Figure 4.9 FE modeling results of the normalized TM displacement magnitude at 1, 2, 4, 8 kHz. The first column shows normal TMs; the second column shows TMs with reduced elastic modulus; the third column shows the TM with reduced fiber volume fraction; the fourth column shows TMs with partially removed fibers.

4.4 Discussion

4.4.1 Comparison with published data

In this study, the full-field surface motion of human TM under a chirp stimulus of 1 to 8 kHz was measured by SLDV before and after the blast exposure. As an important indicator to evaluate the sound transmission function of the TM and middle ear, the surface motion of human TM in the frequency domain have been measured by SLDV and stroboscopic holography, which were reported in a series of studies (Cheng et al., 2010, 2013; Kozin et al., 2016; Rosowski et al., 2011; Zhang et al., 2014). The values of maximum displacement on the TM surface measured by SLDV reported by Zhang and Gan (2014) were 400, 80, and 16 nm/Pa at 1, 4, and 8 kHz. The respective values measured by stroboscopic holography in two different TMs reported by Cheng et al., (2013) were 200/200, 30/35, and 16/8 nm/Pa at 1, 4, and 10 kHz. In this study, the values of maximum displacement on the surface of TM 60 were 180, 30, and 20nm/Pa at 1, 4, and 8 kHz. Considering the individual differences between the samples, the values measured in this study were consistent with published data. The shape of the displacement contours was another critical parameter to evaluate the mobility of the TM. At 1 kHz, a single prominent peak was observed in the posterior-superior area of the TM (Fig. 4.5). The location of the peak reported in this study was closer to what was reported by Cheng et al., (2013). In Zhang and Gan (2014), the peak emerged in the posterior-inferior region of the TM. However, the peak area appeared in the posterior region in the previous and current studies, which was also observed in the surface motion of other animals at the low frequencies (Rosowski et al., 2009, 2013; Wang et al., 2016). At 4 kHz, a half-ring-shaped or ring-shaped high displacement area covered the most of regions of TM except

the superior region was observed in TMs in this study and two previous studies. At 8 kHz, multiple high displacement areas were in shape of concentric circles centered at the umbo and spread out to the TM annulus, which was also observed in Cheng et al. (2013) and Zhang and Gan (2014). Overall, the full-field surface motion measured in this study is consistent with published data.

4.4.2 Comparison between the simulation and experimental results

The full-field TM motion was measured experimentally (Fig. 4.5-4.7) and simulated by FE model (Fig. 4.9). The maximum displacement on the TM surface predicted by the FE model was 118, 16.3, and 4.5 nm/Pa which was consistent with the experimental data of 180, 30, and 20nm/Pa in TM 60 at 1, 4 and 8 kHz, The major peak in the posterior-inferior region of the TM was observed in the normal TM at frequencies below 4 kHz in both Fig. 4.5 and 4.9. Multiple peaks emerged on the TM surface including the superior was observed at 8 kHz in both experimental and model-derived data. Therefore, the multilayer fibrous model of TM was capable to simulate the behavior of normal TM over the frequency range.

The key functionality of the new FE model of TM was to simulate the blast-induced microstructural damage in TM. Figure 4.6 and 4.7 demonstrated a typical characteristic of the change in the full-field surface motion of TM after experiencing the blast exposure: Increase in the maximum magnitude of the displacement at the major peak in the posterior region at the frequencies between 3-4 kHz without altering the distribution of the displacement on the surface of the TM. As it was shown in Fig. 4.5, the normal TM might exhibit higher displacement at the frequencies below 2 kHz or higher than 4 kHz, but the increased mobility was observed in all 4 samples at 3- 4 kHz. The deflection

shapes of TMs in the reduced volume fraction and "hole" group presented in Fig. 4.9 generally followed the same trend of the experimental data. The major peak in the TM with reduced elastic moduli disappeared at frequencies over 3 kHz, which indicated the overall stiffness of the TM in the simulation was lower than the experimental value. It could be explained by the fact that the elastic modulus was reduced by a scale of 1,000, which mimicked the situation of complete loss of all the fibers. The relative higher TM stiffness in the experimental data suggested that the fiber structure was not completely destroyed in the experiment. Moreover, the volume fraction was reduced to only 1/10 of its original value. With the increase of the frequency, it could be observed from the volume fraction group followed the trend of the experimental data well. The multiple peaks and ring-shaped high-displacement area over the entire surface of TM were not observed in high-frequency vibration modes of TM lower than 8 kHz. In the "hole" group, the major peak of displacement was too prominent that there were no peaks with an amplitude comparable with it even at 8 kHz. Figure 4.9 also showed a secondary peak forming inside the "hole area" which indicated the existence of short-wavelength peaks inside the hole area. Both of these phenomena were not observed in the experimental data, which suggested the difference of the stiffness in and outside of the "hole" area was greater in the model than in the reality.

For quantitative analysis on the TM full-field surface motion, the normalized displacement-frequency curves of a point selected at the center of the major peak at 3 kHz in TM 60 (Fig. 4.10a) before and after the blast exposure were plotted in the Fig. 4.10b. The red line represented the data obtained after the blast while the black line represented the results from TM before the blast. The peak frequency of the red and black curves was

almost the same while the peak value of the red curve was approximately 50 nm/Pa higher than the black curve to reach a value at 180 nm/Pa. In the frequency range between 1 to 4 kHz, the displacement at this peak point increased after the blast exposure. The respective model-derived data was presented in Fig. 4.11. The normalized displacement-frequency curves of the point selected from the center of the major peak shown in the Fig. 4.9. Figure 4.11a shows the comparison between the normal and low elastic moduli TMs. Noted the R or C curves represented the elastic moduli were only adjusted in the fibers in the radial or circumferential direction. The R&C curve represented the results obtained from the TM with adjusted fibers in both directions. Fig. 4.11a suggests that the decrease of the elastic moduli increases the maximum displacement magnitude from 120 nm/Pa to over 600 nm/Pa while results in a very limited shift of the peak to the lower frequencies. The reduced elastic moduli in both directions induced a more significant effect on the maximum displacement than the adjustment made in only one direction and the effect of the radial and circumferential direction showed no difference. Figure 4.11b demonstrates results obtained from the FE model showing the effect of fiber volume fraction in the same manner as the Fig. 4.11a. Reducing the volume fraction of fiber to 1/10 of its original value resulted in an increase of maximum displacement of 120 nm/Pa but there was no evidence for the existence of the directional-specific effect. The comparison between the normal and "hole" group is shown in Fig. 4.11c. The peak frequency of the curve obtained from the damaged TM exhibits a slightly lower peak frequency and an increase in the maximum value at a level of 280 nm/Pa. Special attention is paid to the shape of the red curve who exhibits a peak wider than the normal curve. This phenomenon is also shown in the experimental data shown in Fig. 4.10b. Therefore, the maximum

displacement curves obtained from three types of simulated damage shared common features with the experimental data. The blast-induced damage in TM was unlikely to be completely destroyed the fiber system but resulted in a combination of regional and global loss or damage of fibers which increased the mobility of the membrane in the region where the maximum displacement emerged at frequencies below 4 kHz.
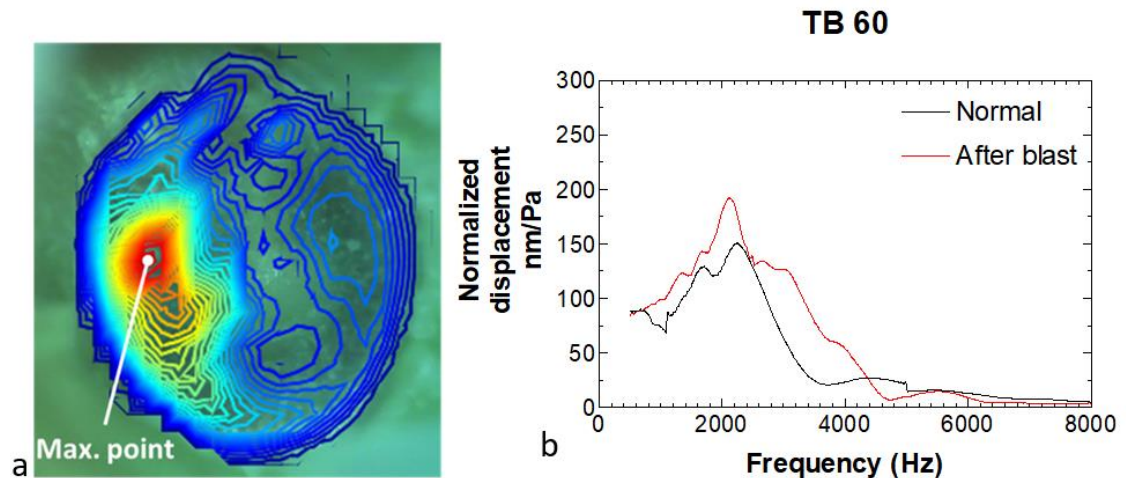
Figure 4.10 (a) Displacement contours of TB-60 at 3 kHz showing the location of the selected point; (b) maximum displacement normalized by the sound input measured from the TB-60 before and after the blast exposure.

4.4.3 Contribution and limitation of this study

Rupture of the TM is a typical injury in the auditory system induced by blast exposure which can cause severe hearing loss and pain (Gan et al., 2016; M.CPT et al., 2015; Patterson and Hamernik, 1997). However, recent biomechanical measurement on the TM after blast exposure lead us into a new field of microstructural damage in TM even if there was no discernable existence of the rupture (Engles et al., 2017; Luo et al., 2016). Moreover, progressive hearing loss after blast exposure was observed in human and animals experienced blast exposure (Bohne et al., 2017; Race et al., 2017). The role of the middle ear, especially the TM in the process of post-blast hearing damage or

recovery process remains unclear. This study directly measured the full-field surface motion of TM which was a critical data for understanding the sound transmission function of the middle ear. By viewing the displacement contours over the frequency of 1-8 kHz, the major peak located in the posterior region of TM was observed, and thus the increase in maximum displacement at 3-4 kHz was further discovered, which provided us with some insights on the frequency-specific and localized increase of the TM mobility in ears experiencing blast exposure. However, the relationship between this type of mobility increase and the progressive hearing loss after blast exposure still requires further investigations. Measurement on the stapes footplate in TBs experienced blast exposure may be necessary for the following studies. The result of this study also proves the SLDV is capable of being a refined method to detect subtle changes in the behavior of TM resulted by the microstructural changes.

Moreover, the multilayer model of TM including radial and circumferential fiber network was successfully constructed in this study. The model was proved to be able to characterize the structure-function relationship of the normal and damaged TM under a frequency range from 1 to 8 kHz. This model enables the experimental results obtained from the biomechanical measurement based on the fibrous structure of TM to be directly used for prediction on the function of the membrane under normal and damaged situations by adjusting the mechanical properties and density of the collagen fibers. The multilayer design also allows more sophisticated microstructural level studies on TM such as the regional or directional-dependent discontinuity of fibers or interlayer interactions between the fibers and the matrix. The model also improves the capability of the model in stress distribution analysis in fiber and matrix under impulse load to understand the

89

mechanism of the rupturing process of the TM in future studies on the blast-induced auditory damage. The evaluation on the TM graft of fibrous structure (Kozin et al., 2016) or the simulation of interlayer edema in TM resulted by otitis media (Guan et al.) are both possible clinical-relevant application of this model in the following studies.

There are still limitations in the current study. In Fig. 4.5, the 1 kHz results show a higher displacement in the TM before blast exposure. Other samples also exhibited higher maximum displacement in normal TMs higher than the blasted ones at frequency range lower than 3 kHz. These discrepancies may be resulted from the surgical approach. During the surgery of exposing the TM, the ear canal was not completely disconnected from the TM annulus for maintaining the integrity of the outer ear structure under blast exposure. Therefore, at superior edge of some of the samples, the epidermal layer of TM was connected to the ear canal tissue and the low-frequency results were affected. Noted the fact that in Fig. 4.5, at the location where the peak appeared at 2 kHz, the displacement value at 1 kHz was still higher after the blast exposure. The second problem was the mechanical properties of the TM model requires further adjustment. To simulate the damage and emphasize the effect of fibers, the average stiffness of the TM model was relatively high which resulted in a smaller normalized displacement than the experimental data (Fig 4.5&4.9). The viscoelastic behavior of the collagen fibers will also need to be considered to improve the accuracy of the model, especially at high frequencies.
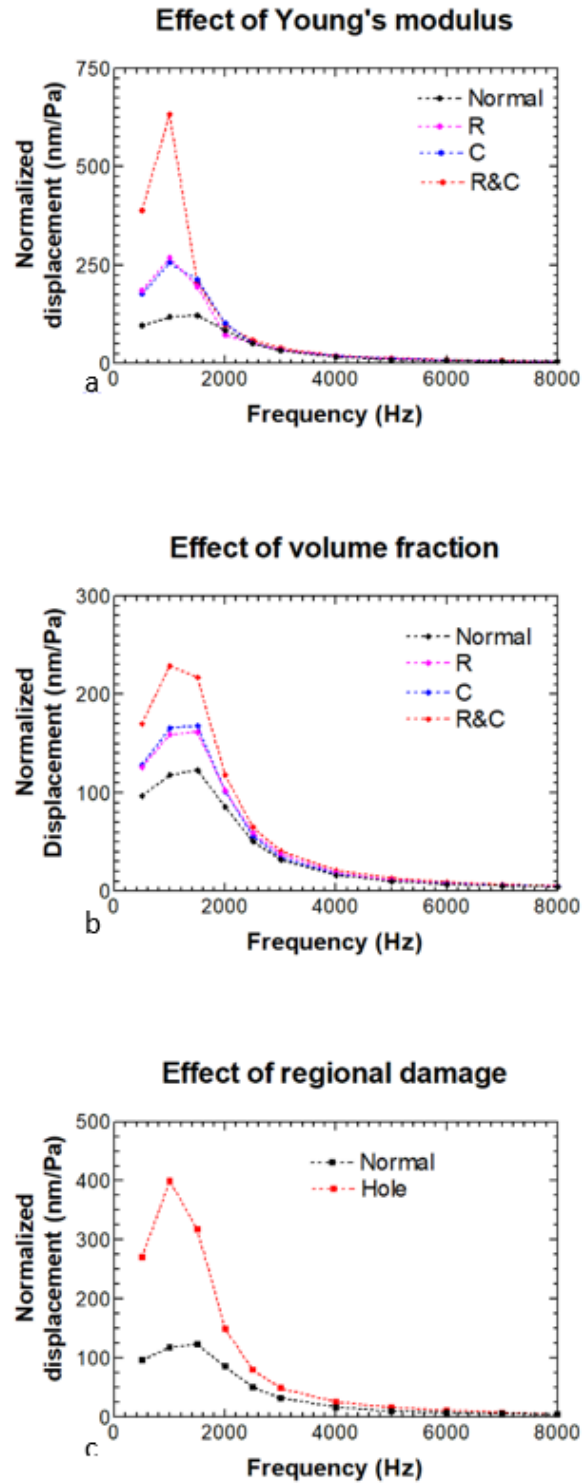
Figure 4.11 Model-derived normalized displacement of the point selected from the center of the posterior-inferior region of the TM where the maximum displacement: (a) the normal and reduced elastic moduli TMs; (b) the normal and reduced fiber volume fraction TMs; (c) the normal and TM with partially removed fibers.

91

4.5 Conclusion

The full-field surface motion of human TM was measured by SLDV over a frequency range from 1 to 8 kHz. An FE model of human TM with multilayer microstructure and embedded by a fiber network was built to simulate the experimental results in both normal and damaged situations. A major displacement peak whose magnitude increased after the blast exposure emerged in the posterior region of the TM was observed in all samples at the frequencies between 3-4 kHz. The model-derived data successfully characterized the features of the surface motion measured from the normal and damaged ear and suggested the blast-induced damage might be a combination of global and regional discontinuity of fibers. This study provides a method to detect the subtle damage to the TM to improve the understanding of post-blast injuries or recoveries in the auditory system. The model built in this study provides a practical tool for microstructural level biomechanical analysis on TM.

Chapter 5   Movement of Human Tympanic Membrane under Blast Exposure Measured by Laser Doppler Vibrometry

(Under review)

5.1 Introduction

The sound transfer function of the human middle ear is initiated by the TM transform the pressure wave into the mechanical vibration of the ossicular chain. Based on an engineering function for a system like the middle ear, its sound-transfer function can be described by the relationship between the sound pressure at the ear canal and the displacement of the TM vibration. Laser Doppler Vibrometry (LDV) is a well-developed technique widely used to measure the vibration of TM in a series of studies to evaluate the function of the middle ear in normal human TBs (Gan et al., 2004b), in human TBs with fluid (Dai and Gan, 2008), in normal and infected chinchillas (Guan et al., 2014), in guinea pigs(Wang et al., 2016) and in artificial TM graft(Kozin et al., 2016). However, the transfer function of the TM has not been measured under blast exposure. For understanding the mechanism of the blast-induced injuries in the ear and characterizing the behavior of the ear in response to the blast overpressure, a dual-laser LDV setup was established to capture the real-time motion of the TM in the period of time during which the blast waves propagate through the ear. The results are crucial for the understanding the mechanism of the rupture or microstructural damage induced by the blast and provide references for blast-related finite element (FE) models.

5.2 Methods

5.2.1 Sample preparation

Five fresh human TBs with an average age of 78.2 (64-87) were involved in this study. Temporal bones were packed in dry ice, shipped from the Life Legacy Foundation. The experiments were conducted within one week after the temporal bones arrived. The samples were processed with a solution of 0.9% saline and 15% povidone at 5 °C to maintain the physiological condition before the experiment which was the same procedure described in the section 2.2.1. Each sample was examined under a microscope to ensure the ear was free from middle ear diseases.

By the completion of a surgery of expanding the opening of the ear canal, the TM umbo was exposed by removing part of the tragus so that it could be reached by a laser beam emitted from a source outside the ear canal. A reflective tape with a size of 1 mm x 1 mm is attached to the TM umbo to increase the signal intensity (Fig. 5.1a). A pressure sensor P1 (Model 105C02, PCB Piezotronics, Depew, NY) was inserted into the ear canal next to the TM through a surgery-opened approach in the TB (Fig. 5.1b). The P1 was designed to measure the pressure inside the ear canal which directly applied on the TM.
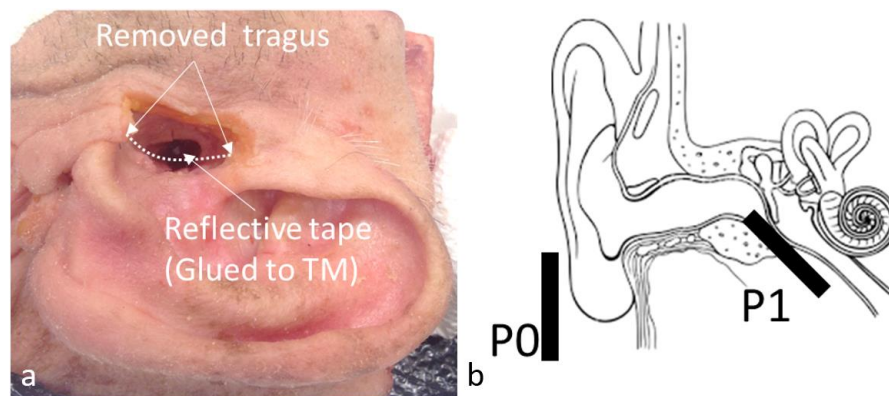
Figure 5.1 Sample preparation: (a) TM is exposed after the surgery; (b) Diagram of the structure of the head block showing the location of P1 and P0 pressure sensors;
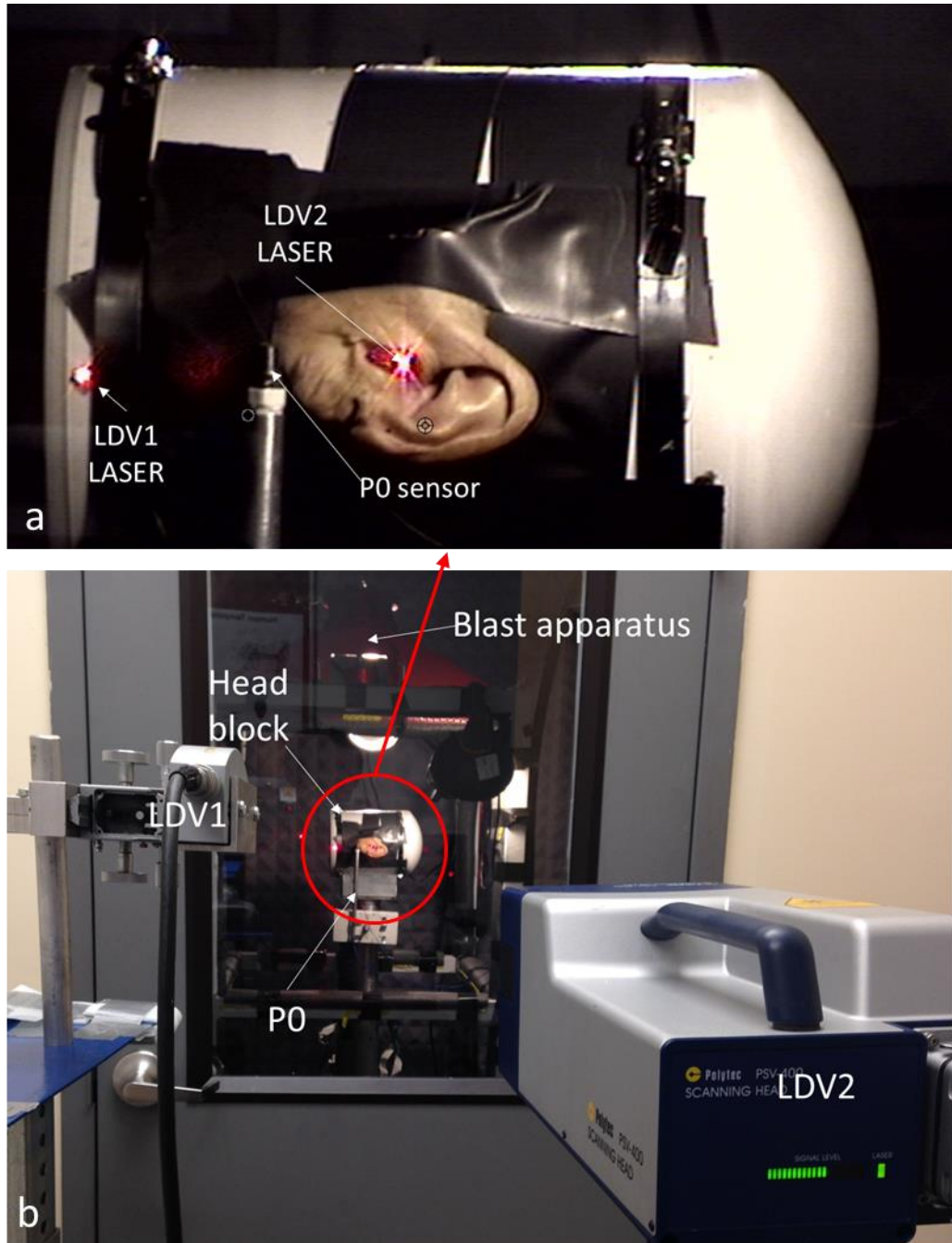
Figure 5.2 Experimental setup: (a) Zoomed-in view of the "head block" showing two lasers are aiming at their targets (b) Experimental setup viewed from the outside of the blast room.

The TB was then fixed to the "head block" which was an artificial human head

with the similar size and shape to simulate a real human skull (Fig 5.2a). The pressure

sensor P0 (Model 102B16, PCB Piezotronics, Depew, NY) was mounted on a column

approximately 1cm lateral to the ear canal opening to monitor the pressure input to the ear (Fig 5.1b & 5.2a). The "head block" was placed under the blast apparatus inside an anechoic chamber. The design of the "head block", blast apparatus, and the chamber was the same as used in the section 4.2.3. To be brief, the blast overpressure was generated by rupturing polycarbonate film(s) (McMaster-Carr, Atlanta, GA) using compressed air. The blast overpressure hit the "head block" in a direction simulating it hit the face of a human head (Fig. 5.2).

5.2.2 Experimental setup

Upon the completion of the sample preparation, the door of the blast chamber was closed and two laser vibrometers were placed outside the blast chamber and the laser beams emitted from the scanning heads transmitted through a transparent window to reach the targets placed on the TM and the "head block" (Fig. 5.2b). A schematic diagram of the experimental setup is shown in the Fig. 5.3. Considering the blast created by the rupture of the film could induce vibration not only in the TM through the air pressure, but also in the "head block" and even the entire blast chamber. Therefore, the laser Doppler vibrometers were placed outside the room on a stable surface to avoid being affected by the vibration created by the blast. In addition, to eliminate the effect of the vibration of the "head block", two laser Doppler vibrometers were applied to measure the motion of TM relative to the "head block". The LDV1 (Polytec CLV 2534, Tustin, CA) aimed at the "head block" to measure the movement of the "head block", the LDV2 (PSV-400, Polytec Inc., Irvine, CA) aimed at the TM to measure the movement of the TM combined with the system (Fig 5.2b&5.3). Two laser beams were aligned in the direction perpendicular to the TM annular plane and parallel to each other. The vibration of the

"head block" was eliminated by subtracting the velocity measured from the LDV1 from the velocity measured from the LDV2. The data acquisition system was the same as it was described in the section 4.2.3. The data acquisition system consisted of a cDAQ 7194, A/D converter 9215 (National Instruments Inc., Austin, TX), and a software package LabVIEW (National Instruments Inc., Austin, TX) which collected and synchronized the signals from the pressure sensors and two LDVs. The sampling rate of the signals measured from P0, P1, LDV1, and LDV2 was 100 kHz. When the front of the blast overpressure arrived at the P0, it triggered the P1 and two LDVs to start recording the signals at the length of 5 ms after the trigger. The P0 level is designed to be around 34 kPa in this study.

5.3 Results

5.3.1 Sound-transfer function measurement of TM under blast overpressure

The typical results obtained from the sample #5 are displayed in the Fig. 5.4. The pressure data recorded by P1 and P0 are plotted as functions of time in Fig. 5.3a. The black P0 curve shows a shape of typical Fried Landers curve with a peak pressure level of 30 kPa. The red P1 curve shows peak pressure level of 69 kPa which is twice as high as the P0 peak pressure. The increased P1 pressure level compared to P0 demonstrates the amplification function of the pinna and ear canal on the blast overpressure. Both P0 and P1 were attenuated within 1 ms. The P1 curve shows more high-frequency fluctuations comparing to the P0 curve after the major peak. Figure 5.4b shows the velocity data measured from the LDV1 and LDV2. Negative values on the velocity curves indicated the TM velocity was in the direction into the middle ear cavity. It could be clearly observed that the movement of the TM is significantly higher than the movement

97

of the head block in the direction of measurement. The velocity obtained after removing the head block vibration is shown in Fig. 5.4c. The TM velocity did not reach its maximum value at the very beginning, but at the second cycle after the blast arrived. The displacement of TM calculated by integrating the velocity over time is plotted in the Fig. 5.4d. The displacement curve indicates that the TM moved into the middle ear cavity at the start in response to the blast overpressure, then vibrated at an amplitude of 0.4 mm for two cycles and the amplitude diminished after 1 ms. The peak pressure amplitude of curves obtained from P0 and P1 sensor were recorded as the input pressure of the middle ear and named P0 and P1, respectively (Fig 5.4a). The maximum values of the peak to peak velocity and displacement were recorded as ΔV and ΔD, respective which represented the response of the TM to the blast overpressure. The P0, P1, ΔV, ΔD, and the ΔD normalized by P0 obtained five samples are listed in Table 5.1 with mean and SD. The $\Delta D/P0$ values represented the sound transfer function of the TM. The data suggests that at a P0 level of 34.3 ± 5.2 kPa, the blast overpressure results in a P1 of 61.1 ± 23.0 kPa, a ΔV of 12.62 ± 3.63 m/s and a ΔD of 0.78 ± 0.26 mm which equals to a normalized displacement of 0.02 29 $\pm$ 0.0066 mm/kPa.

Table 5.1 Quantitative results of five samples

Sample number	P0 (kPa)	P1 (kPa)	ΔV (m/s)	ΔD(mm)	$\Delta D/P0$ (mm/kPa)
#1	31.0	35.9	8.44	0.55	0.0176
#2	31.0	96.5	9.32	0.73	0.0236
#3	40.0	53.1	13.20	0.59	0.0148
#4	40.0	51.0	15.81	1.20	0.0300
#5	30.0	69.0	16.32	0.84	0.0284
Mean $\pm$ SD	34.3 ± 5.2	61.1 ± 23.0	12.62 ± 3.63	0.78 ± 0.26	0.0229 ± 0.0066
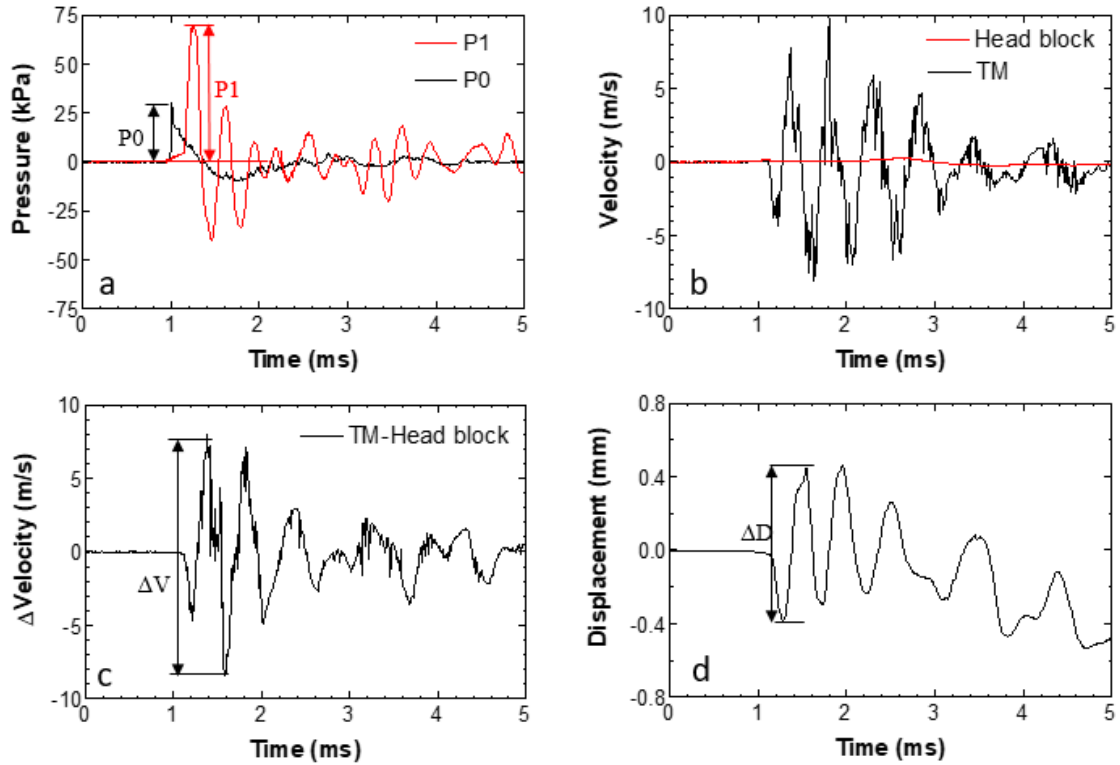
Figure 5.3 Typical results from TB #5: (a) Pressure curves obtained from P0 and P1 sensor; (b) raw velocity data obtained from LDV1 and LDV2; (c) TM velocity after the subtracting head block velocity from the TM velocity; (d) TM displacement curves obtained from the inter.

Considering the fact that the result focuses on the transient response of the TM and the experimental environment involved many possible interferences on the results, the consistency of the experiment was examined by repeating the blast test on the same sample for five times at the same blast level to observe the differences among the output. Under the exactly same experimental condition, the TM velocity curves (before subtraction) of the sample #1 was examined for five times and the curves were shown in Fig. 5.5. Curves obtained from five individual tests overlapped on each other which confirmed that the consistency of this experiment was good.
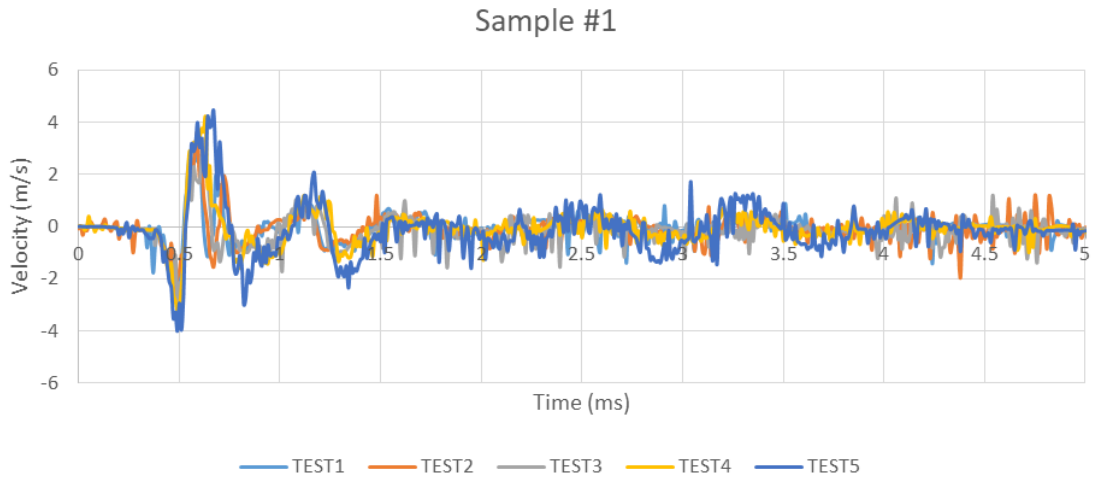
Figure 5.4 Velocity-time curves obtained by 5 repeated blast tests on Sample #1
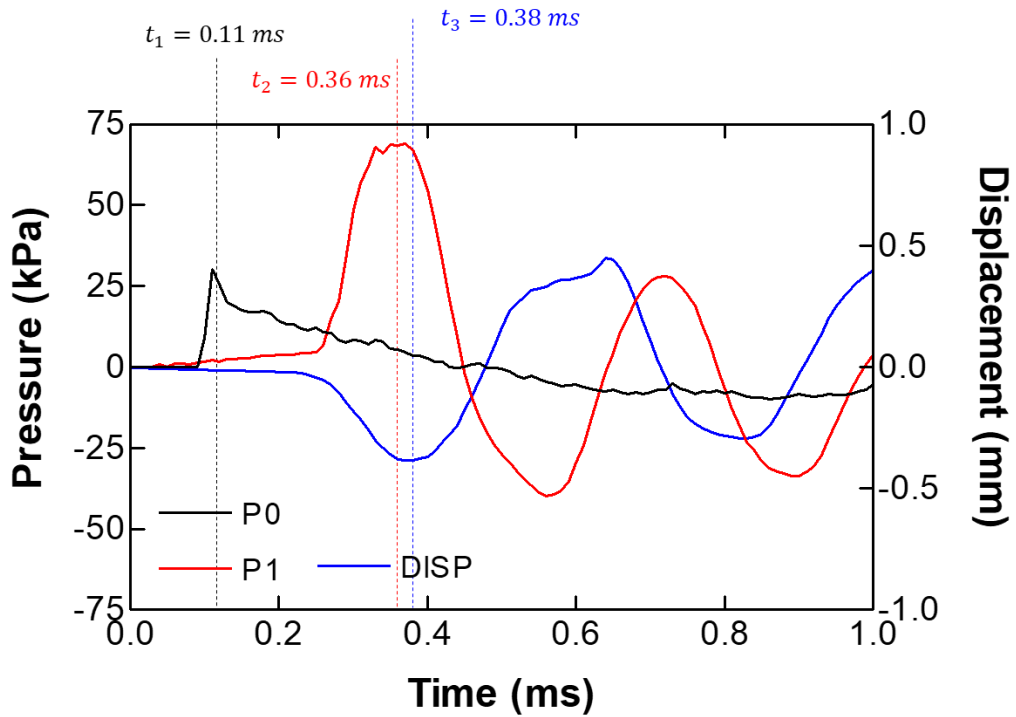
Figure 5.5 Time delay between P0, P1 and displacement signals

5.3.2 TM movement delay

The P0, P1, and displacement signals are plotted on the same time scale in Fig.

5.5. The left y-axis is the pressure while the right axis is the displacement. The time point

100

at which P0 reaches its peak is marked as t_1. Similarly, t_2 is the time point at which P1 and t_3 is the time point for the displacement, respectively. Therefore, the time delay between P0 and P1 was calculated as t_2-t_1, and the time delay between the P1 and displacement was calculated as t_3-t_2, which demonstrated the delayed response of the ear under blast overpressure. Figure 5.5 showed the time delay between the t_1 and t_2 is 0.25 ms. The time delay between t_2 and t_3 is 0.02 ms. It indicated that the blast overpressure took 0.25 ms to propagate through the ear canal to reach the TM. The TM took 0.02 ms to respond to the pressure and start deforming.

5.3.3 Frequency domain analysis on the velocity signal of TM

Based on the waveforms of the TM velocity, a fast Fourier transformation was conducted to analyze the frequency components of the velocity signal. Figure 5.6 exhibits the frequency spectrum of the velocity signal based on a sampling rate of 100 kHz obtained from sample #5. Most of the frequency components are below 5 kHz. There is a sharp peak at 2 kHz with an amplitude of 1.4 m/s. The shape of the curves of 5 samples over the frequency range is similar to each other. The summary of the results obtained from 5 samples is listed in Table 5.2 showing the amplitudes and frequency of the peak of the frequency spectrum. The peak frequencies are between 2-3 kHz and the amplitude varies from 0.51 to 1.4 m/s

Table 5.2 Frequency domain analysis results of the velocity signals

Sample number	#1	#2	#3	#4	#5
Velocity Amplitude (m/s)	0.51	0.60	0.79	1.11	1.40
Frequency (kHz)	2.0	2.0	2.8	2.3	2.0
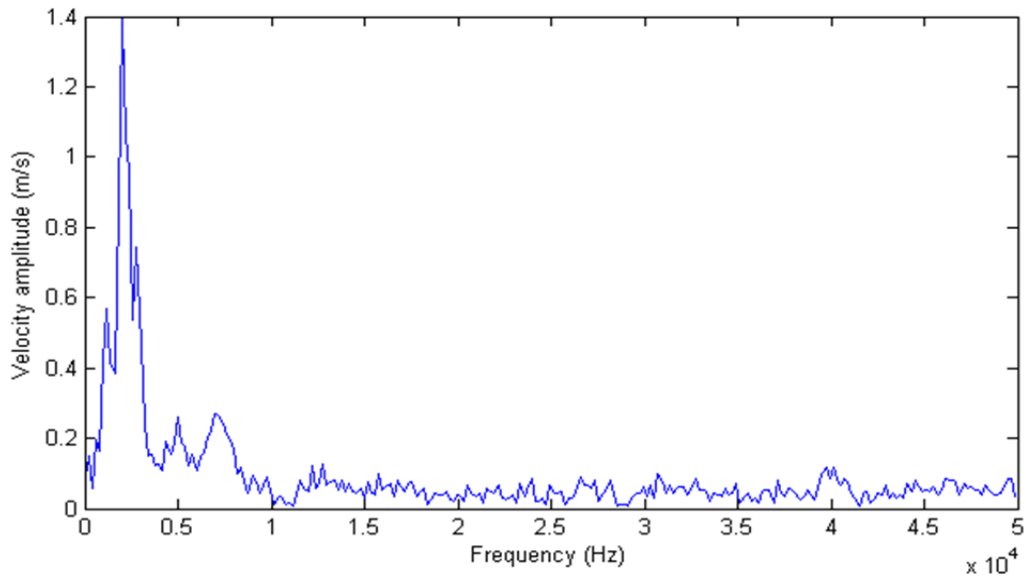
Figure 5.6 Frequency spectrum of the velocity signal of sample #5

5.4 Discussion

5.4.1 Comparison with FE simulation

An FE model of human ear built for blast-related research was built in our laboratory for analyzing the transient response of the ear (Gan et al., 2018). Based on the previous human FE model produced by Gan et al., (2007), this model of the ear was regenerated in ANSYS Workbench (ANSYS Inc., Canonsburg, PA, USA) where Fluent/ANSYS Mechanical coupled fluid-structure interaction analyses were employed to compute blast overpressure transduction from the environment to the TM and middle ear. This model was applied to analyze the distribution of the pressure inside the middle ear under blast exposure and the effect of the direction of the blast wave on the injuries of the TM (Gan et al., 2018; Leckness, 2016). Following the same method presented in Gan et al., 2018, the experimentally recorded P0 waveforms from the head block with were applied at the entrance of the ear canal and the pressure waveforms P1 were then

102

calculated and compared with those measured from the experiments. The waveforms of the displacement of the TM um were also obtained from the FE simulation. The waveforms of P0, P1 and TM umbo displacement are presented in Fig. 5.7. The P1, ΔD t_1, t_2, and t_3 values predicted by the model are compared with the experimental results and listed in Table 5.3. The P1 predicted by the model is lower than the experimental data, but the ΔD is very close to that obtained from the experiment. The model-predicted time delay between the P1 and P0 is shorter than the experimental data, but the delay between the displacement and the P1 is longer than the experimental data. Comparing the waveform in the Fig. 5.5 and 5.7, the order and the peak values of the model-derived P1 and displacement curves are in agreement with the experimental data. However, the cures obtained from the experimental data are smoother than the model predicted curves.
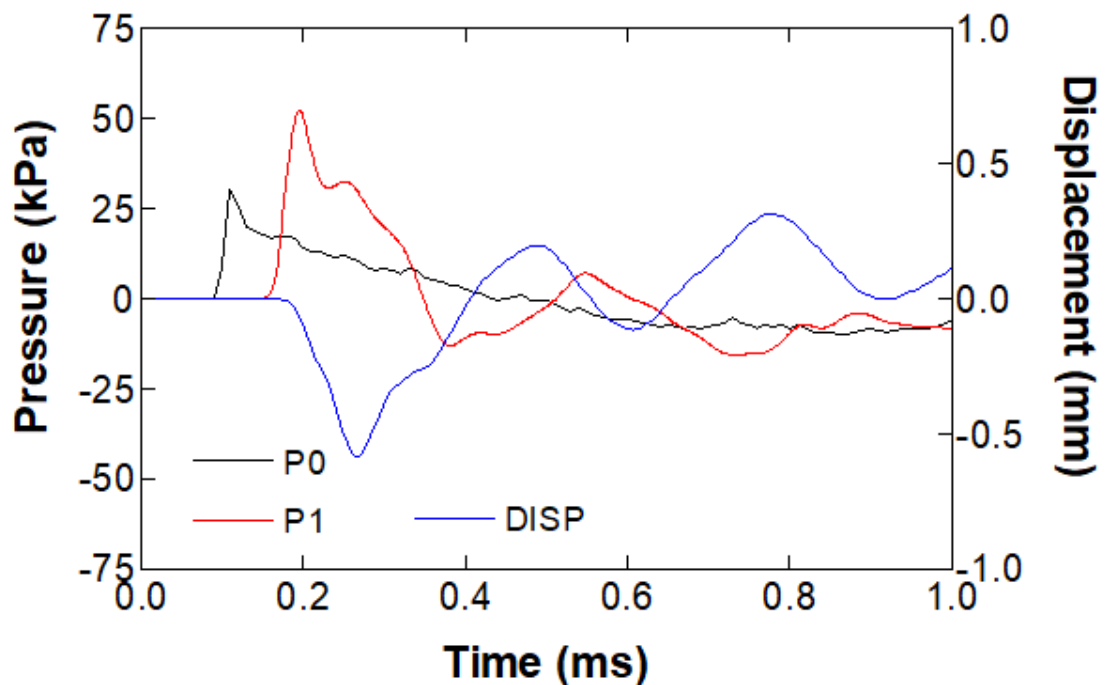
Figure 5.7 The input P0, response P1 and displacement curves calculated from the FE model

Table 5.3 Experimental data compare with the modeling results

	P0 (kPa)	P1 (kPa)	ΔD (mm)	t_1 (ms)	t_2 (ms)	t_3 (ms)
Experiment	29.7	69.0	0.84	0.11	0.36	0.38
Model	29.7	52.4	0.77	0.11	0.20	0.27

The experimental measurement and the model prediction were generally consistent with each other, which indicated that the design and material properties used in the FE model are appropriate to successfully predict the response of the TM to the blast pressure waves. The lower P1 in the model could be resulted by the difference in the geometry or the boundary condition of the ear canal. Noted that a surgery was conducted on the TB in the experiment to expose the TM which might change the pressure amplification function of the outer ear. The location of the P1 sensor could be another factor which resulted in the difference between the experimental data and the model prediction. The location of P1 in the FE model was next to the umbo while the head of the P1 sensor was placed at the inferior edge of the TM. Therefore, the P1 levels were not the same in the model results and the experiment. The difference of the waveform suggested the damping of the FE might need to be adjusted. The time delay differences indicated the viscoelastic properties of the TM in the FE model required further optimization.

5.4.2 Comparison with published data

As far as my knowledge, there is no data on the TM movement under blast overpressure have been reported in the published literature. However, the human TM mobility under acoustic stimulation was reported by Gan et al., (2004b). The peak to peak displacement amplitude of human TM and stapes footplate under a pure tone sound

stimulus of 90 dB SPL is shown in Fig. 5.8. The maximum displacement is shown in Fig. 5.8 was about 0.1 μm at 1 kHz. Therefore, the respective sound transfer function parameter, P0/ΔD was approximately 0.16 μm/Pa. The mean data measured in this current study shown in Table 5.1 is 0.0229 μm/Pa. The ratio between the displacement and input pressure under blast exposure was much lower than the results measured under acoustic load. This indicated the non-linear behavior of the TM and the middle ear under the high-intensity stimulus. Similar nonlinearity was also reported by Cheng et al., (2017). The blast overpressure used in this study was an impulse of the transient air pressure, which was also different from the high-intensity sound. However, the reduced sound transfer function observed in this study was consistent with the high-intensity sound results. This might be resulted from the no linear behavior of the TM and ossicular chain which was also reported by Greene et al., (2017).
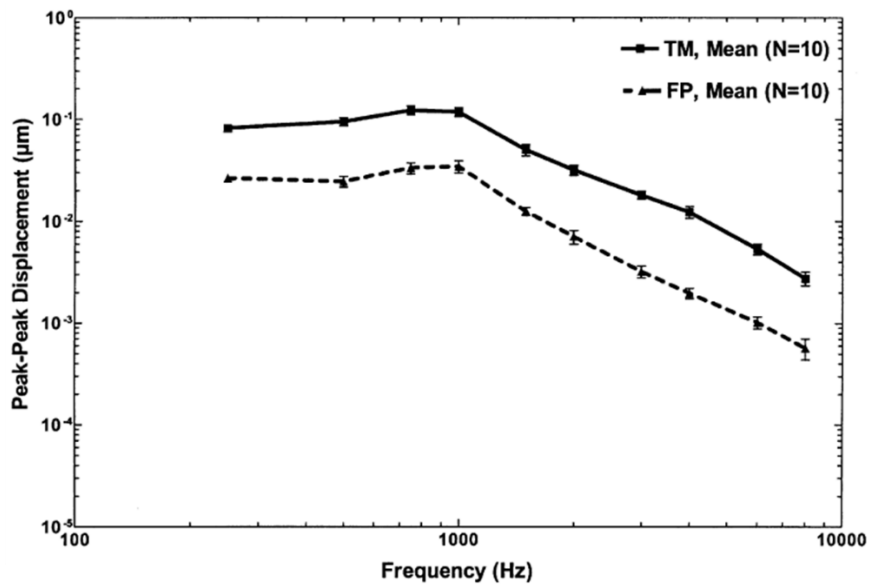
Figure 5.8 Mean (±SE) peak to peak displacement measured at the TM and stapes footplate with the input sound of 90 dB SPL in the ear canal in 10 TBs (Gan et al., 2004b)

5.5 Conclusion

In this study, the movement of human TM under blast overpressure has been measured for the first time using dual-LDV setup. The sound-transfer function of the human TM was quantitatively measured with a result of 0.0229 ± 0.0066 mm/kPa at an input pressure level of 34.3 ± 5.2 kPa. The delayed movement of the TM with respect to the input pressure has been observed and time for the blast wave to propagate through the ear canal has been measured. The frequency domain analysis on the velocity signals indicates the frequency components of the TM vibration in the blast exposure are between 2-3 kHz. The experimental results are in agreement with the FE modeling predictions. This study provides novel ideas on accurate measurement under blast-exposure conditions and quantitative data to understand the formation of the blast-induced injuries, as well as nonlinear behaviors of the middle ear.

Chapter 6   Summary and Future Works

The mechanical properties of the ISJ and TM are important to the sound transmission function of the ear. In this study, biomechanical measurements provide quantitative data on the mechanical properties of the ISJ and TM and characterize their behavior under various conditions. With the assistance of FE simulation, the relationship of the microstructure and behavior of the TM and ISJ under different conditions were investigated. The function of the FE model of predicting the behavior of the ear under blast overpressure could be validated by the experimental data.

In chapter 2 of this dissertation, the dynamic properties of ISJ were measured using DMA assisted by the FTS principles and the FE model of the ISJ simulating its behavior over the frequency range of 1 Hz to 8 kHz was built. This chapter filled in the gap of knowledge in which the dynamic properties of ISJ had not been experimentally determined. Then in the following chapter, the measurement of the ISJ mechanical properties was conducted under the high-strain-rate deformation. The SHTB was applied to the biomechanical measurement of a joint for the first time and the results were consistent with the published data, especially with the values used in previous FE models of the middle ear. The data provided by chapter 2 and 3 may help to improve the quality of the FE model simulating the ear under blast exposure. In chapter 4, the surface motion of both the normal and damaged TM was measured by SLDV. A new TM FE model with a multilayer structure and embedded with a fiber network has been introduced and successfully reproduced the experimentally-measured damage in the simulation. In chapter 5, to characterize the behavior of the entire middle ear under blast exposure, the

movement of TM was measured using dual-laser setup and the results were consistent with the model prediction.

The mechanical properties of ISJ exhibit strong dependence on the frequency and the strain rate, which may indicate the behavior of the joint is very different in the normal and blast-damaged ears. The full-field surface displacement suggests that the mobility of the TM is changed in the damaged ear due to the damaged fibrous microstructure after the blast exposure. The changes of the mechanical properties of TM and ISJ in blast-damaged ears possibly contribute to the abnormal TM displacement measured under blast overpressure, but the detailed mechanism still requires further investigation.

All the research objectives listed in Chapter 1 are fulfilled. The data provided in this dissertation improved the accuracy of the FE model of the human ear and characterize the response of TM and ISJ to harmonic stimuli and blast overpressure. The methods presented in this study could be applied to various types of dynamic biomechanical measurement in future studies.

For future studies, there are a few possible directions listed below:

1) To insert the ISJ and TM FE models with ultrastructure into the FE model of the entire human ear to investigate the effect of microstructural level changes to the function of the ear

2) To develop a split Hopkinson pressure bar to measure the behavior of ISJ under compressive load

3) To measure the movement of the stapes footplate and TM in human TB under blast exposure. These results will be used to calibrate the FE model for blast-induced-damage simulation

References

1. Abdala, C., and Keefe, D.H. (2012). Morphological and Functional Ear Development. In Human Auditory Development, L. Werner, R.R. Fay, and A.N. Popper, eds. (Springer New York), pp. 19–59.

2. Aernouts, J., and Dirckx, J.J.J. (2011). Elastic characterization of the gerbil pars flaccida from in situ inflation experiments. Biomech Model Mechanobiol *10*, 727–741.

3. Aernouts, J., Aerts, J.R., and Dirckx, J.J. (2012). Mechanical properties of human tympanic membrane in the quasi-static regime from in situ point indentation measurements. Hearing Research *290*, 45–54.

4. Alian, W., Majdalawieh, O., Kiefte, M., Ejnell, H., and Bance, M. (2013). The effect of increased stiffness of the incudostapedial joint on the transmission of air-conducted sound by the human middle ear. Otol. Neurotol. *34*, 1503–1509.

5. Bauman, R.A., Ling, G., Tong, L., Januszkiewicz, A., Agoston, D., Delanerolle, N., Kim, Y., Ritzel, D., Bell, R., and Ecklund, J. (2009). An introductory characterization of a combat-casualty-care relevant swine model of closed head injury resulting from exposure to explosive blast. Journal of Neurotrauma *26*, 841–860.

6. Bichara, D.A., O'Sullivan, N.-A., Pomerantseva, I., Zhao, X., Sundback, C.A., Vacanti, J.P., and Randolph, M.A. (2011). The Tissue-Engineered Auricle: Past, Present, and Future. Tissue Engineering Part B: Reviews *18*, 51–61.

7. Bohne, B.A., Kimlinger, M., and Harding, G.W. (2017). Time course of organ of Corti degeneration after noise exposure. Hearing Research *344*, 158–169.

8. Celik, H., Felek, S.A., Islam, A., Demirci, M., Samim, E., and Oztuna, D. (2009). The impact of fixated glass ionomer cement and springy cortical bone incudostapedial joint reconstruction on hearing results. Acta Oto-Laryngologica *129*, 1368–1373.

9. Champion, H.R., Holcomb, J.B., and Young, L.A. (2009). Injuries From Explosions: Physics, Biophysics, Pathology, and Required Research Focus: The Journal of Trauma: Injury, Infection, and Critical Care *66*, 1468–1477.

10. Chan, R.W. (2001). Estimation of viscoelastic shear properties of vocal-fold tissues based on time–temperature superposition. The Journal of the Acoustical Society of America *110*, 1548–1561.

11. Chandra, N., Ganpule, S., Kleinschmit, N.N., Feng, R., Holmberg, A.D., Sundaramurthy, A., Selvan, V., and Alai, A. (2012). Evolution of blast wave

profiles in simulated air blasts: experiment and computational modeling. Shock Waves *22*, 403–415.

12. Chen, W.W., and Song, B. (2010). Split Hopkinson (Kolsky) Bar: Design, Testing and Applications (Springer Science & Business Media).

13. Chen, W., Lu, F., and Cheng, M. (2002). Tension and compression tests of two polymers under quasi-static and dynamic loading. Polymer Testing *21*, 113–121.

14. Cheng, J.T., Aarnisalo, A.A., Harrington, E., Hernandez-Montes, M. del S., Furlong, C., Merchant, S.N., and Rosowski, J.J. (2010). Motion of the surface of the human tympanic membrane measured with stroboscopic holography. Hearing Research *263*, 66–77.

15. Cheng, J.T., Hamade, M., Merchant, S.N., Rosowski, J.J., Harrington, E., and Furlong, C. (2013). Wave motion on the surface of the human tympanic membrane: Holographic measurement and modeling analysis. The Journal of the Acoustical Society of America *133*, 918–937.

16. Cheng, J.T., Remenschneider, A., Kozin, E., Furlong, C., and Rosowski, J.J. (2017). Nonlinear response of human middle ear to high level sound. The Journal of the Acoustical Society of America *141*, 3897–3898.

17. Cheng, T., Dai, C., and Gan, R.Z. (2006). Viscoelastic Properties of Human Tympanic Membrane. Ann Biomed Eng *35*, 305–314.

18. Choi, C.-H. (2012). Mechanisms and Treatment of Blast Induced Hearing Loss. Korean Journal of Audiology *16*, 103.

19. Dai, C., and Gan, R.Z. (2008). Change of middle ear transfer function in otitis media with effusion model of guinea pigs. Hearing Research *243*, 78–86.

20. Daphalapurkar, N.P., Dai, C., Gan, R.Z., and Lu, H. (2009). Characterization of the linearly viscoelastic behavior of human tympanic membrane by nanoindentation. Journal of the Mechanical Behavior of Biomedical Materials *2*, 82–92.

21. Decraemer, W.F., and Funnell, W.R.J. (2008). Anatomical and mechanical properties of the tympanic membrane. Chronic Otitis Media. Pathogenesis-Oriented Therapeutic Management 51–84.

22. Decraemer, W.F., Maes, M.A., and Vanhuyse, V.J. (1980). An elastic stress-strain relation for soft biological tissues based on a structural model. Journal of Biomechanics *13*, 463–468.

23. Engles, W.G., Wang, X., and Gan, R.Z. (2017). Dynamic Properties of Human Tympanic Membrane After Exposure to Blast Waves. Ann Biomed Eng *45*, 2383–2394.

24. Fan, J.T., Weerheijm, J., and Sluys, L.J. (2015). High-strain-rate tensile mechanical response of a polyurethane elastomeric material. Polymer *65*, 72–80.

25. Fay, J., Puria, S., Decraemer, W.F., and Steele, C. (2005). Three approaches for estimating the elastic modulus of the tympanic membrane. Journal of Biomechanics *38*, 1807–1815.

26. Ferrazzini, M. (2003). Virtual middle ear: a dynamic mathematical model based on the finite element method (ETH Zurich).

27. Ferry, J.D. (1950). Mechanical Properties of Substances of High Molecular Weight. VI. Dispersion in Concentrated Polymer Solutions and its Dependence on Temperature and Concentration. J. Am. Chem. Soc. *72*, 3746–3752.

28. Ferry, J.D. (1980). Viscoelastic Properties of Polymers (John Wiley & Sons).

29. Fung, Y.C. (2013). Biomechanics: Mechanical Properties of Living Tissues (Springer Science & Business Media).

30. Funnell, W.R.J., Siah, T.H., McKee, M.D., Daniel, S.J., and Decraemer, W.F. (2005). On the Coupling Between the Incus and the Stapes in the Cat. JARO *6*, 9–18.

31. Gan, R.Z., and Wang, X. (2007). Multifield coupled finite element analysis for sound transmission in otitis media with effusion. The Journal of the Acoustical Society of America *122*, 3527–3538.

32. Gan, R.Z., and Wang, X. (2015). Modeling microstructure of incudostapedial joint and the effect on cochlear input. In AIP Conference Proceedings, (AIP Publishing), p. 060011.

33. Gan, R.Z., Feng, B., and Sun, Q. (2004a). Three-Dimensional Finite Element Modeling of Human Ear for Sound Transmission. Annals of Biomedical Engineering *32*, 847–859.

34. Gan, R.Z., Wood, M.W., and Dormer, K.J. (2004b). Human middle ear transfer function measured by double laser interferometry system. Otol. Neurotol. *25*, 423–435.

35. Gan, R.Z., Sun, Q., Feng, B., and Wood, M.W. (2006). Acoustic–structural coupled finite element analysis for sound transmission in human ear—Pressure distributions. Medical Engineering and Physics *28*, 395–404.

36. Gan, R.Z., Reeves, B.P., and Wang, X. (2007). Modeling of Sound Transmission from Ear Canal to Cochlea. Ann Biomed Eng *35*, 2180–2195.

37. Gan, R.Z., Zhang, X., and Guan, X. (2011). Modeling Analysis of Biomechanical Changes of Middle Ear and Cochlea in Otitis Media. In AIP Conference Proceedings, (AIP Publishing), pp. 539–544.

38. Gan, R.Z., Nakmali, D., Ji, X.D., Leckness, K., and Yokell, Z. (2016). Mechanical damage of tympanic membrane in relation to impulse pressure waveform – A study in chinchillas. Hearing Research *340*, 25–34.

39. Gan, R.Z., Leckness, K., Nakmali, D., and Ji, X.D. (2018). Biomechanical Measurement and Modeling of Human Eardrum Injury in Relation to Blast Wave Direction. Mil Med *183*, 245–251.

40. Gentil, F., Parente, M., Martins, P., Garbe, C., Santos, C., Areias, B., Branco, C., Paço, J., and Jorge, R.N. (2016). Effects of the fibers distribution in the human eardrum: A biomechanical study. Journal of Biomechanics *49*, 1518–1523.

41. Gilat, A., Goldberg, R.K., and Roberts, G.D. (2002). Experimental study of strain-rate-dependent behavior of carbon/epoxy composite. Composites Science and Technology *62*, 1469–1476.

42. Greene, N.T., Jenkins, H.A., Tollin, D.J., and Easter, J.R. (2017). Stapes displacement and intracochlear pressure in response to very high level, low frequency sounds. Hearing Research *348*, 16–30.

43. Guan, X., Chen, Y., and Gan, R.Z. (2014). Factors affecting loss of tympanic membrane mobility in acute otitis media model of chinchilla. Hearing Research *309*, 136–146.

44. Guan, X., Jiang, S., Seale, T.W., Hitt, B.M., and Gan, R.Z. (2015). Morphological changes in the tympanic membrane associated with Haemophilus influenzae-induced acute otitis media in the chinchilla. International Journal of Pediatric Otorhinolaryngology *79*, 1462–1471.

45. Guan, X., Seale, T.W., and Gan, R.Z. (2017). Factors affecting sound energy absorbance in acute otitis media model of chinchilla. Hearing Research *350*, 22–31.

46. Guan, X., Jiang, S., Seale, T.W., Hitt, B.M., and Gan, R.Z. Morphological changes in the tympanic membrane associated with Haemophilus influenzae-induced acute otitis media in the chinchilla. International Journal of Pediatric Otorhinolaryngology.

47. Hackley Steven A. (2015). Evidence for a vestigial pinna-orienting system in humans. Psychophysiology *52*, 1263–1270.

48. Hitt, B.M., Wang, X., and Gan, R.Z. (2017). Dynamic property changes in stapedial annular ligament associated with acute otitis media in the chinchilla. Medical Engineering & Physics *40*, 65–74.

49. Jiang, S., and Gan, R.Z. (2018). Dynamic properties of human incudostapedial joint—Experimental measurement and finite element modeling. Medical Engineering and Physics *54*, 14–21.

50. Jiang, S., Seale, T.W., and Gan, R.Z. (2016). Morphological changes in the round window membrane associated with Haemophilus influenzae-induced acute otitis media in the chinchilla. International Journal of Pediatric Otorhinolaryngology *88*, 74–81.

51. Karmody, C.S., Northrop, C.C., and Levine, S.R. (2009). The Incudostapedial Articulation: New Concepts. [Miscellaneous Article]. Otology & Neurotology *30*, 990–997.

52. Keller, M., Sload, R., Wilson, J., Greene, H., Han, P., and Wise, S. (2017). Tympanoplasty following Blast Injury. Otolaryngol Head Neck Surg 0194599817717486.

53. Kingery, C.N., and Pannill, B.F. (1964). PEAK OVERPRESSURE VS SCALED DISTANCE FOR TNT SURFACE BURSTS (HEMISPHERICAL CHARGES) (ARMY BALLISTIC RESEARCH LAB ABERDEEN PROVING GROUND MD, ARMY BALLISTIC RESEARCH LAB ABERDEEN PROVING GROUND MD).

54. Kirikae, I. (1960). The structure and function of the middle ear (University of Tokyo Press).

55. Koch, M., Eßinger, T.M., Stoppe, T., Lasurashvili, N., Bornitz, M., and Zahnert, T. (2016). Fully implantable hearing aid in the incudostapedial joint gap. Hearing Research *340*, 169–178.

56. Kozin, E.D., Black, N.L., Cheng, J.T., Cotler, M.J., McKenna, M.J., Lee, D.J., Lewis, J.A., Rosowski, J.J., and Remenschneider, A.K. (2016). Design, fabrication, and in vitro testing of novel three-dimensionally printed tympanic membrane grafts. Hear. Res. *340*, 191–203.

57. Kuypers, L.C., Decraemer, W.F., and Dirckx, J.J.J. (2006). Thickness Distribution of Fresh and Preserved Human Eardrums Measured with Confocal Microscopy. Otology & Neurotology *27*, 256.

58. de La Rochefoucauld, O., and Olson, E.S. (2010). A sum of simple and complex motions on the eardrum and manubrium in gerbil. Hearing Research *263*, 9–15.

59. Landel, R.F., and Nielsen, L.E. (1993). Mechanical Properties of Polymers and Composites, Second Edition (CRC Press).

60. Leckness, K. (2016). Novel Finite Element Method to Predict Blast Wave Transmission Through Human Ear.

61. Liang, J., Luo, H., Yokell, Z., Nakmali, D.U., Gan, R.Z., and Lu, H. (2016). Characterization of the nonlinear elastic behavior of chinchilla tympanic membrane using micro-fringe projection. Hearing Research *339*, 1–11.

62. Luo, H., Lu, H., and Leventis, N. (2006). The compressive behavior of isocyanate-crosslinked silica aerogel at high strain rates. Mechanics of Time-Dependent Materials *10*, 83–111.

63. Luo, H., Dai, C., Gan, R.Z., and Lu, H. (2009). Measurement of Young's Modulus of Human Tympanic Membrane at High Strain Rates. J Biomech Eng *131*, 064501–064501.

64. Luo, H., Jiang, S., Nakmali, D.U., Gan, R.Z., and Lu, H. (2016). Mechanical Properties of a Human Eardrum at High Strain Rates After Exposure to Blast Waves. J. Dynamic Behavior Mater. *2*, 59–73.

65. Maducdoc, M.M., Ghavami, Y., Shamouelian, D., Mahboubi, H., and Djalilian, H.R. (2015). Congenital anomalies of the incudostapedial joint. International Journal of Pediatric Otorhinolaryngology *79*, 2277–2280.

66. Mathews, Z.R., and Koyfman, A. (2015). Blast Injuries. The Journal of Emergency Medicine *49*, 573–587.

67. Mayorga, M.A. (1997). The pathology of primary blast overpressure injury. Toxicology *121*, 17–28.

68. McLellan, M.S., and Webb, C.H. (1957). Ear studies in the newborn infant: natural appearance and incidence of obscuring by vernix, cleansing of vernix, and description of drum and canal after cleansing. The Journal of Pediatrics *51*, 672–677.

69. M.CPT, C., M.CPT, C., and W.COL, C. (2015). Blast Injury of the Ear: Clinical Update from the Global War on Terror. Military Medicine.

70. Middlebrooks, J.C., and Green, D.M. (1991). Sound Localization by Human Listeners. Annual Review of Psychology *42*, 135–159.

71. Miri, A.K. (2014). Mechanical Characterization of Vocal Fold Tissue: A Review Study. Journal of Voice *28*, 657–667.

72. Nakajima, H.H., Dong, W., Olson, E.S., Merchant, S.N., Ravicz, M.E., and Rosowski, J.J. (2009). Differential Intracochlear Sound Pressure Measurements in Normal Human Temporal Bones. JARO *10*, 23.

73. Nie, X., Song, B., Ge, Y., Chen, W.W., and Weerasooriya, T. (2009). Dynamic Tensile Testing of Soft Materials. Exp Mech *49*, 451–458.

74. Ortug, G., Ortug, C., and Aydar, Y. (2006). Configurations of Incudostapedial Joint Surface, An SEM Study. FASEB J *20*, A442–A442.

75. Oskui, I.Z., and Hashemi, A. (2016). Dynamic tensile properties of bovine periodontal ligament: A nonlinear viscoelastic model. Journal of Biomechanics *49*, 756–764.

76. Park, J., Cheng, J.T., Ferguson, D., Maguluri, G., Chang, E.W., Clancy, C., Lee, D.J., and Iftimia, N. (2016). Investigation of middle ear anatomy and function with combined video otoscopy-phase sensitive OCT. Biomedical Optics Express *7*, 238.

77. Patterson, J.H., and Hamernik, R.P. (1997). Blast overpressure induced structural and functional changes in the auditory system. Toxicology *121*, 29–40.

78. Peters, G.W.M., Meulman, J.H., and Sauren, A. a. H.J. (1997). The Applicability of the Time/Temperature Superposition Principle to Brain Tissue. Biorheology *34*, 127–138.

79. Phillips, Y.Y., and Richmond, D.R. (1991). Primary blast injury and basic research: a brief history. Textbook of Military Medicine Part I Warfare, Weapons, and the Casualty. Vol. 5, Conventional Warfare. Ballistic, Blast, and Burn Injuries 221–240.

80. Race, N., Lai, J., Shi, R., and Bartlett, E.L. (2017). Differences in post-injury auditory system pathophysiology after mild blast and non-blast acute acoustic trauma. Journal of Neurophysiology jn.00710.2016.

81. Ritenour, A.E., and Baskin, T.W. (2008). Primary blast injury: Update on diagnosis and treatment. Critical Care Medicine *36*, S311.

82. Rosowski, J., Cheng, J., Merchant, S., Harrington, E., and Furlong, C. (2011). New Data on the Motion of the Normal and Reconstructed Tympanic Membrane. Otol Neurotol *32*, 1559–1567.

83. Rosowski, J.J., Cheng, J.T., Ravicz, M.E., Hulli, N., Hernandez-Montes, M., Harrington, E., and Furlong, C. (2009). Computer-assisted time-averaged holograms of the motion of the surface of the mammalian tympanic membrane with sound stimuli of 0.4–25 kHz. Hearing Research *253*, 83–96.

84. Rosowski, J.J., Dobrev, I., Khaleghi, M., Lu, W., Cheng, J.T., Harrington, E., and Furlong, C. (2013). Measurements of three-dimensional shape and sound-induced motion of the chinchilla tympanic membrane. Hearing Research *301*, 44–52.

85. Sim, R.J., and Chang, P. (2008). Incudostapedial ankylosis from temporomandibular joint disruption. Otolaryngology -- Head and Neck Surgery *139*, 166–167.

86. Stuhlman, O. (1937). The Nonlinear Transmission Characteristics of the Auditory Ossicles. The Journal of the Acoustical Society of America *9*, 119–128.

87. Suzuki, M., Kanebayashi, H., Kawano, A., Hagiwara, A., Furuse, H., Yamaguchi, T., and Shimizu, M. (2008). Involvement of the incudostapedial joint anomaly in conductive deafness. Acta Oto-Laryngologica *128*, 515–519.

88. Szymanski, M., Rusinek, R., Zadrozniak, M., Morshed, K., and Warminski, J. (2014). The Influence of Incudostapedial Joint Separation on the Middle Ear Transfer Function. Clin Exp Otorhinolaryngol *7*, 250–253.

89. Tuck-Lee, J.P., Pinsky, P.M., Steele, C.R., and Puria, S. (2008). Finite element modeling of acousto-mechanical coupling in the cat middle ear. J Acoust Soc Am *124*, 348–362.

90. Vishwakarma, R., More, Y.I., Joseph, S.T., Patel, K.B., Ramani, M.K., and More, R.I. (2009). Incudostapedial joint arthroplasty using temporalis fascia/perichondrium ties. American Journal of Otolaryngology *30*, 171–175.

91. Volandri, G., Di Puccio, F., Forte, P., and Carmignani, C. (2011). Biomechanics of the tympanic membrane. Journal of Biomechanics *44*, 1219–1236.

92. Von Békésy, G., and Wever, E.G. (1960). Experiments in hearing (McGraw-Hill New York).

93. Wang, X., Guan, X., Pineda, M., and Gan, R.Z. (2016). Motion of tympanic membrane in guinea pig otitis media model measured by scanning laser Doppler vibrometry. Hearing Research *339*, 184–194.

94. Wenger, M.P.E., Bozec, L., Horton, M.A., and Mesquida, P. (2007). Mechanical Properties of Collagen Fibrils. Biophysical Journal *93*, 1255–1263.

95. Williams, M.L., Landel, R.F., and Ferry, J.D. (1955). The Temperature Dependence of Relaxation Mechanisms in Amorphous Polymers and Other Glass-forming Liquids. J. Am. Chem. Soc. *77*, 3701–3707.

96. Wolf, S.J., Bebarta, V.S., Bonnett, C.J., Pons, P.T., and Cantrill, S.V. (2009). Blast injuries. The Lancet *374*, 405–415.

97. Yeh, D.D., and Schecter, W.P. (2012). Primary Blast Injuries—An Updated Concise Review. World J Surg *36*, 966–972.

98. Yokell, Z., Wang, X., and Gan, R.Z. (2015). Dynamic Properties of Tympanic Membrane in a Chinchilla Otitis Media Model Measured With Acoustic Loading. J Biomech Eng *137*, 081006–081006.

99. Zhang, X., and Gan, R.Z. (2010). Experimental measurement and modeling analysis on mechanical properties of incudostapedial joint. Biomech Model Mechanobiol *10*, 713–726.

100.   Zhang, X., and Gan, R.Z. (2012). Dynamic Properties of Human Tympanic Membrane Based on Frequency-Temperature Superposition. Ann Biomed Eng *41*, 205–214.

101.   Zhang, X., and Gan, R.Z. (2013). Finite element modeling of energy absorbance in normal and disordered human ears. Hearing Research *301*, 146–155.

102.   Zhang, X., and Gan, R.Z. (2014). Dynamic Properties of Human Stapedial Annular Ligament Measured With Frequency–Temperature Superposition. J Biomech Eng *136*, 081004–081004.

103.   Zhang, X., Guan, X., Nakmali, D., Palan, V., Pineda, M., and Gan, R.Z. (2014). Experimental and Modeling Study of Human Tympanic Membrane Motion in the Presence of Middle Ear Liquid. JARO *15*, 867–881.